Imperial College London

Phase separation, crystallization and interactions in biopolymer blends studied in situ by macro ATR-FTIR spectroscopic imaging

Huiqiang Lu

Supervisor: Professor Sergei G. Kazarian

Department of Chemical Engineering

A thesis submitted to Imperial College London in part fulfilment of the requirements for the degree of Doctor of Philosophy in Chemical Engineering and the Diploma of Imperial College London

24/07/2020

I would like to dedicate this Thesis to my Parents: Jinsheng Lu & Lan Zhang and also to the rest of my family to acknowledge their unconditional help and support throughout my education

Great accomplishments require

ambition and tireless effort.

Declaration

This thesis is a description of the work carried out in the Department of Chemical Engineering, Imperial College London, between June 2018 and April 2021, under the supervision of Professor Sergei G. Kazarian. Except where acknowledged, the material is the original work of the author and no part of it has been submitted for a degree at any other university.

Abstract

Ubiquitous applications of biopolymer blends require a broader range of accurate information about their behaviour. For this purpose, macro attenuated total reflection-Fourier transform infrared (ATR-FTIR) spectroscopy and spectroscopic imaging are the main characterisation methods of choice to provide reliable information for both qualitative and quantitative analysis. The main objective of this project is to realise their full potential to investigate biopolymers and biopolymer blends with and without high-pressure CO_2.

In situ high-pressure ATR-FTIR spectroscopic imaging was applied to visualize the dynamic process of phase separation in biopolymer Polycaprolactone (PCL)/Poly (lactic acid) (PLA) blends under high-pressure CO_2. It was demonstrated that the extent of phase separation in PCL/PLA blends under high-pressure CO_2 is enhanced with increasing exposure time, CO_2 pressure and temperature.

The mechanisms of polymer-polymer interactions were investigated using 2D correlation analysis and 2D disrelation mapping. Evidence of the break of some of the existing inter- and intramolecular dipole-dipole interaction (C=O···C=O) between polymer molecules under high-pressure CO_2 was provided.

The simultaneous visualization of crystallization and phase separation in Poly (3-hydroxybutyrate) PHB/PLA blends has been realized for the first time through utilizing in situ ATR-FTIR spectroscopic imaging. Decreasing the annealing temperature is proved to be an effective method to constrain phase separation between these two blend components and tailor the final morphology in upper critical solution temperature (UCST) crystallizable polymer blends for practical applications.

Spectroscopic images based on the band position were successfully used to investigate changes in intra- and intermolecular interactions in PHB/PLA blends. During the isothermal melt crystallization, the disappearance of the intermolecular interaction between PHB and PLA and the appearance of the inter- and intramolecular interactions within the PHB crystal were both visualized.

Overall, this thesis has demonstrated further the use of ATR-FTIR spectroscopy and macro ATR-FTIR spectroscopic imaging as a valuable analytical approach to investigate

biopolymers and biopolymer blends with and without high-pressure CO_2, which can aid the design of biopolymer products and biopolymer process.

Acknowledgements

The completion of my PhD study and this thesis would not be possible without the support and aid of many people. First and foremost, I want to thank my respectable supervisor Prof. Sergei G Kazarian for his generous support and invaluable guidance throughout my PhD study. I am very grateful for his introduction to this exciting field of FTIR spectroscopy and his time invested in my research. As my supervisor and friend, he offers guidance supervision, encouragement and opportunities, which results in my achievement and improvement during the PhD period. I also owe much gratitude to my mentor Dr Chris Tighe for his advice and motivation.

I owe much gratitude to Great Britain-China Educational Trust for providing a Chinese student award to me.

I would like to give my sincere appreciation to Prof. Harumi Sato (collaborator of my supervisor). Her knowledge of polymer crystallization has helped me a lot for my PhD project and the involvement in her book also helps my understanding of the theory in the field of polymer and vibrational spectroscopy. Dr. Hideyuki Shinzawa (collaborator of my supervisor) also contributed a lot to my research in the area of two-dimensional (2D) correlation spectroscopy.

Thanks are also given to our collaborating researcher: Dr. Diana Iruretagoyena Ferrer and Prof. Konstantin N. Mikhelson. The involvement in their projects inspired me to explore the new applications of spectroscopic imaging technology in activated carbons and membranes.

Special thanks to my friends and colleagues in my research group: Dr. Cai Li Song, Miss Hannah Tiernan, Mr James Beattie and Mr Guan-Lin Liu for their sincere and friendships.

Last but not least, I want to acknowledge my parents and family for all of their financial and mental support throughout my entire education.

List of publications

The results presented in this thesis are published in the following papers:

1. Lu H., Kazarian S. G., Sato H. Simultaneous visualization of phase separation and crystallization in PHB/PLLA blends with in situ ATR-FTIR spectroscopic imaging Macromolecules (2020) 53(20), 9074–9085

2. Lu H., Kazarian S.G. How Does High-Pressure CO_2 Affect The Morphology of PCL/PLA Blends? Visualization of Phase Separation using In Situ ATR-FTIR Spectroscopic Imaging Spectrochimica Acta Part A: Molecular and Biomolecular Spectroscopy (2020) 243, 118760

3. Lu H., Shinzawa H., Kazarian S. G. Intermolecular Interactions in the Polymer Blends Under High-Pressure CO_2 Studied by Two-Dimensional Correlation Analysis and Two-Dimensional Disrelation Mapping. Applied Spectroscopy (2021) 75(3), 250–258

4. Lu H., Sato H., Kazarian S. G. Visualization of Inter- and Intramolecular Interactions in Poly(3-hydroxybutyrate)/Poly(L-lactic acid) (PHB/PLLA) Blend During Isothermal Melt-crystallization Using Attenuated Total Reflection Fourier Transform infrared (ATR FT-IR) Spectroscopic Imaging Applied Spectroscopy (2021) 75(8) 979-986

5. Lu H., Ewing A. V., Kazarian S. G. 'FTIR spectroscopy and spectroscopic imaging for the analysis of polymers and multicomponent polymer systems' in 'Spectroscopic Techniques for Polymer Characterization: Methods, Instrumentation, Applications' Ed. Y. Ozaki & H. Sato 2021 (Awaiting publication, invited book chapter)

Other papers

1. Solovyeva E. V., Lu H., Khripoun G. A. Mikhelson K. N., Kazarian S. G. In situ ATR-FTIR spectroscopic imaging of PVC, plasticizer and water in solvent-polymeric ion-selective membrane containing Cd^{2+}-selective neutral ionophore Journal of Membrane Science (2021) 619, 118798

2. Iruretagoyena D., Bikane K., Sunny N., Lu H., Kazarian S. G., Chadwick D., Pini R., Shah N. Enhanced Selective Adsorption Desulfurization on CO_2 and Steam Treated Activated Carbons: Equilibria and Kinetics Chemical Engineering Journal (2020) 379, 122356

Table of content

List of figures

List of Symbols and Abbreviations

T = transmittance

A = absorbance

n = refractive index

ν = wavenumber, cm^{-1}

λ= wavelength, cm

$d_{e,u}$ = effective thickness, cm

d_p = depth of penetration, cm

l = pathlength, cm

c = molar concentration, $mol \times L^{-1}$

ε = molar absorptivity, $L \times mol^{-1} \times cm^{-1}$

θ = angle of incidence, rad

ATR = Attenuated Total Reflection

FTIR = Fourier Transform Infrared

FPA = Focal Plane Array

MCT = Mercury Cadmium Telluride

PCL=Polycaprolactone

PLA=Poly (lactic acid)

PHB=Poly (ε-hydroxybutyrate)

DSC=Differential scanning calorimetry

LCST= Lower critical solution temperature

M_w= Molecular weight

PEG= Poly (ethylene glycol)

PMMA= Poly (methyl methacrylate)

PTFE= Polytetrafluoroethylene

T_g= Glass transition temperature

T_m= Melting temperature

UCST= Upper critical solution temperature

wt%= Weight percent

χ = Flory-Huggins interaction parameter

Chapter One

Introduction

1. Introduction

1.1 Background

To save fossil raw materials and develop viable green technologies, biopolymers, which are biocompatible and biodegradable, have been widely studied by the scientific community. [1–5] However, compared with the standard plastics produced from crude oil, the physical properties of biopolymers are not always adequate for specific purposes. [6] Thus, through mixing two or more biopolymers with complementary physical properties together, biopolymer blends are created. Like composites, biopolymer blends can also combine the advantages of both components to cater for the performance requirements at low prices. [7–9]

Using high-pressure and supercritical CO_2 as a viable additive in polymer processing has a minimal environmental impact. As a promising alternative to the organic solvents, it can be produced at a high purity with a low cost and easily removed from the final products.[10]

In order to exploit the benefits offered by high-pressure CO_2, a thorough understanding of how high-pressure CO_2 interacts with polymers and affects their final properties is needed. Fourier transform infrared (FTIR) spectroscopy can detect the molecular vibrations of different components in the sample simultaneously and then reveal their morphology and structure. The molecular-level insight provided by this technology can produce vast amounts of valuable information to study this kind of interaction and then facilitate the polymer process.[11]

FTIR spectroscopic imaging can reveal the spatially resolved information. The intrinsic vibrational modes of functional groups are used to identify the spatial distribution of different components in the ternary polymer A/polymer B/ CO_2 systems and quaternary amorphous polymer A/ crystalline polymer A/ amorphous polymer B/ crystalline polymer B systems.[12] Attenuated total reflection (ATR) mode is chosen for the FTIR spectroscopic imaging in the studies described in this Thesis because of its advantages including little or no sample preparation and independent of the sample thickness.

Ubiquitous applications of biopolymer blends require a broader range of accurate information about their behaviour. For this purpose, ATR-FTIR spectroscopy and spectroscopic imaging are the characterisation methods of choice to provide reliable information in situ for both

qualitative and quantitative analysis.[13] In this project, phase separation, crystallization and interactions in representative biopolymer blends (polycaprolactone (PCL)/ poly (lactic acid) (PLA) blends and poly(3-hydroxybutyrate) (PHB) / PLA blends) have been investigated in situ by macro ATR-FTIR spectroscopic imaging.

1.2 Objectives

The main objective of this project is to realise the full potential of ATR-FTIR spectroscopy and ATR-FTIR spectroscopic imaging to investigate biopolymers and biopolymer blends with and without high-pressure CO_2. Different biopolymer blends, such as the upper critical solution temperature (UCST) biopolymer blends and the lower critical solution temperature (LCST) biopolymer blends, have been studied.

To be more specific, the major objectives of this work are laid out as follows:

1. To study phase separation in the PCL/PLA blend, a typical lower critical solution temperature (LCST) polymer blend, under high-pressure CO_2. This is because the quality of final polymeric products in almost all polymer processes depends in part on how well the material was mixed. The purpose of this work is to visualize the dynamic process of phase separation in this blend exposed to high-pressure CO_2 utilizing in situ high-pressure ATR-FTIR spectroscopic imaging. The extent of phase separation under different conditions (temperature, CO_2 pressure, exposure time and polymer molecular weight) will be compared.

2. To study the mechanism of interaction appearing in the PCL/PLA interface before and under exposure to high-pressure CO_2 through using two-dimensional correlation analysis and two-dimensional disrelation mapping. With the specially designed polymer interface, the interaction between the same type of polymers and that between different types of polymers will be distinguished. These interactions with high-pressure CO_2 and those without high-pressure CO_2 will also be compared. The interaction between polymers and CO_2 will also be demonstrated. The two-step formation process of CO_2-polymer complex in the previous study [14] will be proved and the effect of Flory interaction parameter on phase separation of this polymer blend under exposure to high-pressure CO_2 will be investigated.

3. To investigate the phase separation and crystallization in the PHB/PLA blend simultaneously using in situ ATR-FTIR spectroscopic imaging. The change in the degree of crystallization and the extent of phase separation between crystalline polymers during the isothermal melt-crystallization process will be detected. The mechanism of crystallization and phase separation in UCST polymer blends during this process will be discussed.

4. To investigate changes in intra- and intermolecular interactions in PHB/PLA blends during the isothermal melt crystallization through using spectroscopic images based on the band position. These spectroscopic images will be prepared to reflect the spatial distribution of different intra- and intermolecular interactions in the polymer blend. Furthermore, the obtained spectroscopic images based on the band position will be compared with the spectroscopic images based on integrated absorbance.

1.3 Outline of thesis

This thesis demonstrates that macro ATR-FTIR spectroscopic imaging can be utilized as a reliable approach to study phase separation, crystallization and interactions in polymers and polymer blends with and without high-pressure CO_2.

Chapter 2 provides a detailed literature review to introduce the background knowledge for the research presented thereafter. It commences with the fundamentals of ATR-FTIR spectroscopy, ATR-FTIR spectroscopic imaging and 2D correlation spectroscopy. Then it moves on to discuss the current status of some important concepts in polymer research using FTIR spectroscopy, such as miscibility in polymer blends, interaction in multicomponent polymer systems and polymer crystallization. Then some of the current problems which need to solve are identified. Chapter 3 reveals the experimental procedures and experimental instruments used in this work.

Visualization of phase separation in PCL/PLA blends under high-pressure CO_2 is presented in Chapter 4, which is based on the peer-reviewed journal paper [9]. Chapter 5 describes the investigation of mechanism of interaction in PCL/PLA blends under high-pressure CO_2 using 2D correlation analysis and 2D disrelation mapping, which is based on the peer-reviewed journal paper [15]. The use of in-situ ATR-FTIR spectroscopic imaging to visualize phase

separation and crystallization simultaneously in PHB/PLA blends can be found in Chapter 6, which is based on the peer-reviewed journal paper [16]. The feasibility to visualize changes in intra- and intermolecular interactions in PHB/PLA blends during the isothermal melt crystallization through using spectroscopic images based on the band position is described in Chapter 7, which is based on the peer-reviewed journal paper [17]. An overall summary of this work is presented in Chapter 8 along with the opportunities for continuation of this project in the future.

Chapter Two

Literature review

2. Literature review

The first objective of this chapter is to introduce the fundamentals of ATR-FTIR spectroscopy, ATR-FTIR spectroscopic imaging and 2D correlation spectroscopy, which can reveal valuable information about the polymer samples. Then it summarizes the previous progress in the investigation of polymers with spectroscopic technology and highlights some of the current problems which need to solve. Thus, the novel opportunities are discovered and then investigated in the following chapters.

2.1 Introduction to FTIR spectroscopy

Spectroscopy is the study of matter and its properties using electromagnetic radiation. It quantitatively measures the consequences of the interaction of light with matter and then determines the molecular structure and physical characteristics of materials. Infrared spectroscopy is one of the main spectroscopic technologies to detect the chemical components and their molecular state in the unknown sample. It is the study of absorption of radiation from the IR region of the electromagnetic spectrum. The frequency of absorbed radiation exactly matches the frequency of molecular vibration. IR spectroscopy can only detect the infrared active molecules, which show the change of dipole moment during molecular vibration. The dipole moment is a measure of the separation of positive and negative electrical charges. Infrared spectroscopy can provide a molecular-level insight into the microstructures of polymers, such as configuration, conformation, constitution and intra- or intermolecular interactions. According to the Hooke's Law, the vibrational frequency is proportional to the strength of spring, which means that a stronger spring leads to a higher frequency. In the field of IR spectroscopy, it means that stronger bonds (molecular interactions) absorb at higher vibrational frequencies. Thus, it is an ideal technique to reveal the underlying physical basis for polymer processing, because the obtained molecular-level information of polymers can be used to improve the macroscopic properties of polymeric materials. [13,18,19]

One of the advantages of infrared spectrometry is its versatility. Samples in all states of matter, such as gases, liquids and solids, can be studied. According to the intensity, wavenumber and shape of bands in the sample spectrum, the chemical bonds of the

molecules can be distinguished and then the molecular structure can be determined. The infrared region can be divided into three major regions: near-infrared (12000-4000 cm^{-1}, overtones/harmonics), mid-infrared (4000-400 cm^{-1}, molecular vibrations) and far-infrared (400-20 cm^{-1}, rotations/low energy vibrations). In this research, mid-infrared radiation is applied to study the fundamental molecular vibrations. [20–24]

Interferometers are the 'heart' of the infrared spectrometry and most of the current interferometers are based on the two-beam interferometer designed by Albert A. Michelson. Compared with the traditional diffraction grating, spectra can be obtained quickly and signal to noise is improved using interferometers. As shown in Figure 2.1, it can divide the beam of radiation emitted from the IR source into two paths by a beamsplitter, which consists of a fixed mirror and a moving mirror. Half of the beam of radiation is reflected to the fixed mirror and the other half is transmitted to the moving mirror. After recombined at the beamsplitter, the beam of radiation interacts with the sample. The molecules in the sample absorb the radiation in specific wavenumber ranges and then the rest IR radiation reaches the detector. The optical path difference between these two halves of the beam, which is caused by the movement of the adjustable mirror, results in the generation of constructive and destructive interference. Then the detector produces interferogram which is a plot of beam intensity emerging from the interferometer against path difference. Fourier transform algorithm is used to convert the interferogram into an infrared spectrum, which is a plot of infrared intensity against wavenumber. Spectrum is a representation of what electromagnetic radiation is absorbed or emitted by the sample. In order to obtain the spectrum of pure sample, background spectrum, which is measured without sample, should be ratioed against the sample spectrum so as to eliminate the contribution of instruments and atmosphere. Therefore, the transmittance spectrum can be obtained through equation 2.1.

$$T\ (\%) = \frac{I}{I_0} \times 100\% \qquad \text{equation 2.1}$$

Where T(%) is transmittance, I is the intensity of radiation in the system with the sample, I_0 is the intensity of radiation in the system without the sample. [24]

For quantitative analysis, absorbance values should be used to replace transmittance value. Equation 2.2 is used for this transition.

$$A=-\lg T \qquad \text{equation 2.2}$$

Where A is the absorbance. [24]

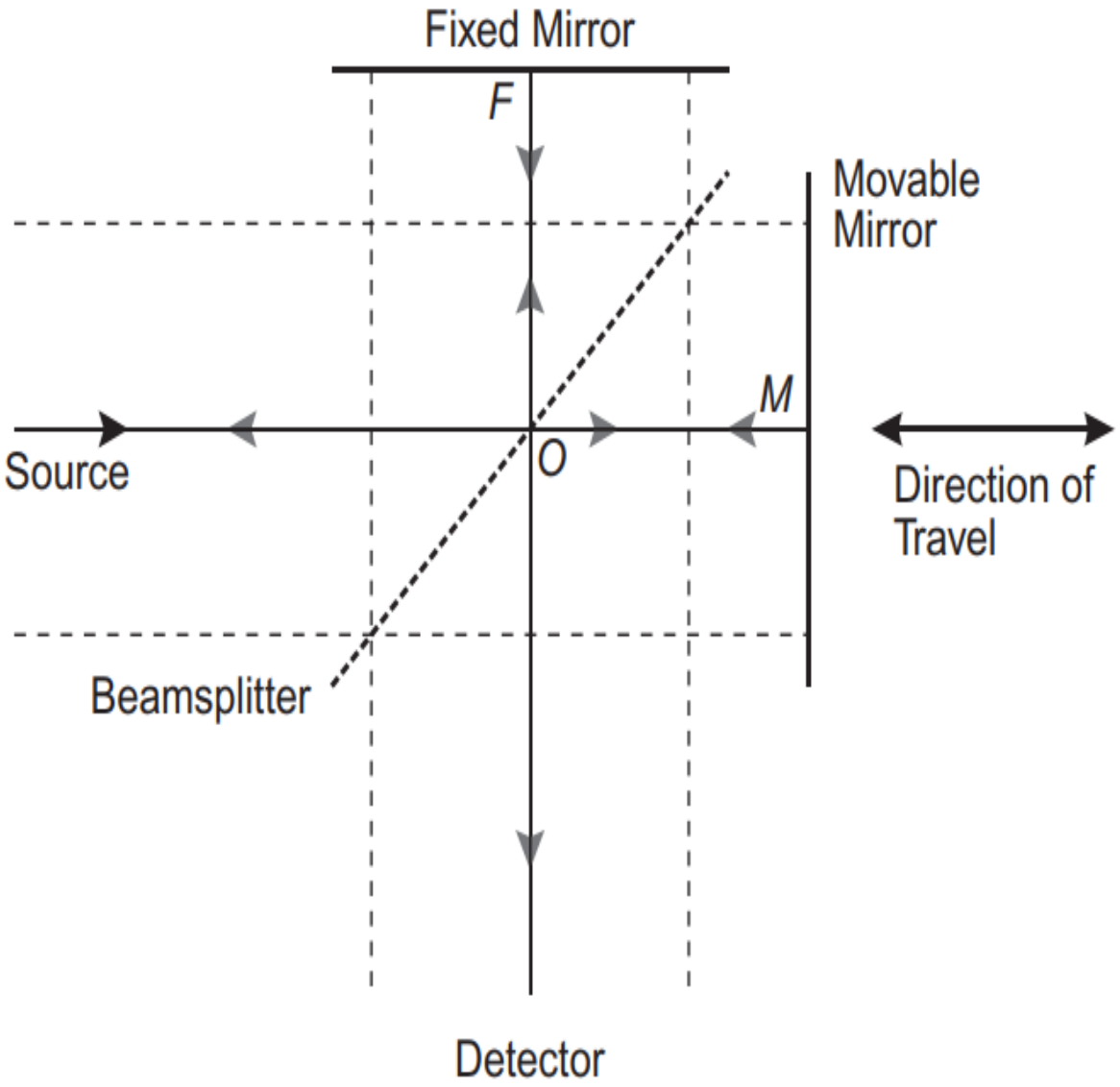

Figure 2.1 Schematic diagram of the Michelson interferometer. (Solid line is the median ray and dashed line is the extreme of the collimated beam) (Source [24]**)**

2.1.1 Quantitative analysis of FTIR spectra

One of the powers of spectroscopy is the ability to deduce the quantity of absorbing materials in a sample. The Beer-Lambert law, which is also called Beer's law, is a fundamental law of quantitative spectroscopy. It reveals that the absorbance of a spectral band is proportional to the component concentration and light pathlength, as indicated in equation 2.3.

$$A = \varepsilon lc \qquad \text{equation 2.3}$$

Where ε is the molar absorptivity, l is the pathlength through the sample and c is the concentration of the components. [6,25]

This equation makes it possible to calculate the concentration of each component in the measured sample.

2.1.2 Methods of acquisition

There are three common sampling methods available for infrared light to interact with the sample, which are transmission, reflection and attenuated total reflection (ATR). Among them, ATR mode, which is ideal for strongly absorbing samples, has become more and more widely applied in the field of infrared spectroscopy. Its advantages include little or no sample preparation (no change in the sample morphology) and consistent results. But it can only reveal the composition of bottom surface layer instead of the bulk area. [24,26]

The sample is placed directly on the ATR crystal and the sufficient contact should be ensured. The common ATR crystals used are diamond, Zinc Selenide (ZnSe) and Germanium. In this research, which includes high-pressure investigation, we use diamond (refractive index: 2.4) as the ATR crystal because it is chemically resistant and can endure high temperature and pressure. [7,24]

As shown in figure 2.2, the theory of ATR-FTIR spectroscopy is following: the IR beam is directed at a pyramidal ATR prism with a relatively high refractive index and approaches its top surface at an angle greater than the critical angle. Total internal reflection occurs at the interface between the sample and ATR crystal and then an evanescent wave penetrates orthogonally into the sample with an exponential decay of the magnitude of the electric field. [21,26] The depth of penetration of the evanescent wave can be calculated through equation 2.4. It is defined as the distance of the electric field penetrating into the sample before its amplitude falls to 1/e (about 37%) of its original value at the surface. [27]

$$d_p = \frac{\lambda}{2\pi n_2 (\sin^2\theta - \left(\frac{n_1}{n_2}\right)^2)^{\frac{1}{2}}} \qquad \text{equation 2.4}$$

Where d_p is the depth of penetration, λ is the wavelength of the incident beam, n_1 and n_2 are the refractive indices of ATR crystal and sample, respectively, θ is the incident angle. [27]

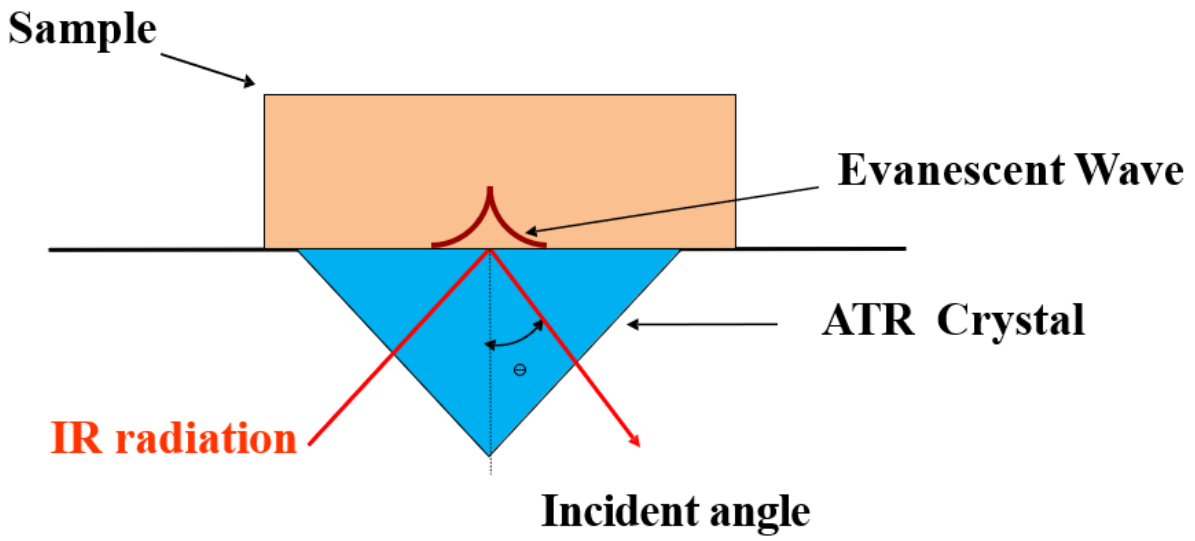

Figure 2.2 Schematic diagram of the principle of ATR mode (ATR crystal with sample showing evanescent wave).

When applying Beer-Lambert Law in the ATR mode, effective thickness should be used instead of the pathlength. It is defined as a pathlength giving the same absorbance in an ATR-IR experiment as that obtained in a transmission IR experiment, which can be calculated through the following equation.

$$\frac{d_{e,u}}{\lambda} = \frac{\frac{n_2}{n_1}cos\theta\left[3\sin^2\theta - 2\left(\frac{n_2}{n_1}\right)^2 + \left(\frac{n_2}{n_1}\right)^2\sin^2\theta\right]}{2\pi\left[1-\left(\frac{n_2}{n_1}\right)^2\right]\left\{\left[1+\left(\frac{n_2}{n_1}\right)^2\right]\sin^2\theta - \left(\frac{n_2}{n_1}\right)^2\right\}\left[\sin^2\theta - \left(\frac{n_2}{n_1}\right)^2\right]^{\frac{1}{2}}} \qquad \text{equation 2.5}$$

Where $d_{e,u}$ is the effective thickness. [28]

2.2 Introduction to FTIR spectroscopic imaging

As mentioned in the section 2.1 of this Thesis, the conventional FTIR spectroscopy with a single element detector can provide an average FTIR spectrum from the measured area. However, this method can not reveal the spatial information of different components in the sample. Mapping technology can be used to obtain the spatial information by scanning the

beam or moving the sample. However, it is not suitable for dynamic systems because a system could change much during slow measurements by mapping. [29,30]

To solve these problems, a focal plane array (FPA) detector was used to collect the full spectra from different locations of a sample simultaneously. The size of array commercially available ranges from 32×32 pixels to 256×256 pixels and most of them have a pixel size of 40 μm×40 μm. [21] The absorbance of a specific spectral band is obtained by integrating its band area in a certain wavenumber range. Through plotting the distribution of the absorbance of specific band across all of the measured pixels, the FTIR images are produced to reveal the spatial distribution of different components in the imaged area as shown in figure 2.3. Like the common photographic camera, FTIR spectroscopic imaging is especially suitable for the study of dynamic systems in 'real-time' because of the simultaneous data acquisition and short measurement time. It is very versatile because no dye is needed to add when providing chemically specific images. It is also possible to monitor many samples for high-throughput analysis[13,29]

In terms of ATR-FTIR spectroscopic imaging, it is the combination of FTIR spectroscopic imaging with an ATR accessory. The obtained ATR-FTIR images reflect the concentration distribution of each component in the surface layer of the sample, which is around several micrometres thick. [29] This technique has three significant advantages: (1) Little or no sample preparation is needed. (2) It can analyse the aqueous solution and corrosive materials. (3) The precise control of temperature is feasible. Apart from the field of polymer science, this technology can also be applied to other systems, such as protein [31], biopharmaceuticals [29,32], membrane [33], tissue [34], crude oil fouling [35], forensic science [36] and so on.

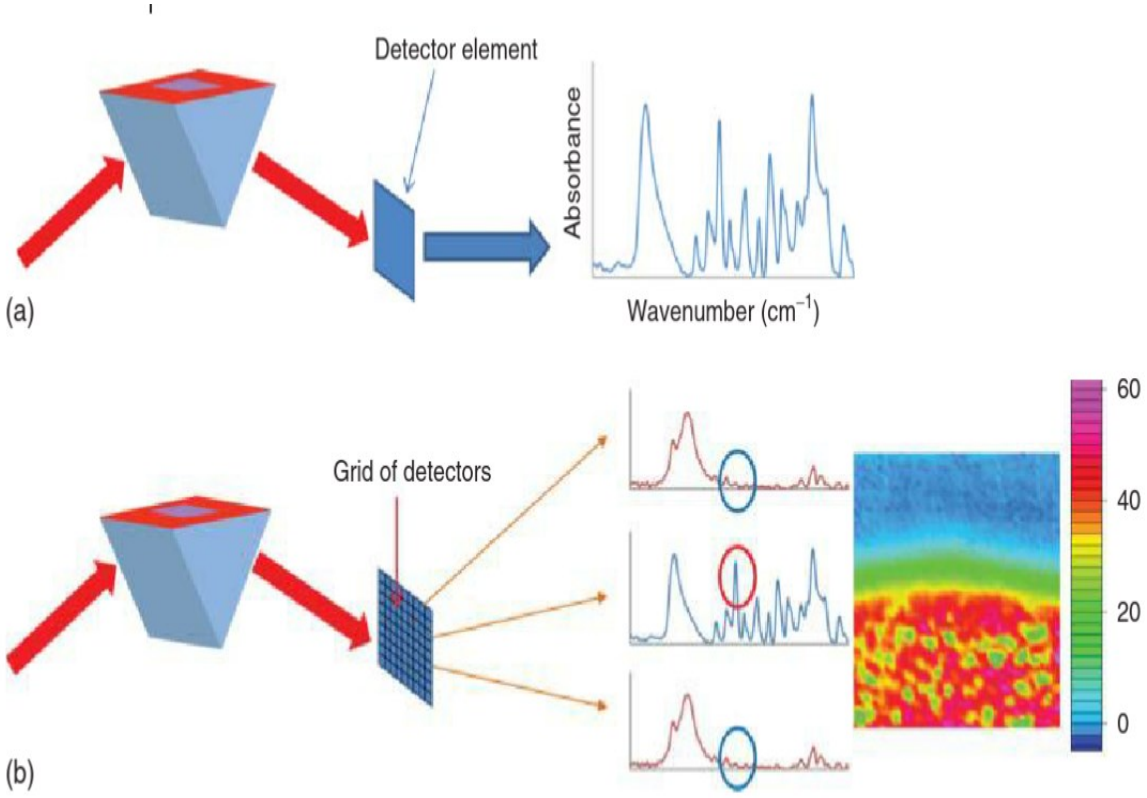

Figure 2.3 Schematic diagram of (a) the average FTIR spectrum produced from the conventional FTIR spectroscopy (b) FTIR images produced from the FTIR spectroscopic imaging. (Source [21]**)**

Apart from ATR-FTIR spectroscopic imaging, a range of characterization techniques, such as Atomic force microscopy (AFM), Scanning electron microscopy (SEM), and Transmission electron microscopes (TEM), are also widely used to investigate polymer systems. AFM is a type of scanning probe microscopy (SPM) with a very high resolution (order of fractions of a nanometer). SEM is a type of electron microscope with a resolution better than 1 nanometer. It opens the possibility of 3D imaging in a large depth of field and a high magnification. TEM is another advanced microscopy approach with an unique resolution (~0.07 nm), It can provide detailed information concerning the internal structure of measured samples. [37] Although all of these advanced characterization techniques have better spatial resolutions, they are not suitable to measure the samples with increasing temperature or under exposure to high-pressure CO_2.

2.2.1 Macro ATR-FTIR spectroscopic imaging

ATR-FTIR spectroscopic imaging can be divided into two types: micro ATR-FTIR spectroscopic imaging with microscope optics and macro ATR-FTIR spectroscopic imaging without microscope optics. In this work, macro ATR-FTIR spectroscopic imaging, which is suitable for a larger field of view, is applied to investigate the polymer system. It can be used to investigate the dynamic processes, such as interdiffusion in polymer interface and phase separation in polymer blends.[38]

The internal structure of Golden Gate™ ATR accessory in macro mode is shown schematically in figure 2.4. Mirrors and lenses are used to focus the light onto ATR crystal. Diamond is chosen as ATR crystal because of its high refractive index. Its high stiffness and strength allow the use of force to ensure good contact between the sample and ATR crystal, which can improve the reproducibility of the obtained data. [39]

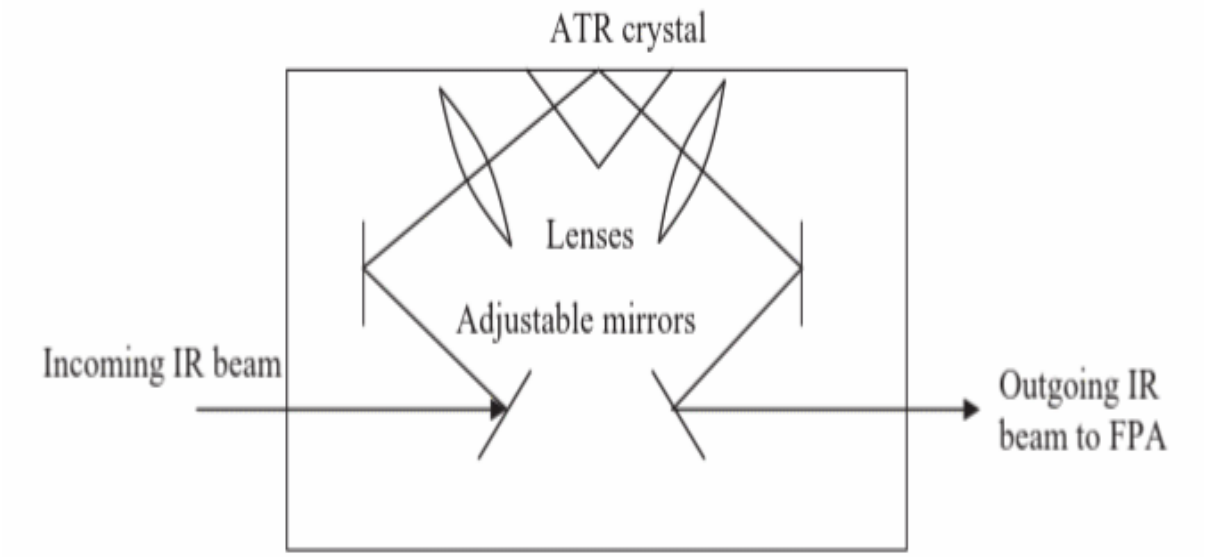

Figure 2.4 Schematic diagram of the internal structure of Golden Gate™ ATR accessory in macro mode. (Source [39]**)**

2.3 Two-Dimensional Correlation Spectroscopy (2D-COS)

Among numerous methods of spectral analysis, the most popular one is two-dimensional (2D) correlation spectroscopy (2D-COS). It has been proved to be a versatile analysis method for different spectroscopic modalities, such as IR and Raman spectroscopy. It was introduced by Noda in 1989 for the first time and widely applied in the fields of polymer, pharmacy, protein and materials.[40] It can facilitate the interpretation of structural and compositional information obtained from ATR-FTIR spectroscopy and ATR-FTIR spectroscopic imaging. Thus, it can lead to a better understanding of the molecular composition of measured samples. Apart from the applications in IR and Raman spectroscopy, 2D correlation spectroscopy can also be used in ultraviolet-visible (UV-Vis) spectroscopy, fluorescence, mass spectrometry and nuclear magnetic resonance (NMR). [41,42]

Some of the spectral features caused by different kinds of vibration are difficult to distinguish in the original data set. Through spreading the overlapped bands over the second dimension, spectral resolution is enhanced and then 2D correlation spectroscopy can be applied to identify these spectral features.[41,43,44] It can also be used to study intermolecular interactions.[45–47]

Moreover, this technology is especially suitable for the study of dynamic process in order to monitor the response of the system to the external perturbation spectroscopically. The common sources of perturbation are temperature, pressure, concentration, pH and spatial position. During the analysis, the only variable parameter is the external perturbation. Other parameters, such as sample, temperature and spatial position, should be constant. The spectral intensity is acquired as a function of two different independent variables, such as frequencies, wavenumbers or wavelengths. [47–49] After then, the simultaneous or sequential changes of the correlation intensity of spectral variations are derived as synchronous or asynchronous correlations. [43,48,50]

The peaks in the synchronous spectrum mean the similar spectral intensity variations at spectral variable positions ν_1 and ν_2. The autopeaks, which are on the diagonal line and always positive, indicate the extent of change in the spectral intensities at a certain wavenumber (wavelength). The cross peaks, which are located at off-diagonal positions, can be positive or negative. They indicate the synchronized spectral changes of distinct spectral features. Positive cross peaks reflect that the band at ν_1 and the band at ν_2 increase or

decrease together. Negative cross peaks reflect that one of these two bands increases and the other decreases.[44]

The peaks in the asynchronous 2D correlation spectrum mean the dissimilar (unsynchronized) spectral intensity variation at these two positions, which indicates the sequential order of spectral events. Since the asynchronous spectrum is antisymmetric at the diagonal line, only off-diagonal cross peaks instead of autopeaks can be observed. When the corresponding cross peak in the synchronous spectrum is positive, a positive cross peak in an asynchronous spectrum indicates the change in spectral intensity at v_1 occurs ahead of that at v_2. A negative cross peak indicates the spectral intensity variation at v_1 occurs after that at v_2 under the same condition.[44]

Based on multiple perturbation 2D correlation analysis, [40,41] Shinzawa et al have invented '2D disrelation mapping' in 2017, to highlight the dissimilarity among spectra extracted from a chosen area. [46] The disrelation intensity becomes strong in the areas where spectral feature changes. Thus, it has the capacity not only to enhance the spectral resolution but also to identify the band origins. This method obtains the disrelation intensity $\mathbf{\Lambda}_{ij}$ through so-called convolution windows. Firstly, through the FTIR spectroscopic imaging, spectra from different positions in the imaged area can be obtained. The spectral data at v_1 and v_2 of the pixels in the convolution window are used to calculate the disrelation intensity between v_1 and v_2 of central pixel. Through moving the convolution window across the whole image, the disrelation map, which reflects the distribution of disrelation intensity in the imaged area, can be generated as shown in figure 2.5. Its main function is to detect the interaction between two molecules and the temporary appearance of intermediate species, which are both difficult to discover through the visual inspection of conventional FTIR spectroscopic images. [46]

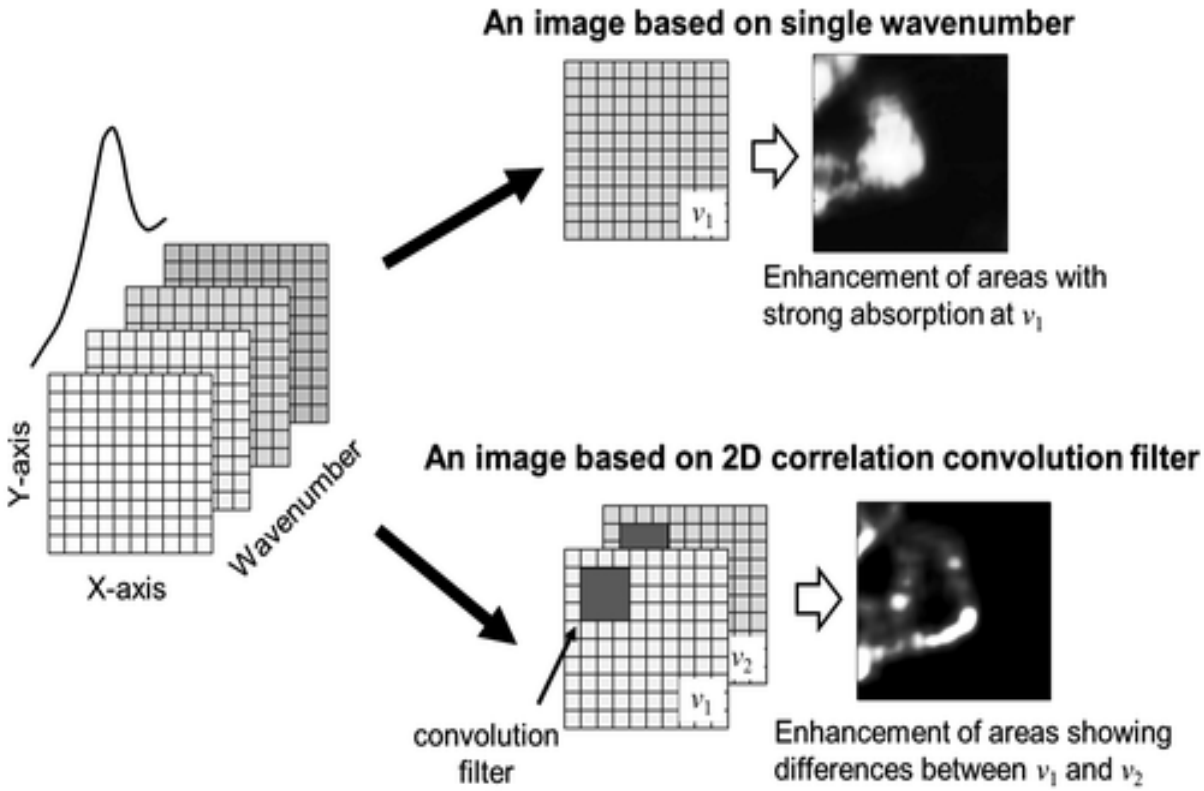

Figure 2.5 Schematic diagram of disrelation mapping based on 2D correlation convolution filter.[46]

2.4 High-pressure and supercritical CO_2

Supercritical fluid is a liquid or gaseous substance which exceeds its critical temperature and pressure. By changing the pressure or temperature, the gas properties can be transited to liquid properties so that it is a 'tunable' solvent. Due to its liquid-like density and gas-like viscosity, it benefits the polymer processes a lot, such as extraction, purification, foaming and impregnation.[7]

As a non-toxic, non-flammable, 'green' and cheap gas, high-pressure and supercritical CO_2 has been used in many types of chemical engineering activities as a viable alternative to volatile organic compounds currently used. The critical temperature (304.15K) and pressure (7.38 MPa) of CO_2 are easily achieved. Similar to heat and some organic solvents, it can also induce temporary plasticization of polymers, which means that the interchain distances and free volume increase while the degree of segmental and chain mobility is enhanced. Plasticization results in decreasing glass transition temperature (T_g) of amorphous polymers or decreasing melting temperature (T_m) of crystalline polymers.[51,52] Thus, heat-sensitive polymeric materials can be processed and thermally labile additives can be added under a

lower temperature with high-pressure CO_2. As CO_2 is gaseous at ambient temperature and pressure, it can be totally removed from the final products after the polymer processing so that these products without residual solvent are more suitable to use in biotechnological, pharmaceutical and food processing applications. The removal of caffeine from coffee beans and the preparation of encapsulated materials in the pharmaceutical industry are two well-known examples. High-pressure CO_2 can also induce beneficial changes in polymers, such as plasticisation, crystal modification, foaming, impregnation and viscosity reduction. [53]

One of the main obstacles to polymer process, especially polymers with larger M_w, is the high viscosity of many polymeric raw materials. The common methods to reduce the viscosity, such as heat and plasticizing agents, are not ideal enough. Heat consumes more energy and is more likely to induce thermal degradation. On the other hand, plasticizer is difficult to remove totally and is more likely to contaminate the final products. [54,55] High-pressure CO_2, as a 'molecular lubricant', has the same effect as heating the polymer above its T_g: increasing chain and segmental mobility and decreasing viscosity. This property can benefit the polymer process a lot because of the lower shear stress. [13,56] Moreover, the thermolabile or bioactive polymers, which are impossible to obtain through standard routes, can be processed at a lower temperature with high-pressure CO_2. However, T_g of polymers does not reduce any more after the pressure of CO_2 reaches a certain point, which means that the effect of high-pressure CO_2 as a plasticizer is limited. [52,57,58]

Polymers with basic functional groups, which are electron donor species, can form Lewis acid-base interactions when exposed to CO_2. The carbon atom of CO_2 acts as an electron acceptor. Greater strength of this interaction leads to a higher plasticizing effect on polymers and then results in more viscosity reduction. This is because high-pressure CO_2 can disrupt the current inter- and intramolecular interactions in polymers and thus increase the chain distance. [59,60] The strength of interactions depends on temperature, CO_2 pressure and M_w. [61]

Polymer crystallization can also be induced after exposure to high-pressure CO_2. When the decrease of T_g is at the same level as that of T_m, the rate of crystallization increases with increasing CO_2 pressure at the temperature in the crystal-growth controlled region and decreases at the temperature in the nucleation-controlled region. In the crystal-growth controlled region, the dominant effect of CO_2 is to enhance the self-diffusion of polymer chains. On the other hand, in the nucleation-controlled region, the domain effect of CO_2 is to

hinder the nuclei to reach its critical size and thus reduce the nucleation rate. [62] Under exposure to high-pressure CO_2, the chain and segmental mobility becomes greater and free volume in polymers increases so that the polymer chains can be rearranged into a more thermodynamically stable state.[59,63] Then small spherulites (crystallites) are formed and grow with increasing exposure time. The kinetics of crystallization is affected by temperature and CO_2 pressure. Specific types of crystalline forms, which are not obtainable through the traditional process, can be induced by high-pressure CO_2. Other high-pressure gas, such as high-pressure N_2, can not induce such type of crystalline forms, which means that they are caused by the plasticization effect of CO_2 instead of the hydrostatic pressure of high-pressure gas. Moreover, polymer crystallization also occurs after decompression and it affects the final product of polymeric foams a lot. [57,62–64]

The capital cost of high-pressure CO_2 processing is relatively high, which increases the manufacturing cost of the final products. [8] After installation, cost of high-pressure CO_2 processing is affected by the total cycle time (pressure rise, holding and loading/unloading times), energy, labour and vessel filling ratio. The processing costs and environmental impact of high-pressure CO_2 processing are much higher than those of conventional thermal processing. [65] However, because of these substantial advantages for polymer processing mentioned above, novel polymeric materials with unique characteristics and properties can be produced with the help of high-pressure CO_2. Besides polymer processing, high-pressure CO_2 can also benefit different kinds of polymer synthesis. Thus, the investigation of polymer processing with high-pressure CO_2, which benefits the overall performance of polymeric materials, has great commercial values. Prior to its successful application, information regarding the interactions between polymers and high-pressure CO_2 is required to optimise the processes.[61]

2.5 Current study of polymers and polymer blends with spectroscopic techniques

In this section, the current state-of-the-art research through using FTIR spectroscopic approaches was reviewed. Some important discoveries, such as miscibility in polymer blends, polymer crystallization and inter- and intramolecular interactions between polymers in the polymer blend, were summarized. Since high-pressure CO_2 treatment can improve the

physical and mechanical properties of polymers a lot, investigating the behaviour of polymers and polymer blends with or without high-pressure CO_2 benefits the development of more efficient polymer processing routes.

2.5.1 Investigation of miscibility in polymer blends

Miscibility of polymer blends affects the properties of final products, especially physical properties (mechanical, electrical, optical etc). [66–69] As a result, it is vital to know when possible phase separation will occur in the products containing polymer blends so that this phenomenon can be mitigated. [9] A phase diagram, which is made up of a bimodal line and a spinodal line, can reveal the miscibility of polymers in the blend under different volume fractions and temperatures. The binodal line defines the boundary between miscible and immiscible blends under certain conditions while the spinodal line indicates whether the blend is unstable or metastable. [70–73] The point of junction of these two lines indicates the critical temperature and volume fraction for the blend to become homogeneous. In terms of the UCST polymer blend, the critical temperature will increase when the volume fraction moves from 0 towards the critical point and decrease when the volume fraction moves from the critical point towards 1. In terms of the LCST polymer blend, the critical temperature shows an opposite trend with increasing volume fraction. [70,74–76] Briber et al. used cloud point measurements and DSC to prepare the phase diagram for the α-PVF_2/PEA blend system and confirmed that phase separation in LCST polymer blends occurs at the temperature beyond the cloud point. [77] As shown in figure 2.6, Koyama et al used the Flory-Huggins equation to prepare the phase diagram for PHB/PLA blends with different molecular weights. [68,78]

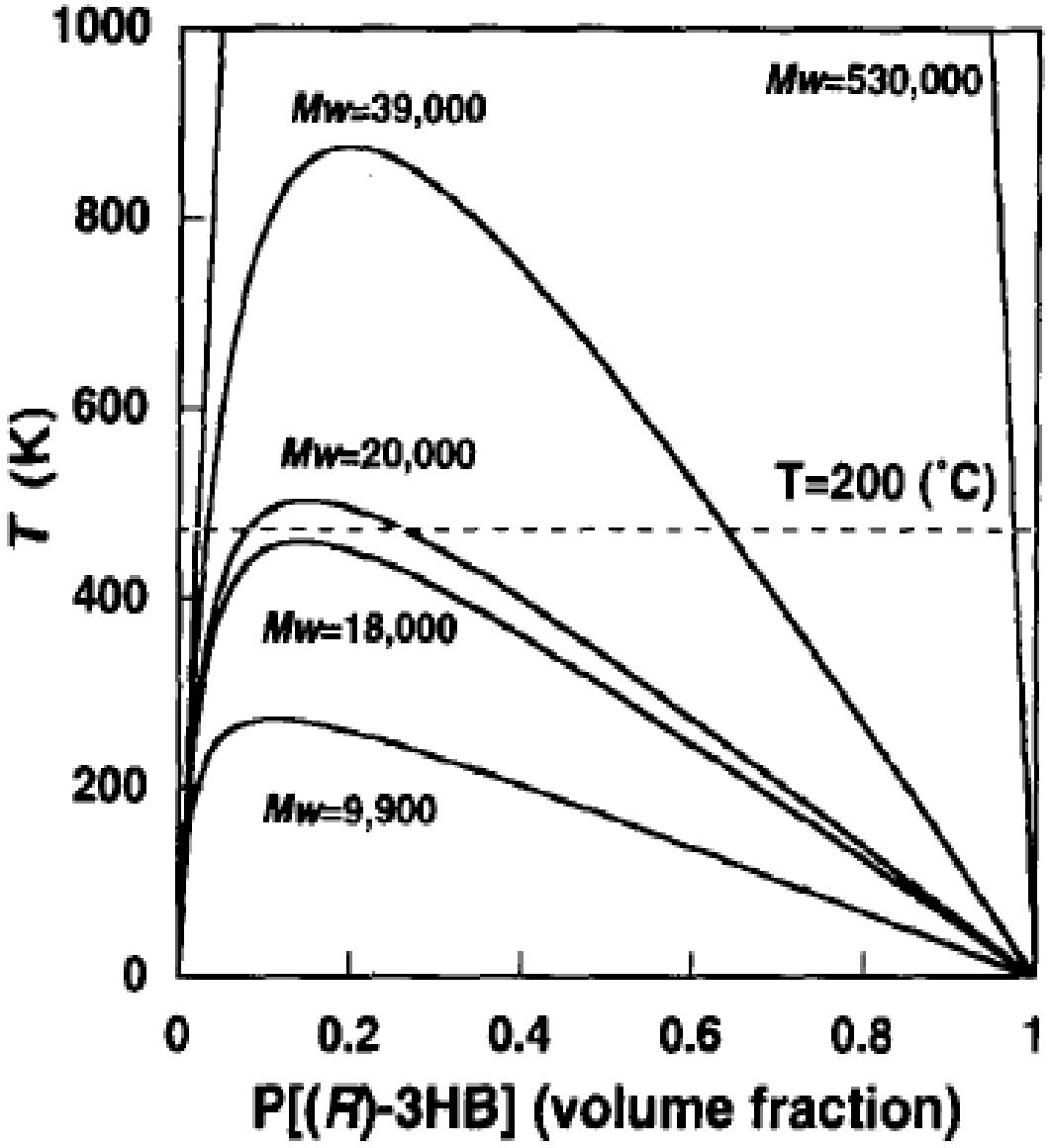

Figure 2.6 Spinodal curves of the PHB/PLA blends with different M_w (Source [68])

Vogel et al. have visualized phase separation in UCST polymer blends using transmission FTIR spectroscopic imaging to improve the physical properties of biopolymer blends. As shown in figure 2.7, the occurrence of phase separation in the PHB/PLA (50wt/50wt) blend and a compatible one-phase system of the PHB/PLA (70wt/30wt) blend can be clearly observed through the transmission FTIR spectroscopic images. Other technologies, such as DSC and miniaturized stretching machine, were used to provide more evidence for the occurrence of phase separation. Then transmission FTIR spectroscopic imaging was used to detect the phase separation in other polymer blends, which proved that this technology is

suitable for different types of polymer blends. Through changing the blend composition, the miscibility gaps of polymer blends can be obtained, which benefits the preparation of phase diagram. [6]

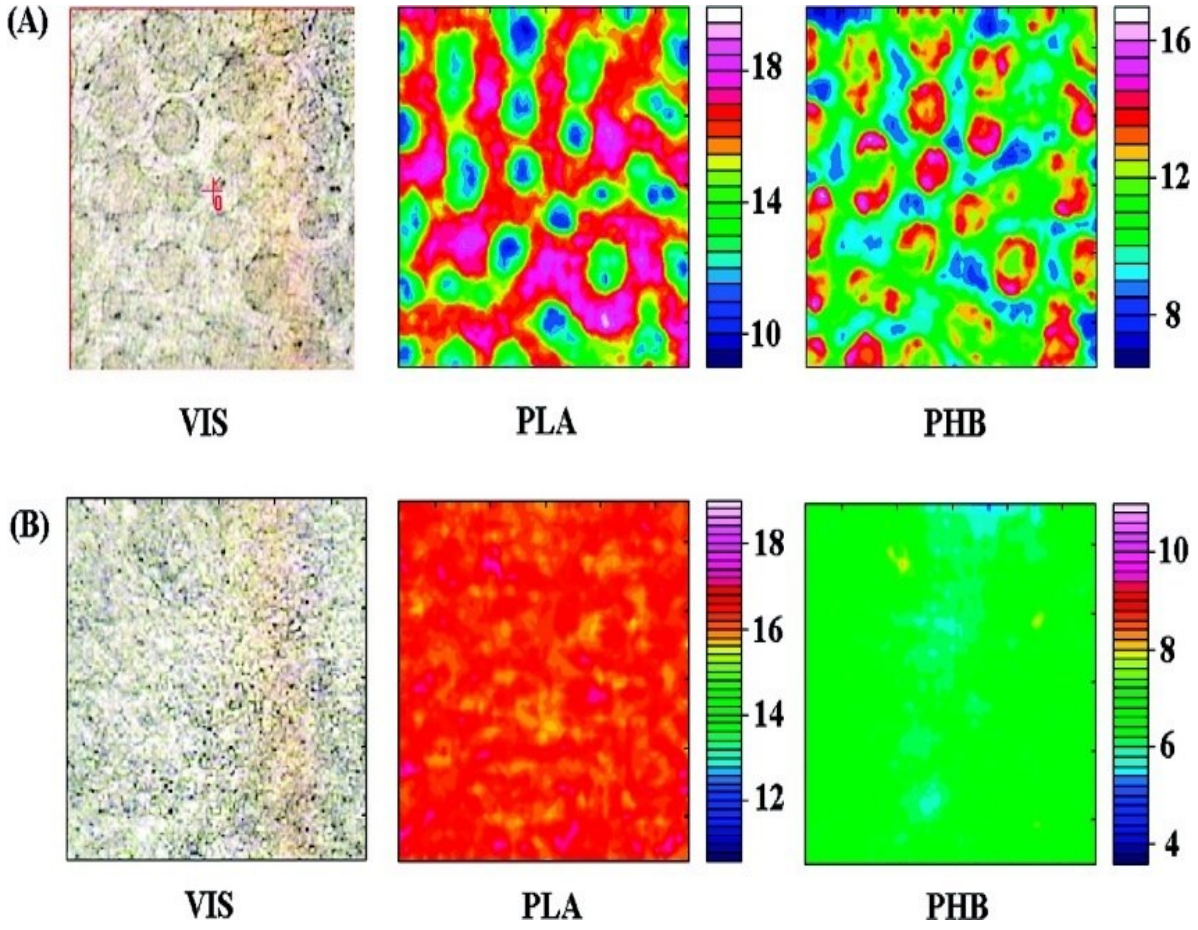

Figure 2.7 (A) Visual image (left), PLA-specific FTIR image (centre), and PHB-specific FTIR image (right) of the PHB/PLA (50wt/50wt) blend. (B) Visual image (left), PLA-specific FTIR image (centre), and PHB-specific FTIR image (right) of the PHB/PLA (30wt/70wt) blend. (Source [6])

The interdiffusion of two different polymers under high-pressure CO_2 has been studied. Polyvinylpyrrolidone (PVP) / poly(ethylene glycol) (PEG) interfaces were prepared and then subjected to high-pressure CO_2. [79] Since high-pressure CO_2 can plasticise the polymers and

reduce their viscosity, the rate of interdiffusion in miscible polymer systems is accelerated under high-pressure CO_2. As shown in figure 2.8, it was observed that PEG sorbs more CO_2 than PVP, which is because the relative affinity of CO_2 for PEG leads to the favourable sorption into its matrix. The mutual diffusion of PVP and PEG with increasing time was visualized using ATR-FTIR spectroscopic imaging for the first time. [79] It was also found that high-pressure CO_2 not only accelerates the interdiffusion but also facilitates its occurrence through increasing the segmental and chain mobility. This is because polymer mobility affects the transport and diffusion properties within polymer matrices. Thus, when the molecular weight of PEG was changed from 600 to 1500 in the same work, the interdiffusion did not occur even after 100 hours without high-pressure CO_2 while significant interdiffusion occurred under exposure to high-pressure CO_2. These ATR-FTIR spectroscopic images revealed the spatial distribution of both polymers and CO_2 during the process of interdiffusion and proved that the speed of interdiffusion can be tuned by changing CO_2 pressure. [79] Kazarian and Chan have investigated Polystyrene (PS)/poly(vinyl methyl ether (PVME) blends (representative LCST polymer blends) with high-pressure CO_2 using ATR-FTIR spectroscopic imaging. [12] It is the first time for the high-pressure CO_2-induced phase separation in LCST polymer blends to be visualized through using spectroscopic imaging. [12] However, the whole dynamic process hasn't been revealed through producing time-dependant spectroscopic images so that the extent of phase separation under different conditions cannot be compared.

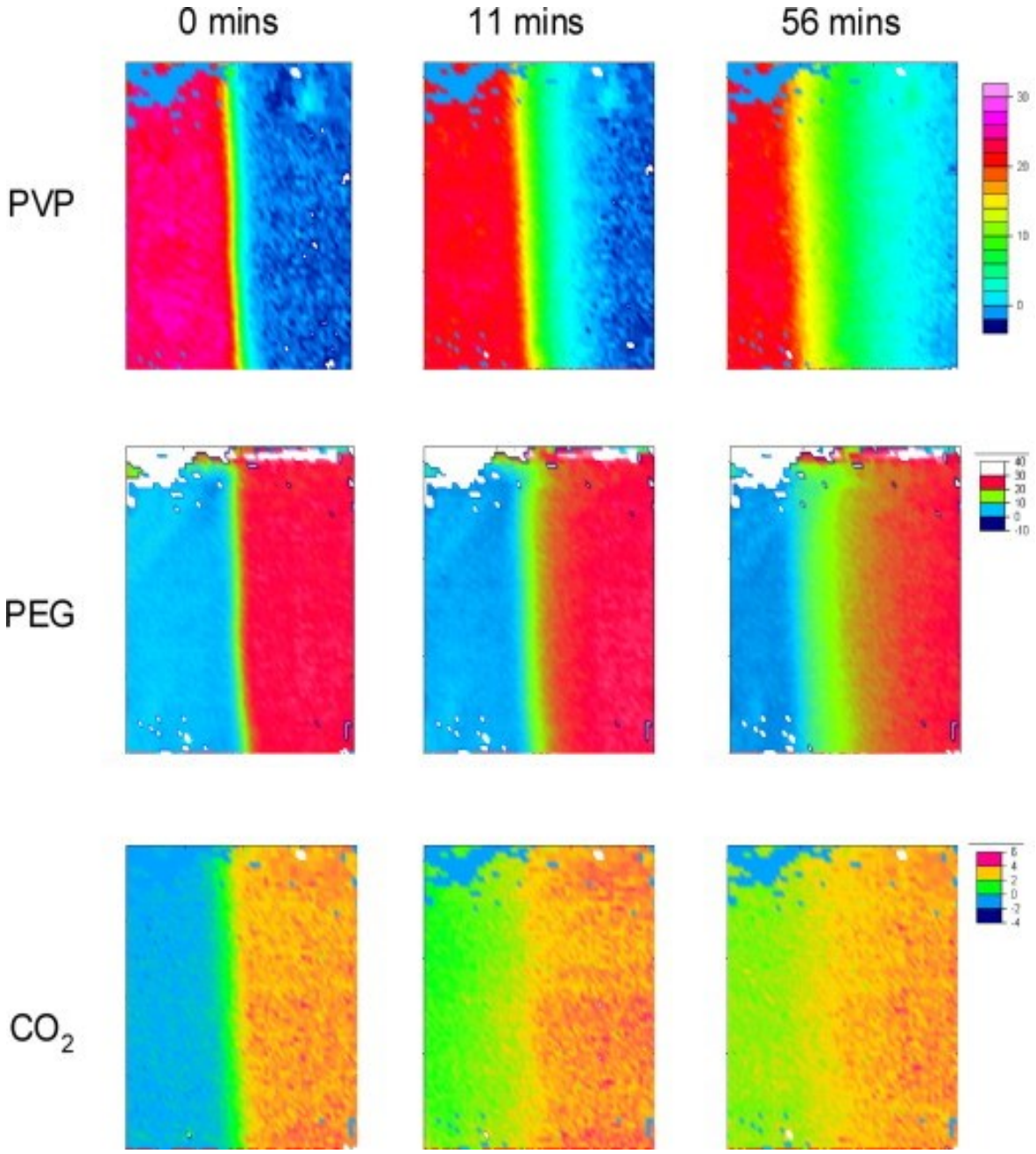

Figure 2.8 ATR-FTIR spectroscopic images of PVP/PEG 600 interface under exposure to 40 bar CO_2. The top images are based on the spectral band of PVP, the middle images are based on the spectral band of PEG, and the bottom images are based on the spectral band of CO_2. (Source [79]**)**

2.5.2 Investigation of inter- and intramolecular interactions in polymers

Inter- and intramolecular interactions in polymers have effects on the polymer properties and thus have implications on their synthesis and processing. [80] For instance, the hydrogen bond in the poly (ethylene glycol) (PEG)/ polyvinylpyrrolidone (PVP) blend leads to the unique adhesive and elastic properties, which are important to pharmaceutical products, such as transdermal delivery devices. [56]

FTIR spectroscopic imaging can reveal the component-rich domains and component-poor domains in the imaged area but it can not provide information about the areas where inter- and intramolecular interactions occur. In order to highlight the areas where chemically or physically meaningful variations occur, Shinzawa and co-workers have introduced a novel technique named disrelation mapping. Its detailed fundamentals have been described in section 2.3. In their study, poly(methyl methacrylate) (PMMA)/ PEG blends with different molecular weights were investigated as an example to visualize the molecular interactions. Firstly, disrelation spectra were prepared to indicate which two wavenumbers have different trends in the spectral absorbance variation. Then, the disrelation maps based on the disrelation intensity between these two wavenumbers were prepared and shown in figure 2.9. The intermolecular hydrogen bonding between PMMA and PEG at the boundary of these two polymers was visualized for the first time. The strength of hydrogen bonding can also be compared through detecting the strength of disrelation intensity. [46]

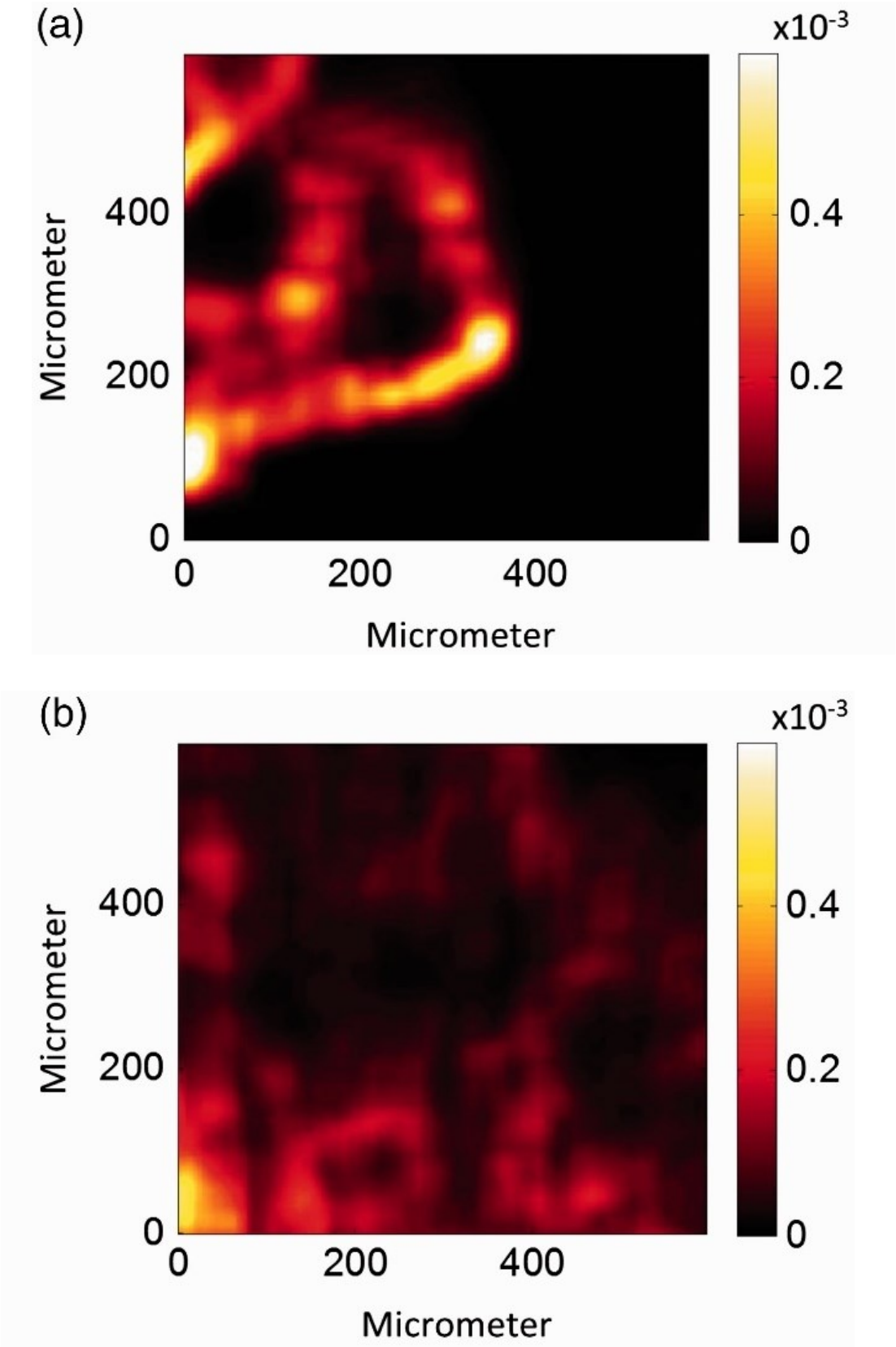

Figure 2.9 Disrelation maps of (a) PMMA/PEG-2000000 and (b) PMMA/PEG-2000 blends calculated with disrelation intensity between 1730 and 1714 cm^{-1}. (Source [46])

2.5.3 Investigation of polymer crystallization

The crystallization of polymers, which is a process of transitioning polymers from entangled melts to an ordered structure, can be induced by many factors, such as solvent, temperature and strain. Higher degree of crystallization results in greater hardness and brittleness while lower degree of crystallization results in greater ductility and toughness, which are required for many plastics applications. [67] The isothermal crystallization process can be divided into two types: melt-crystallization and cold-crystallization. The first one is to decrease the temperature below T_{mc} (upper critical crystallization temperature) to induce crystallization and the latter one is to increase the temperature beyond T_c (lower critical crystallization temperature) to induce crystallization. These two types of isothermal crystallization result in different crystal modifications and intermolecular interactions. [66,81–83]

Compared with high-pressure DSC and X-ray diffraction (XRD), ATR-FTIR spectroscopy is suitable to monitor the fast crystallization process in situ because it facilitates faster screening with shorter acquisition times. [12]. It can reveal the polymer morphologies, crystallization kinetics and crystalline form via significant changes in the FTIR spectra,[23] which benefits the understanding and development of polymer processing.[13] To be more specific, it can detect the formation of helical chains and chain segment conformations as well as the local molecular environment of polymers through the absorbance change and peak shift in different spectral bands. [81,84–87]

Melt-crystallization of polymers is worthy of investigation because the increasing undercooling has two opposing factors on it: increasing thermodynamic driving force and decreasing polymer chain mobility. Zhang et al. investigated the melt-crystallization process of PHB using FTIR spectroscopy and 2D correlation spectroscopy.[84,88] 2D correlation spectroscopy can differentiate the highly overlapped bands of ester groups in the PHB spectrum into single bands. The cross-peaks in the asynchronous spectrum indicate the sequential order of spectral intensity variation in these C=O group bands: 1743 cm^{-1} (1747 and 1739 cm^{-1}) >1731 cm^{-1} > 1722 cm^{-1}. The abnormal sequential order implies the appearance of an intermediate state, The results revealed the sequence of structural adjustment of polymer chains in the melt-crystallization process of PHB: the ester groups adjust their conformation at first, followed by longer regular 2_1 helix chains and then the regular 2_1 helix chains. PHB crystallizes into a 2_1-helix with an approximately g^+g^+tt

conformation, and the crystal structure of isolated PHB consists of an orthorhombic unit cell which contains two left-handed helical molecules in antiparallel orientation. [88] Another study investigated the influence of crystalline structures of PLA on its hydrolysis process. It was found that the hydrolytic degradation behaviour of PLA depends on the crystal form (α′- or α-form) and degree of crystallization. [81,88,89]

After investigating the melt-crystallization process of pure polymers, PHB/PLA blends were prepared and their crystallization behaviours were studied. During the crystallization process in the immiscible blend, PLA crystallization occurs at a higher temperature and then PHB crystallization occurs at a lower temperature. However, in the miscible PHB/PLA blend (their T_m are close), almost simultaneous crystallization (crystallization at the same annealing temperature) can be observed. As a result, it can be demonstrated that the crystallization behaviour of both blend components is greatly affected by the miscibility of polymer blend. [84] The detail of this effect will be further investigated in chapter 6.

Since the conventional spectroscopy can not provide the spatial information, the solvent-induced crystallization of syndiotactic polystyrene (s-PS) was studied utilizing transmission FTIR spectroscopic imaging. As shown in figure 2.10, the movement of solvent into the polymer and the distribution of induced crystalline polymer in the imaged area were visualized. Through the obtained time-resolved FTIR images, polymer crystallization kinetics and solvent diffusion coefficients can be calculated and thus the type of diffusion was demonstrated to be Fickian diffusion. As a consequence, it was concluded that solvent diffusivity is the main limiting factor in the crystallization process because this process can only be initiated with enough solvent. [90]

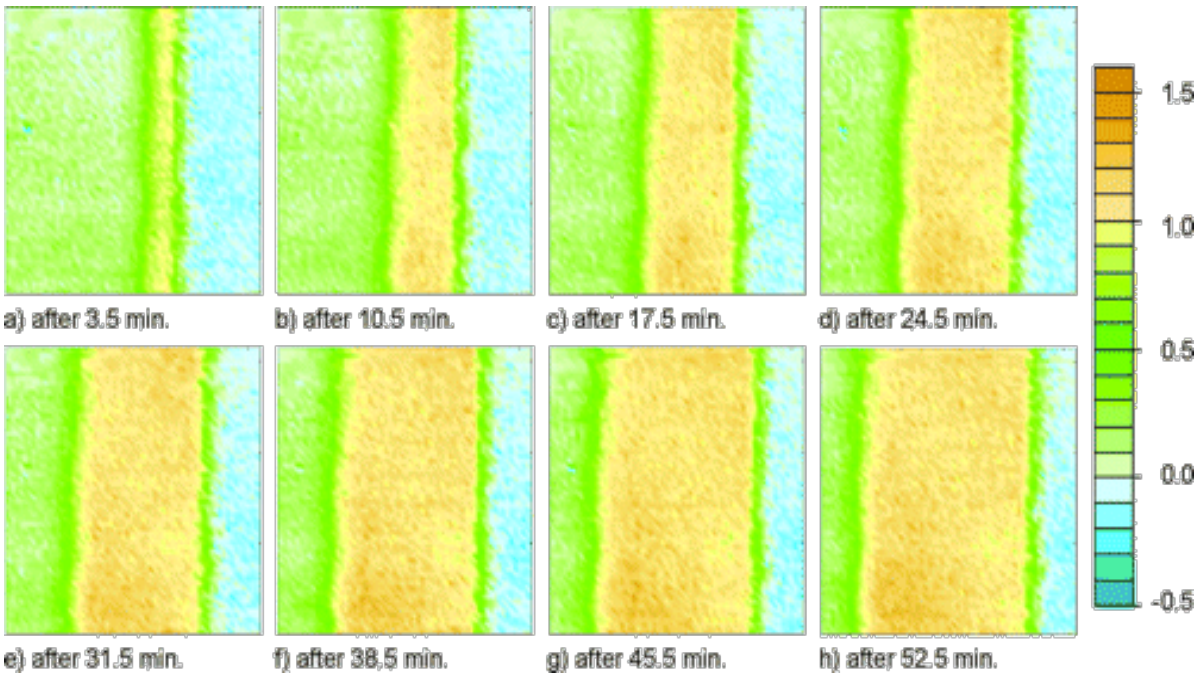

Figure 2.10 FTIR images based on the distribution of the integrated absorbance of the band at 1275 cm^{-1} (crystalline s-PS) as a function of solvent exposure time. (Source [90]**)**

2.5.4 Conclusion

In summary, this chapter has summarised some of the important discoveries associated with the application of spectroscopic techniques for polymer characterization. These discoveries have been proved to be beneficial for the greater understanding of the modification and behaviour of the polymeric materials and systems. Moreover, the research gap was identified and summarized as following:

1. FTIR spectroscopic imaging is a powerful experimental tool to study the dynamic polymeric systems. As mentioned in section 3.2, our lab introduced and developed in situ high-pressure ATR-FTIR imaging, which has been used to study polymer interdiffusion under high-pressure CO_2 previously. [79] However, the dynamic process of phase separation in LCST polymer blends under high-pressure CO_2 hasn't been visualized before. This technology laid the basis for the study of high-pressure CO_2-induced phase separation in polymer blends.

2. 2D disrelation map, as an extension of conventional 2D correlation analysis, has been applied to visualize the intermolecular hydrogen bonding between PMMA and PEG in the partially miscible PMMA/PEG blend. The strength of hydrogen bonding was compared through detecting the strength of disrelation intensity. [46] In this project, it is the first time for this new technology to be applied to visualize the interaction occurring in the polymer interfaces before and under exposure to high-pressure CO_2. The high-pressure CO_2-weakened specific inter- and intramolecular interaction between polymers will be demonstrated through detecting the strength of disrelation intensity.

3. The isothermal crystallization process of UCST crystallizable polymer blend from the immiscible molten state to the immiscible crystalline state and from the miscible molten state to the miscible crystalline state have been investigated. However, without the capability to visualize the phase separation, the isothermal crystallization process of this type of blend from the miscible molten state to the immiscible crystalline state cannot be detected. In this project, phase separation and crystallization in the PHB/PLA blend will be visualized simultaneously using ATR-FTIR spectroscopic imaging.

4. The spectroscopic images based on integrated absorbance can reveal the spatial distribution of each blend component in the polymer blend. But they cannot reflect the spatial distribution of inter- and intramolecular interactions in polymer blends. In this thesis, spectroscopic images based on the band position will be used to investigate changes in intra- and intermolecular interactions in PHB/PLA blends during the isothermal melt crystallization.

Chapter Three

Experimental apparatus and methods

3. Experimental apparatus and methods

3.1 ATR-FTIR spectroscopy

To obtain the conventional ATR-FTIR spectra of samples, an Equinox 55 FTIR spectrometer (Bruker Corp.) with a mercury-cadmium-telluride (MCT) detector was used, which is shown in figure 3.1. The MCT detector needs to cool with liquid nitrogen. The chosen ATR crystal in the ATR accessory for this work is diamond (refractive index: 2.4), where the measuring surface is 2×2 mm^2. The samples are placed on the surface of diamond during measurement. Good contact between sample and diamond is ensured through pressing the sample with a stainless steel flat anvil of the ATR accessory. The spectral resolution is 4 cm^{-1} and the number of co-added scans is 64. The obtained data are treated by OPUS (Bruker Corp.) and MATLAB.[91] The main purpose of using the conventional ATR-FTIR spectroscopy is to record spectra of pure samples and then identify the unique spectral bands to generate the ATR-FTIR spectroscopic images.

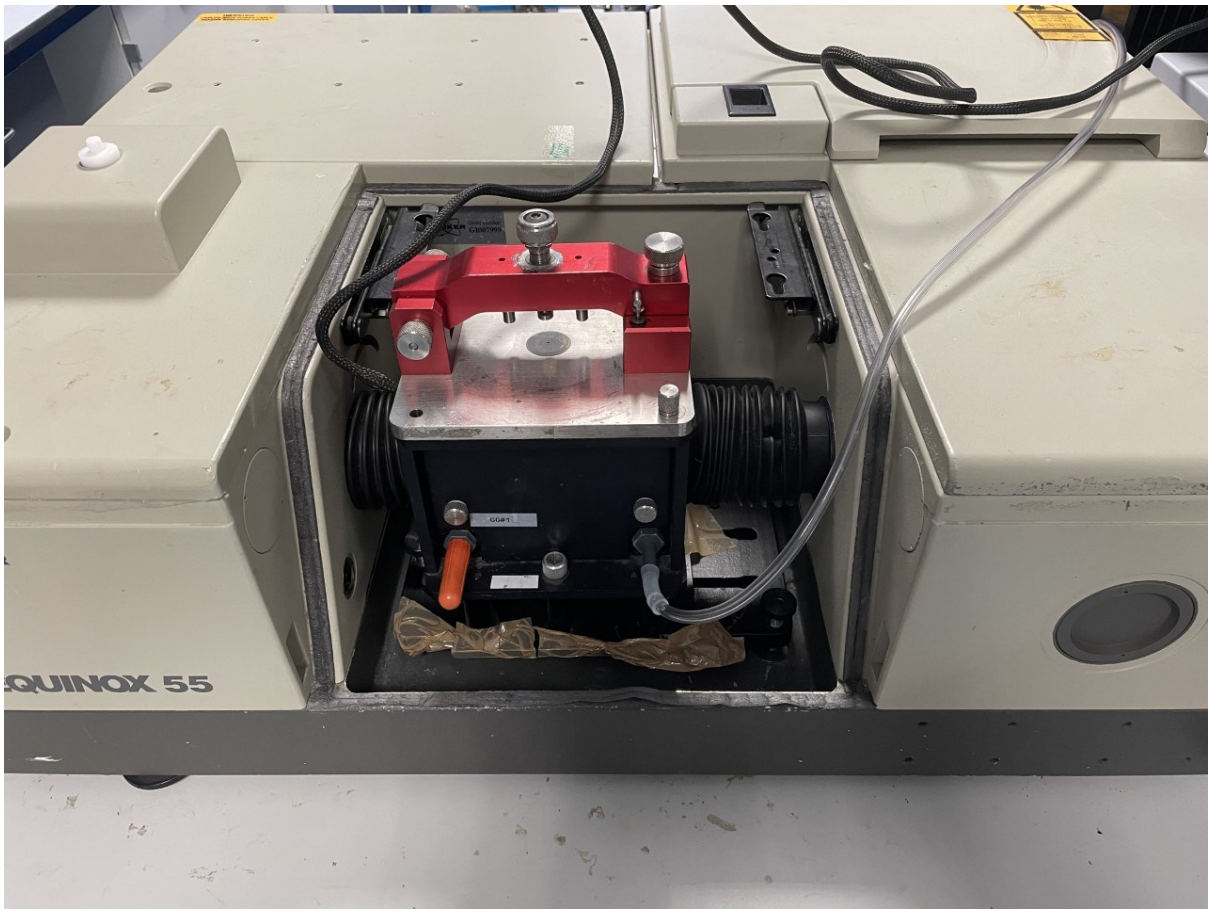

Figure 3.11 Photograph of the Equinox 55 FTIR spectrometer (Bruker Corp.) with a mercury-cadmium-telluride (MCT) detector.

3.2 ATR-FTIR spectroscopic imaging system

As shown in figure 3.2, a Tensor 27 FTIR spectrometer (Bruker Corp.) is combined with an IMAC macrochamber (Bruker Corp.) for housing a 64 x 64 FPA detector (Santa Barbara Focal plane, USA) and an Imaging Golden Gate™ ATR accessory (Specac, UK). The IMAC macrochamber is also called a large sample compartment.

The spectrometer is purged with dry air all the time to avoid the effect of the change in humidity on the measurement. When the sample is placed on the ATR crystal, background measurement can no longer proceed so that the following measurements will use the same background spectra obtained at the start of experiment. Thus, it is vital to keep the concentration of water and CO_2 constant in the imaging system during the whole process of measurement.

The liquid nitrogen-cooled FPA detector is connected to the spectrometer. FPA detectors were only used for military purposes in the past and now their usage is extended into scientific research. Its size is 64×64 pixels, which means that it can divide the imaged area into 64×64 pixels and then measure 4096 spectra within the sample in one single measurement.

Spectral information in the mid-IR region: 3900-850 cm^{-1} was recorded. The spectral resolution is 4 cm^{-1} and the number of co-added scans is 64. These chosen parameters make the signal-to-noise (S/N) ratio sufficiently high and measurement time short enough. After data collection, the obtained spectra are treated using OPUS (Bruker Corp.) and MATLAB. Two-dimensional ATR-FTIR spectroscopic images are formed through plotting the distribution of the integrated absorbance of chosen spectral bands for all pixels. The value of integrated absorbance is indicated in the colour bar next to these images, where red represents a high concentration and blue represents a low concentration for the corresponding component. [9]

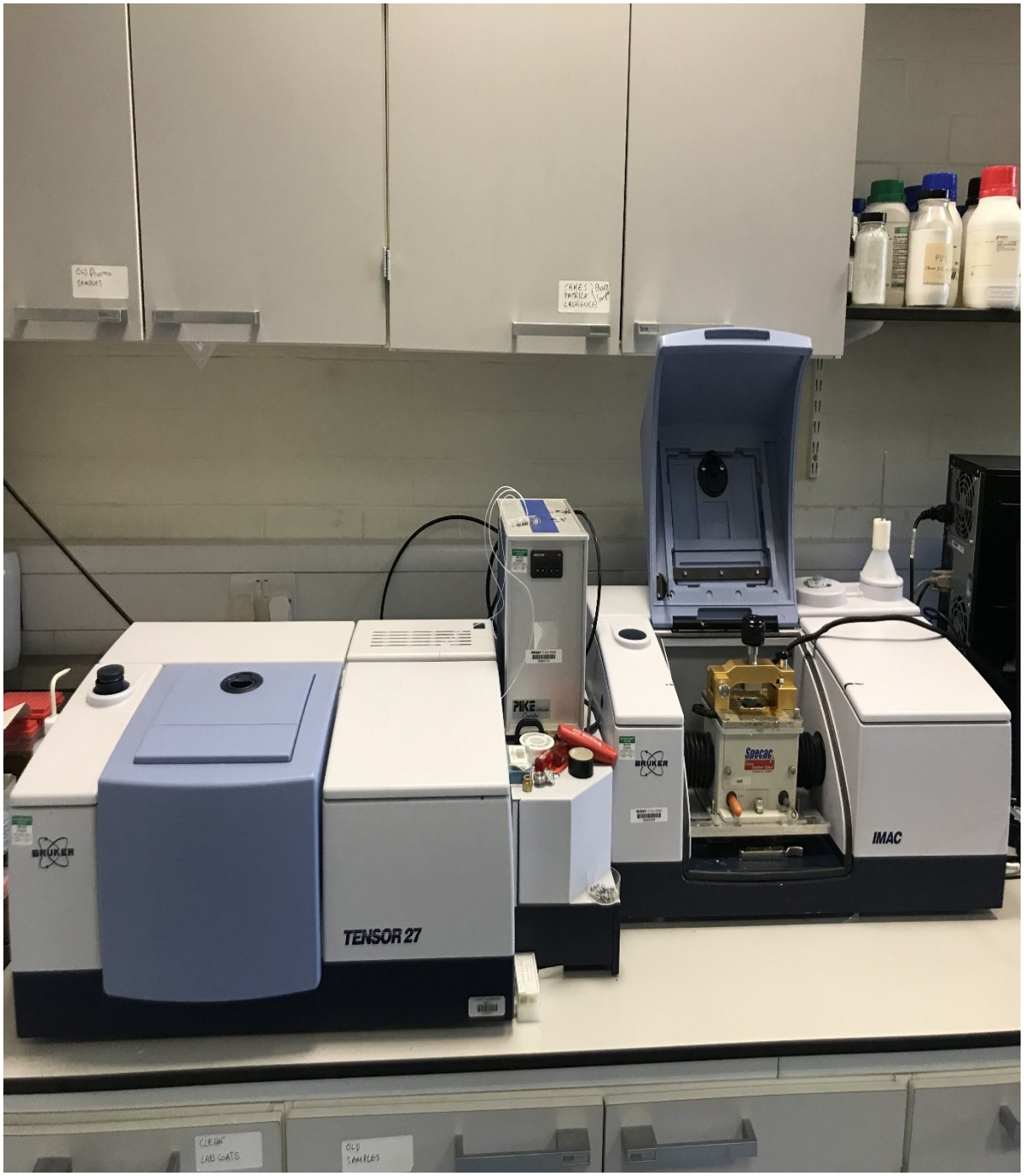

Figure 3.12 Photograph of the ATR-FTIR spectroscopic imaging system. The Imaging Golden Gate™ ATR accessory is in the IMAC macrochamber.

3.2.1 ATR imaging accessory

As shown in figure 3.3, the imaging accessory used for the macro FTIR spectroscopic imaging measurement is an Imaging Golden Gate^{TM} ATR accessory (Specac, UK) with diamond (refractive index: 2.4), shaped like an inverted prism. The ATR accessory is aligned exactly in the macrochamber to ensure that the IR beam can go through the ATR crystal and then reach the detector. If the alignment is not good, spatial resolution, image quality and S/N ratio will all be affected. Corrective optics in the accessory can account for distortion. A heater is connected to the ATR accessory so that the effect of changing temperature on samples can be investigated and temperature during experiments can be controlled more accurately. Some advantages of this accessory are the capability for in situ measurement, a high mechanical strength for compression and the ease of cleaning, which can improve the reproducibility of the spectroscopic images.

The size of produced spectroscopic images is 0.6 mm × 0.55 mm (length × width) with a spatial resolution of approximately 15–20 μm. [30,32,33] The high spatial resolution makes it suitable for studying the interface between two different polymers. [15] But it can only detect the morphology of microstructure, such as a discrete phase structure in matrix. The nanostructure, such as polymer blends with a bicontinuous phase structure, is not visible in these ATR-FTIR images.[92,93]

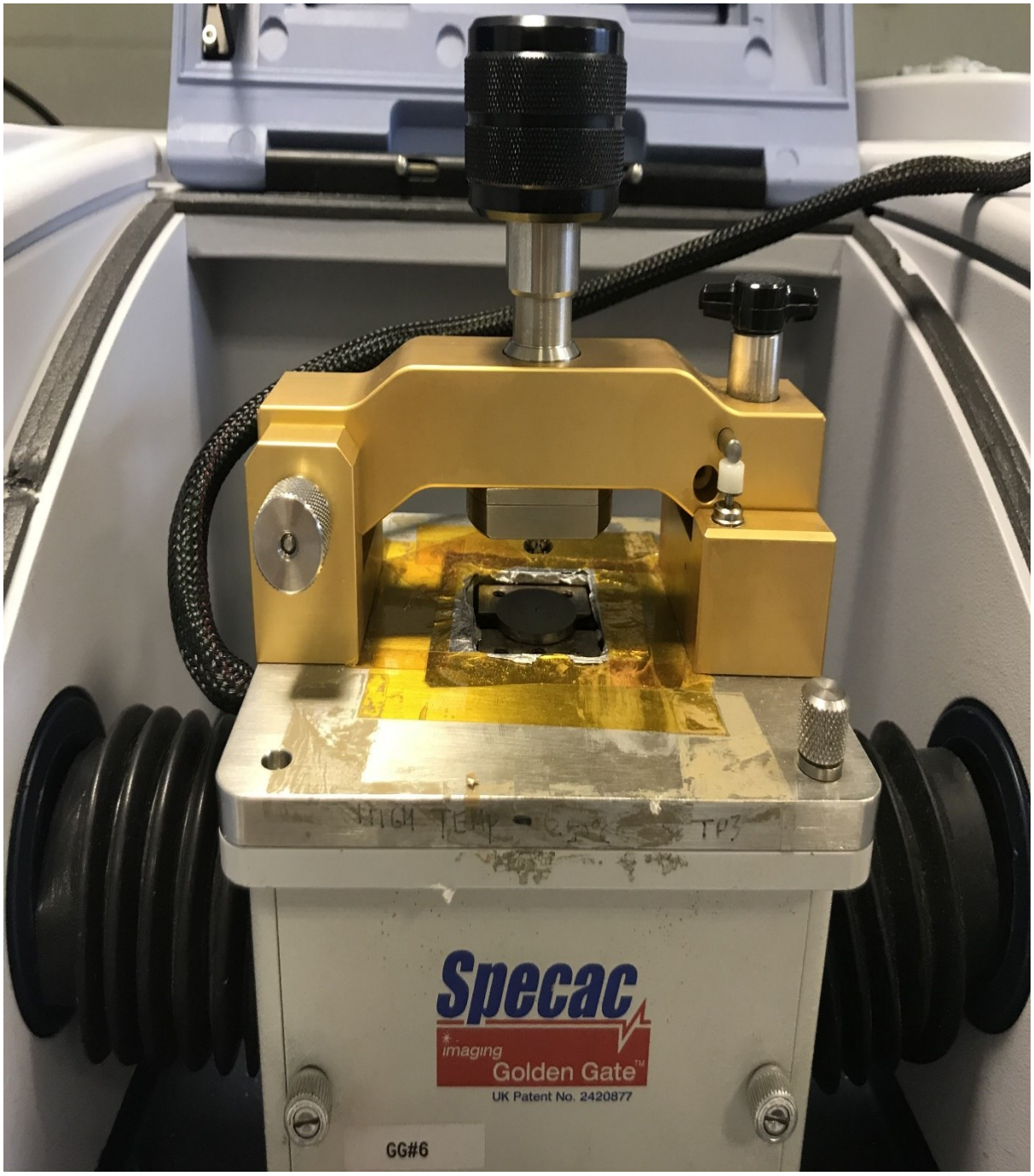

Figure 3.13 Photograph of the Imaging Golden Gate™ ATR accessory in the IMAC macrochamber.

3.3 High-pressure set-up

The investigation of polymers under high-pressure CO_2 requires the high-pressure apparatus. The Kazarian research group has developed a specially designed high-pressure experimental

apparatus to introduce high-pressure CO_2 to the sample. It is made up of a spectroscopic cell, a syringe pump, a pressure transducer, pipes and valves. The miniature homemade high-pressure stainless steel cell has a small volume so that the risk of apparatus failure can be reduced. It is placed on the diamond support plate (tungsten carbide plate) and held in position by a stainless steel flat anvil of the accessory mentioned above. This cell is the key part of the high-pressure set-up. Apart from the small volume, there are two factors: no fragile window is on the cell and the ATR crystal is very hard, which can also reduce the risk of apparatus failure. [12]

A high-pressure syringe pump (Teledyne 500D, Isco, USA) is used to supply CO_2. Temperature regulation is realized using a heater connected to the heating plate of accessory. Pressure regulation is realized using a digital pressure transducer (Swagelok, Germany), which is shown in figure 3.4. During the measurement, the sample is positioned directly on the ATR crystal and then covered with the spectroscopic cell. The thickness of polymer film should be higher than the penetration depth of evanescent field but not too thick so that CO_2 can penetrate the bulk area of the film easily. Sealing of the cell is achieved using a Polytetrafluoroethylene (PTFE) O-ring, which can endure up to 120 bar CO_2 at 30°C. The schematic diagram of in situ high-pressure ATR-FTIR spectroscopic imaging is shown in figure 3.5. Measurements should be taken after the polymer samples reach equilibrium.

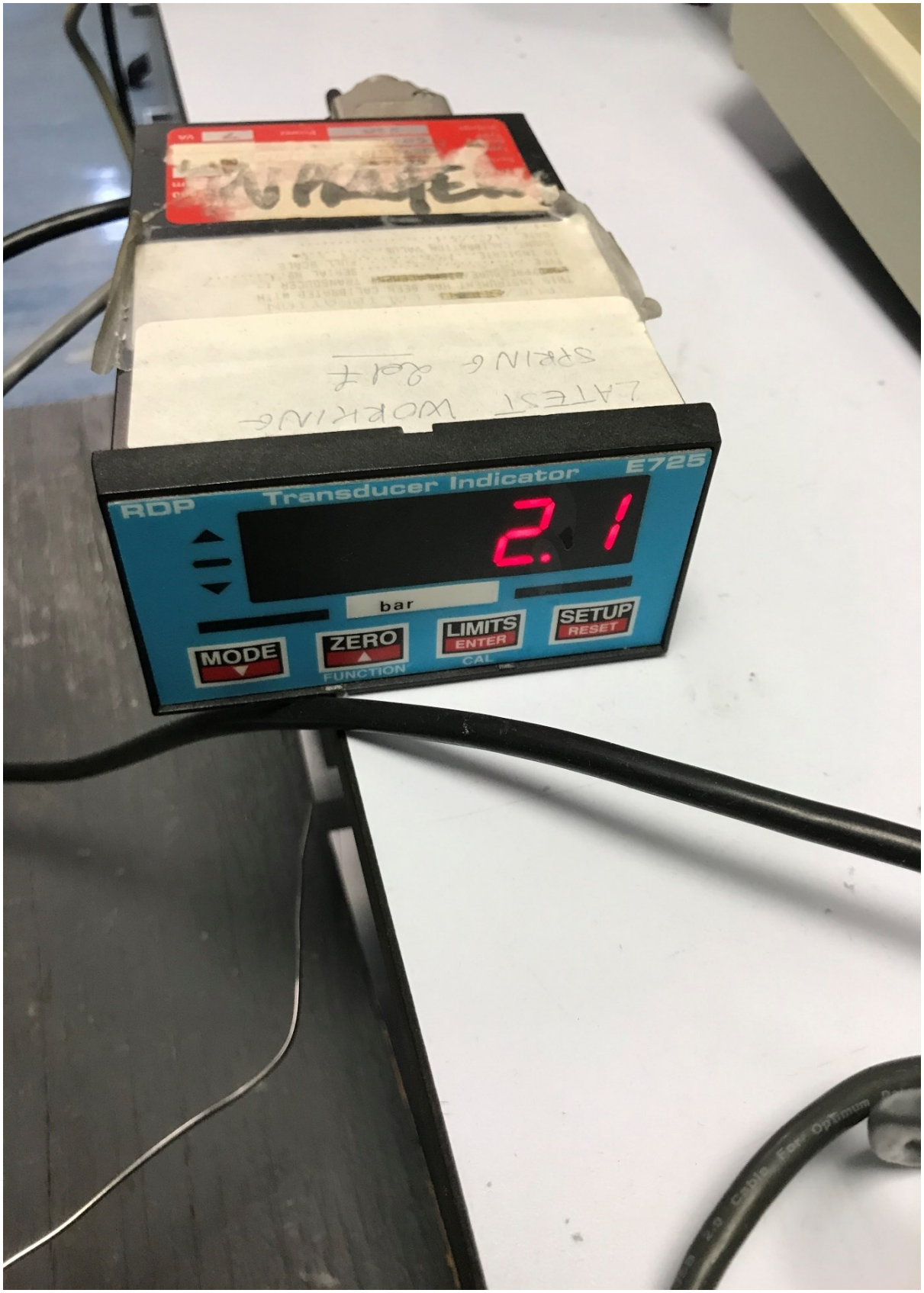

Figure 3.14 Photograph of the digital pressure transducer

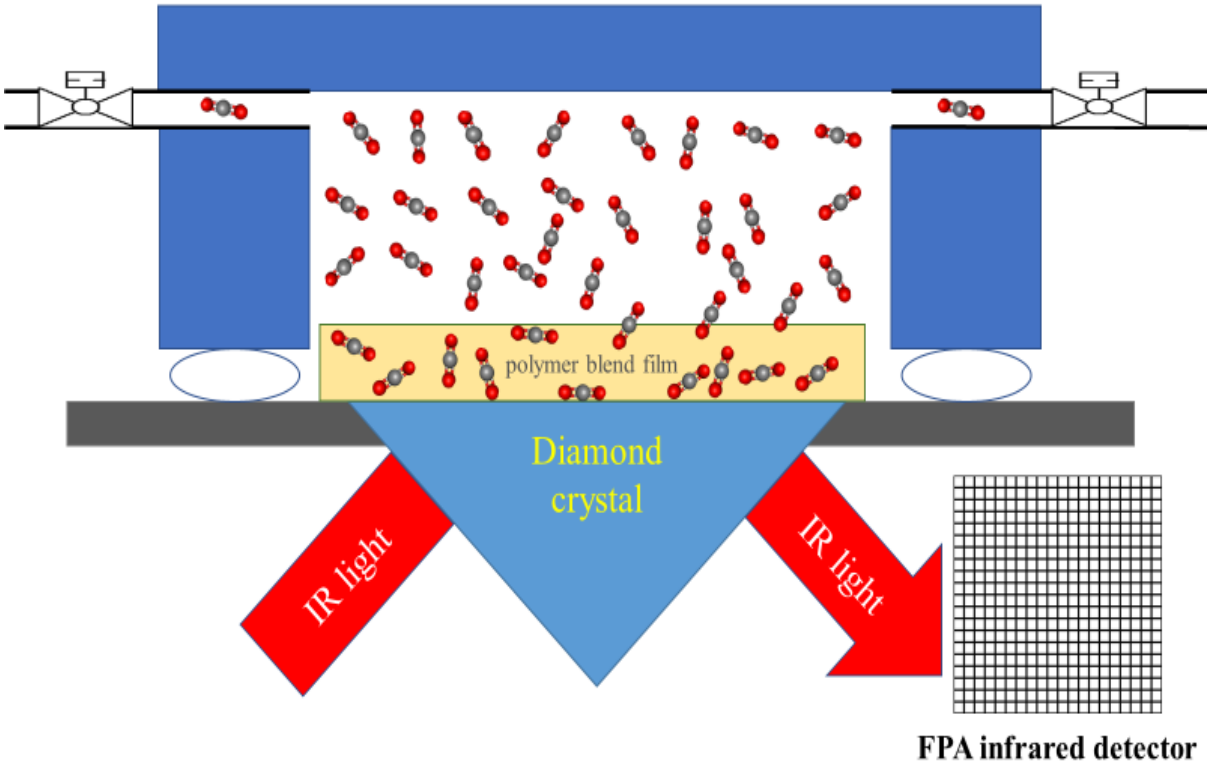

Figure 3.15 Schematic diagram of in situ high-pressure ATR-FTIR spectroscopic imaging showing the polymer blend film under high-pressure CO_2. The grid is the schematic of FPA detector. (Source [9])

Chapter Four

Visualization of phase separation in PCL/PLA blends under high-pressure CO_2 using in situ ATR-FTIR spectroscopic imaging

4. Visualization of phase separation in PCL/PLA blends under high-pressure CO_2 using in situ ATR-FTIR spectroscopic imaging

This chapter presents the application of in situ high-pressure ATR-FTIR spectroscopic imaging to study the phase separation in PCL/PLA blends under exposure to high-pressure CO_2. PCL/PLA blends are representative lower critical solution temperature (LCST) polymer blends, which indicates that they are miscible below the critical solution temperature for all compositions. [94] This work visualized the dynamic process of phase separation in PCL/PLA blends under high-pressure CO_2 in order to provide an insight into their physical properties. [9]

The first part of this chapter describes phase separation in PCL/PLA blends with increasing temperature or under high-pressure CO_2 studied by ATR-FTIR spectroscopic images. The second section of this chapter focuses entirely on the comparison of the extent of phase separation in this blend under different conditions through observing the morphology change of PCL-rich domains and PLA-rich domains in the obtained spectroscopic images. It is found that increasing temperature, CO_2 pressure and exposure time can all enhance the extent of phase separation in this blend under exposure to high-pressure CO_2. Finally, a mechanism of this type of phase separation was proposed. [9]

4.1 Motivation and scientific background

Because of its complementary rheological properties, relatively low cost and excellent mechanical properties, biopolymer blend of PCL and PLA has attracted a great deal of interest. [95] It can be used in packaging because of its biodegradability and tissue engineering since it is biocompatible. PCL is a semicrystalline thermoplastic and PLA is a linear aliphatic thermoplastic polyester. [96] As biopolymers, they can not only be produced through ring opening polymerization but also be derived from renewable resources. Like composites, the advantages of PCL (high flexibility) and PLA (high stiffness and tensile strength) can be combined. [9,95]

As a popular biopolymer blend, the mechanical, rheological, viscoelastic properties [97], thermal stability [98] and shape memory behaviour [99] of PCL/PLA blends have been investigated previously. However, because of the challenges of experiments, the studies of the morphology of this blend under high-pressure CO_2 are limited. As mentioned in chapter 2, high-pressure CO_2 may benefit the chemical industries especially polymer industries. Thus, an increase in the knowledge of the morphology of polymer blend/CO_2 systems under different conditions is needed for the process development and implementation. It can reveal the processing window for PCL/PLA blends and high-pressure CO_2. In addition, it is vital to know when possible phase separation will occur in the products containing PCL/PLA blends when they are used under exposure to high-pressure CO_2, so that this phenomenon can be mitigated.[9]

4.2 Materials and methods

4.2.1 Materials

PCL (M_n=93,000) was bought from Perstorp UK Ltd. PCL (M_n=10,000) was bought from Sigma-Aldrich. PLA (M_w=240,000) was bought from Biomer. The chemical structures of PCL and PLA are shown in Figure 4.1. CO_2 (99.9% pure) was supplied by BOC. All of them were used as received without further treatment.[9]

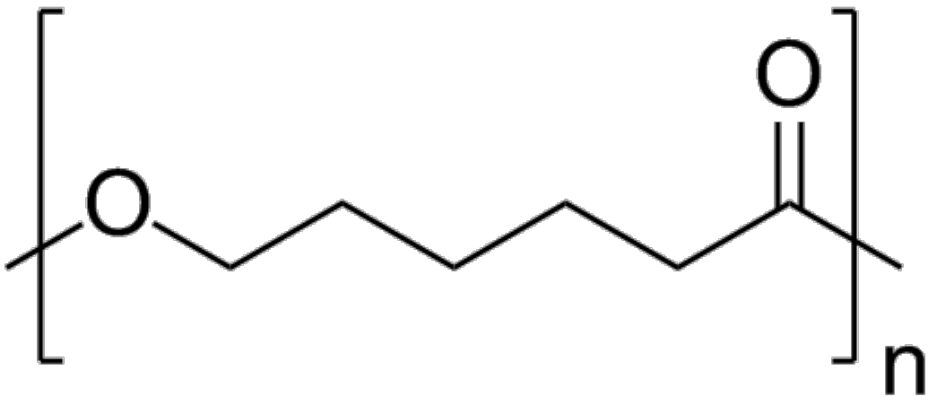

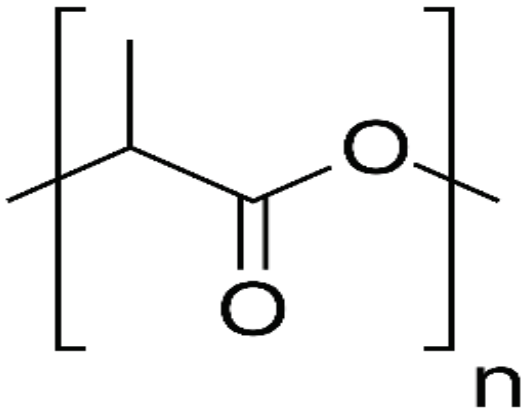

Figure 4.16 Chemical structures of PCL (top) and PLA (bottom). (Source [15])

4.2.2 Polymer blend preparation

Because moisture can affect both chemical and physical properties of polymers, PCL and PLA were placed in a vacuum desiccator for 24 hours at room temperature to remove moisture. [100] Then both of these dried polymers were dissolved together in a suitable solvent: chloroform (99.2% chloroform, 0.8% ethanol) with the weight ratio (50wt%:50wt%). The obtained solution was poured into a Soda glass specimen tube with a rotator and then stirred (300 rpm) overnight on a hot plate (MS-H280-Pro). To avoid the phase separation of polymer blends until measurement, the polymer blend solution was stirred continuously after the complete dissolution of polymers. The solution was then cast directly on an ATR crystal, diamond to form polymer blend film. Several measurements were taken before the formal data collection to ensure that chloroform was totally removed and the sample was at homogeneous and equilibrium state.[9]

4.2.3 High-pressure experimental apparatus

The high-pressure set-up is detailed in section 3.3.

4.2.4 In situ macro ATR-FTIR spectroscopic imaging measurements

An Alpha FTIR spectrometer (Bruker Corp.) was used to measure the conventional ATR-FTIR spectra of each component in PCL/PLA blends, separately. A Tensor 27 FTIR spectrometer (Bruker Corp.), as detailed in section 3.2, was applied to measure the ATR-FTIR spectroscopic images with an FPA detector. A spectral resolution of 4 cm^{-1} and 64 co-added scans were applied. [9]

4.3 Results and discussion

4.3.1 The comparison of effect of heat and high-pressure CO_2 on the phase separation of polymer blends

First of all, the conventional FTIR spectrometer was used to measure the ATR-FTIR spectra of pure PCL (M_n=10,000) and PLA. As shown in figure 4.2, spectral bands relevant to PCL at 1721 cm^{-1} and spectral bands relevant to PLA at 1083 cm^{-1} are well separated and clearly distinguishable. Thus, the integration ranges used to generate spectroscopic images were selected as follows: 1750-1700 cm^{-1} for PCL, 1115 cm^{-1}-1058 cm^{-1} for PLA and 2350 cm^{-1}-2300 cm^{-1} for CO_2. [9]

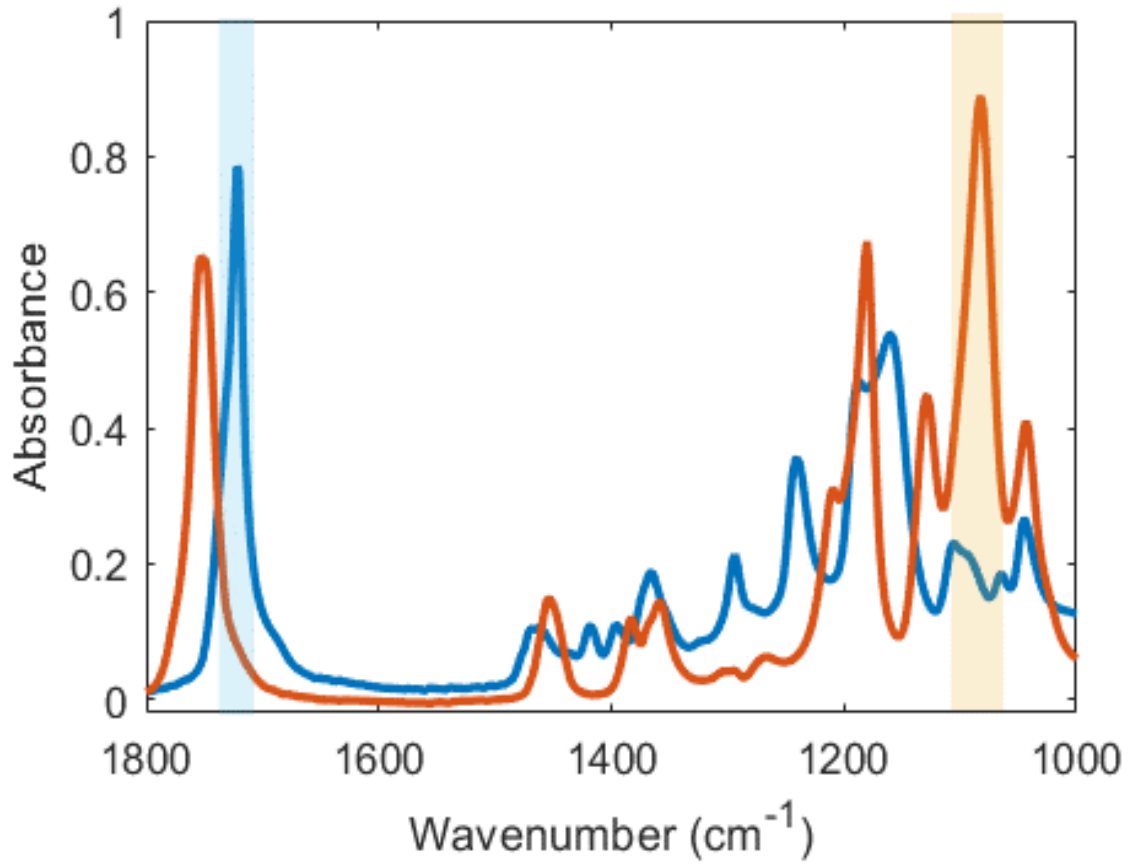

Figure 4.17 ATR-FTIR spectra of pure PCL (blue) and PLA (orange) at 30 °C (Source [9])

As shown in figure 4.3(a), the spatial distribution of PCL (M_n=10,000) and PLA in the polymer blend is revealed in these images. It is found that the concentration of PCL and PLA are nearly constant in the whole images at 20°C, which indicates the nearly homogeneous distribution of both blend components. With increasing temperature from 20°C to 130°C, PCL-rich domains, where contain a greater concentration of PCL, appear on the left side of the image while PLA-rich domains, where contain a greater concentration of PLA, appear on its bottom and right side. The spectra shown in figure 4.3(b) also prove that the concentration of PCL in the PCL-rich domain is greater than that in the PLA-rich domain while the concentration of PLA in the PLA-rich domain is also greater than that in the PCL-rich domain. Both of the spectroscopic images and spectra suggest that phase separation occurs in PCL/PLA blends after temperature increases. This is because, as an LCST polymer blend, the segments of PCL and PLA become more mobile to move at a higher temperature. The blend separates into two phases in order to keep the free energy of this system at its minimum. [6,9]

One of the limitations of these spectroscopic images is that it can only reveal the composition of bottom surface layer of polymer blend instead of its bulk. Phase separation in z-direction, which is vertical to the bottom surface, cannot be revealed.

(a)

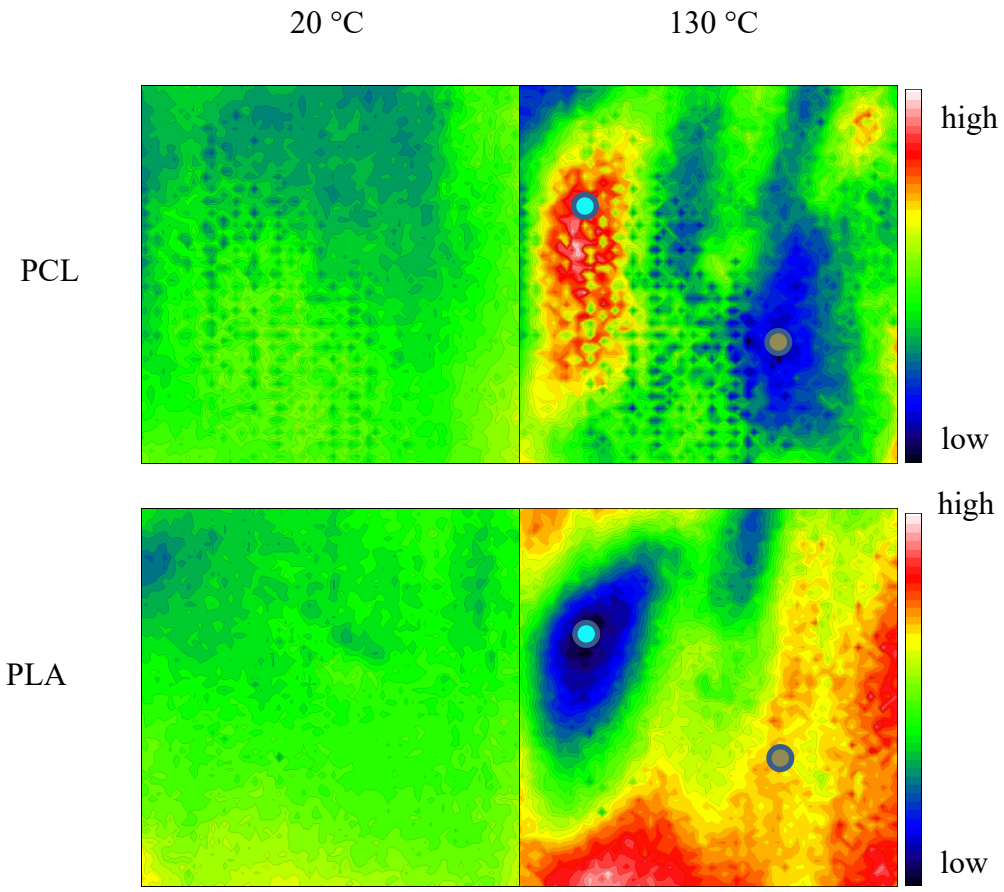

(b)

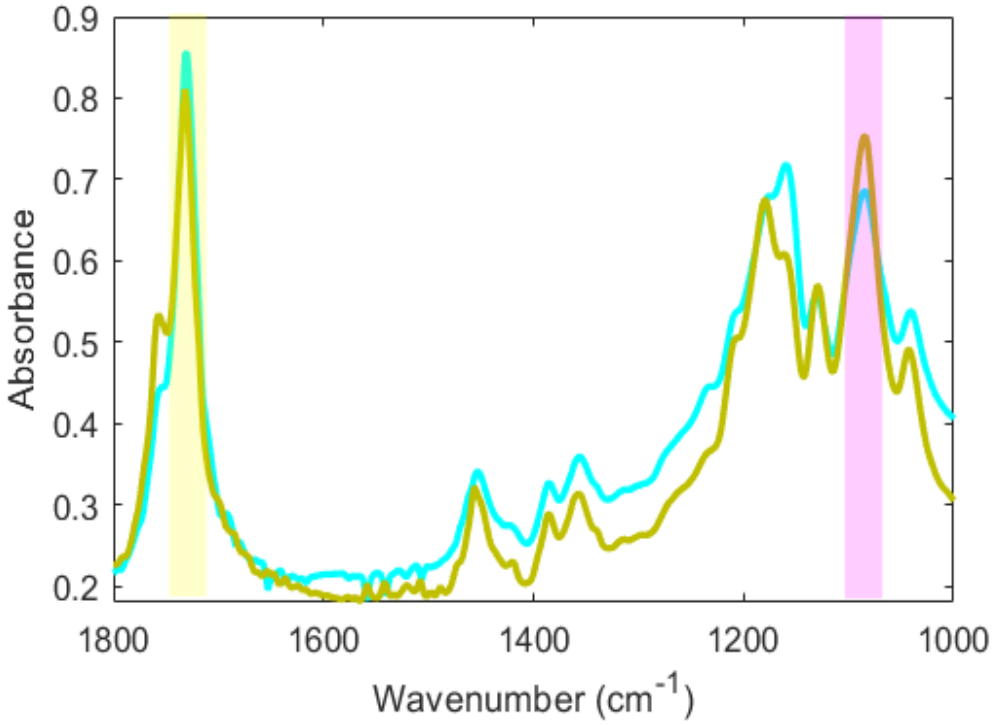

Figure 4.18 (a) ATR-FTIR spectroscopic images of the PCL (Mn=10000) and PLA blend at 20 °C (left) and 130 °C (right). The top images are based on the spectral band of PCL while bottom images are based on that of PLA. (b): spectra were extracted from the PCL-rich domain indicated by a blue circle in the top right image and the PLA-rich domain indicated by a brown circle in the bottom right image. (Source [9])

The following experiment measured PCL/PLA blends under high-pressure CO_2. Similar to heat, high-pressure CO_2 can also result in the increase of segmental and chain mobility. Figure 4.4 shows that CO_2 distributes homogeneously in the polymer blend, which is because the CO_2 sorption in both blend components is similar. Thus, the CO_2 sorption does not influence the relative concentrations of these two components in the blend. [9]

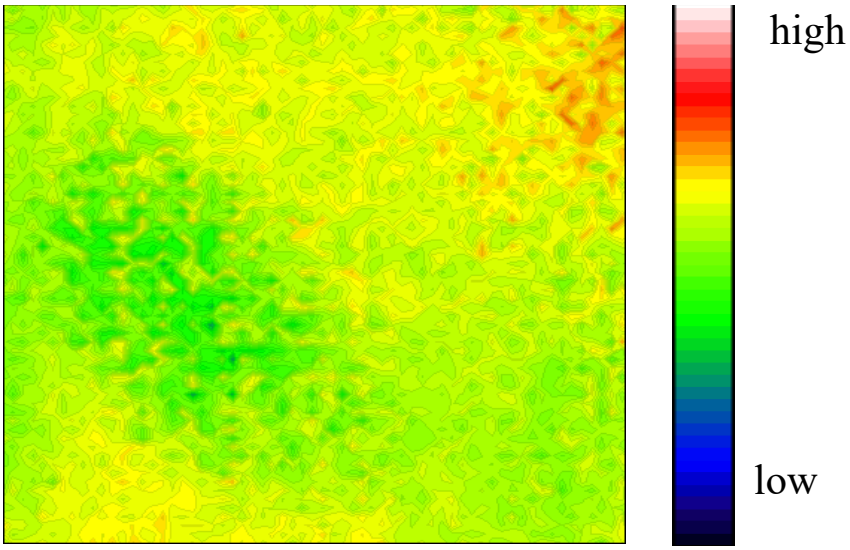

Figure 4.19 ATR-FTIR spectroscopic image of the PCL (Mn=10000) and PLA blend under exposure to 60 bar CO_2 at 30 °C. The image is based on the spectral band of CO_2. (Source [9])

Likewise, as shown in figure 4.5, both of the spectroscopic images and spectra indicate that the initial nearly homogeneous sample becomes inhomogeneous under exposure to high-pressure CO_2. It is because high-pressure CO_2 plasticizes the polymers and results in higher free volume, greater chain mobility and lower viscosity. Thus, the polymer blend separates into two components to reduce the free energy of this system. [6] To be more specific, the free energy of mixing obtained by Equation 4.1 should be negative when the distribution of polymer blend is homogeneous. This is because the Gibbs free energy should be minimum for any system at equilibrium. [9]

$$\Delta G_m = \Delta H_m - T\Delta S_m \qquad \text{(equation 4.1)}$$

$$\frac{\Delta G_m}{RTV} = \frac{\phi_1}{N_1} In\phi_1 + \frac{\phi_2}{N_2} In\phi_2 + \phi_1\phi_2\chi_{12} \qquad \text{(equation 4.2)}$$

Where ΔG_m is the free energy of mixing, ΔH_m is the enthalpy of mixing (heat of mixing), T is temperature, ΔS_m is the entropy of mixing. R is the gas constant, V is the volume of system, N_1 and N_2 are molar volumes of PCL and PLA, respectively. ϕ_1 and ϕ_2 are volume fractions of PCL and PLA, respectively. χ_{12} is the Flory interaction parameter. [68] [9]

(a)

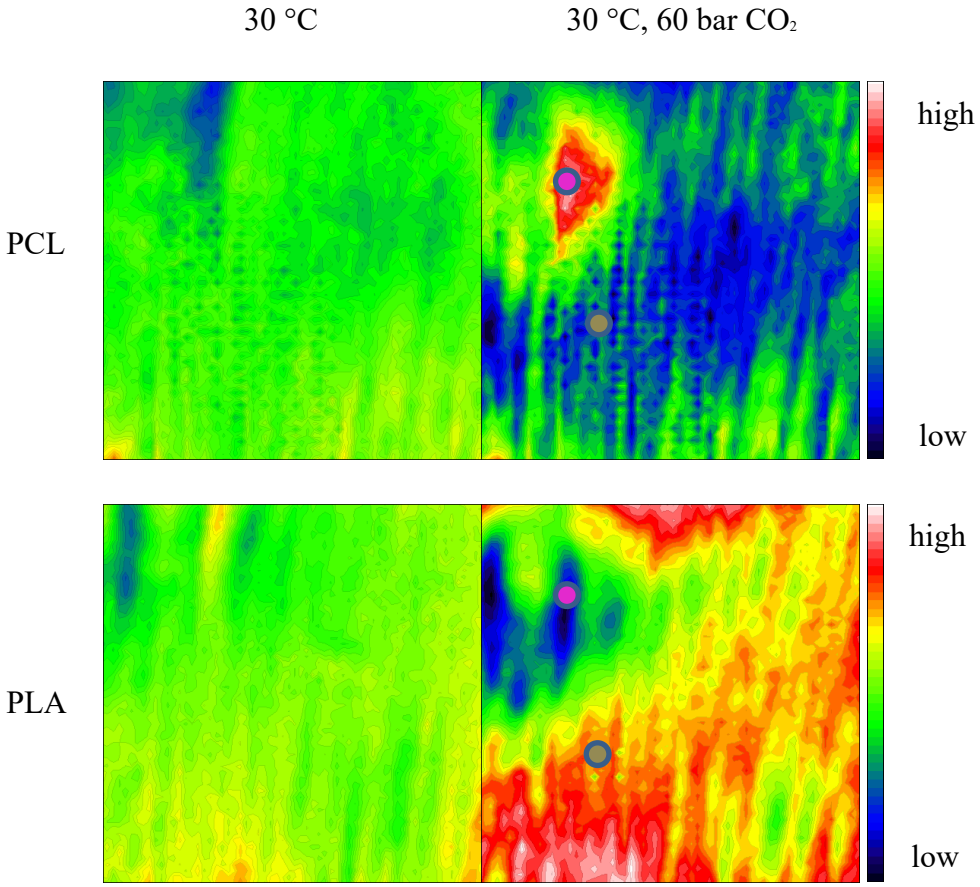
30 °C
30 °C, 60 bar CO2
PCL
high
low
PLA
high
low

(b)

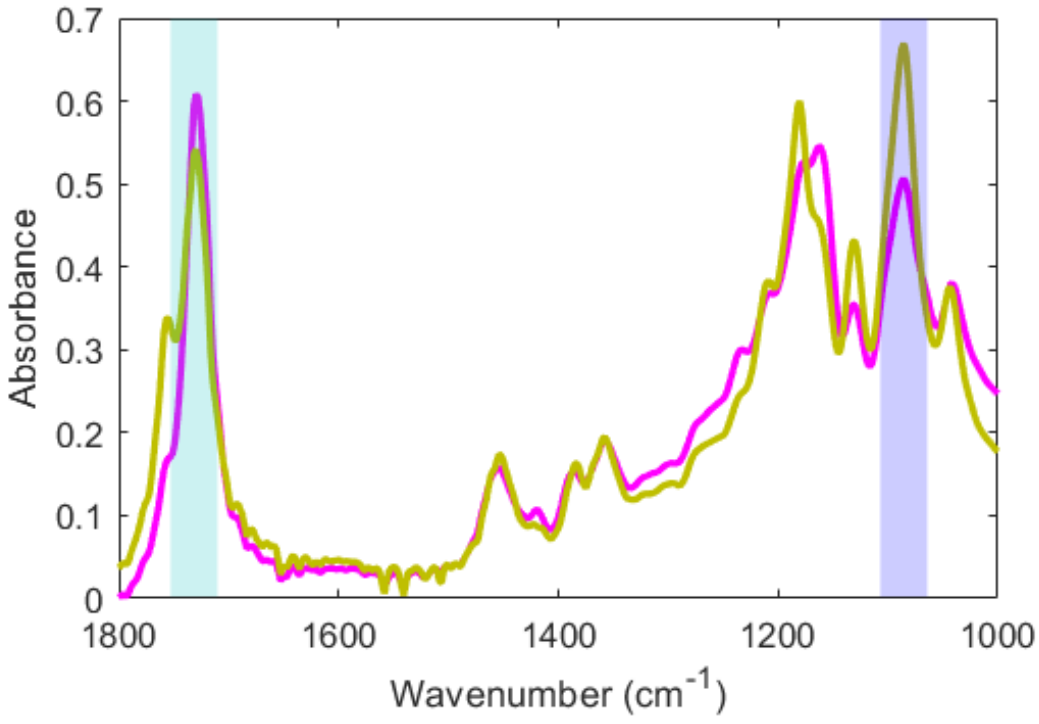
0.7
0.6
0.5
0.4
0.3
0.2
0.1
0
Absorbance
1800
1600
1400
1200
1000
Wavenumber (cm-1)

Figure 4.20 (a) ATR-FTIR spectroscopic images of the PCL (Mn=10000) and PLA blend before (left) and under exposure to 60 bar CO_2 (right) at 30 °C. The top images are based on the spectral band of PCL while bottom images are based on that of PLA. (b): spectra were extracted from the PCL-rich domain indicated by a pink circle in the top right image and the PLA-rich domain indicated by a ginger circle in the bottom right image. (Source [9])

Hydrostatic pressure has little impact on the miscibility of LCST polymer blends so that the Flory interaction parameter is mainly influenced by free volume and interaction in polymer blends. [101] The exposure to high-pressure CO_2 enlarges the free volume disparity of both polymers and then χ increases. [102] In terms of the interaction, new CO_2-polymer non-covalent interactions replace the existing polymer-polymer interactions under exposure to high-pressure CO_2. [14] Since the original interaction between polymers is much more energetically favourable than the new interaction of CO_2 with polymers, χ_{PCL,co_2} and χ_{PLA,co_2} are larger than $\chi_{PCL,PLA}$ and thus χ increases. The increasing χ results in the occurrence of phase separation. [9,102]

Although both PCL and PLA are crystallizable polymers and high-pressure CO_2 can also promote polymer crystallization, [23] there is no clear spectroscopic evidence of crystallization at the conditions of this work, such as peak shift of the carbonyl stretching band in the spectra. Nevertheless, in chapter 6, another representative biopolymer blend: PHB/PLA blend will be chosen and its crystallization and phase separation will be investigated simultaneously. [9]

4.3.2 The investigation of effect of CO_2 pressure on the phase separation in PCL/PLA blends under high-pressure CO_2

The formal measurements were taken after the samples are in equilibrium to get rid of the effect of exposure time on their phase separation. It can be confirmed by the constant absorbance of bands in the spectra and the unchanged shape, size and location of blend component-rich domains in the spectroscopic images with increasing exposure time. As

shown in the images of figure 4.6(a) and spectra of figure 4.6 (b), phase separation occurs in the polymer blends under high-pressure CO_2 and its extent is enhanced gradually with increasing CO_2 pressure. It is because the CO_2 sorption into the polymer blend increases with increasing CO_2 pressure, which is indicated by the increasing absorbance of CO_2 band shown in figure 4.6(c). More CO_2 sorption leads to higher free volume, greater chain mobility and lower viscosity of both PCL and PLA. [9]

(a)

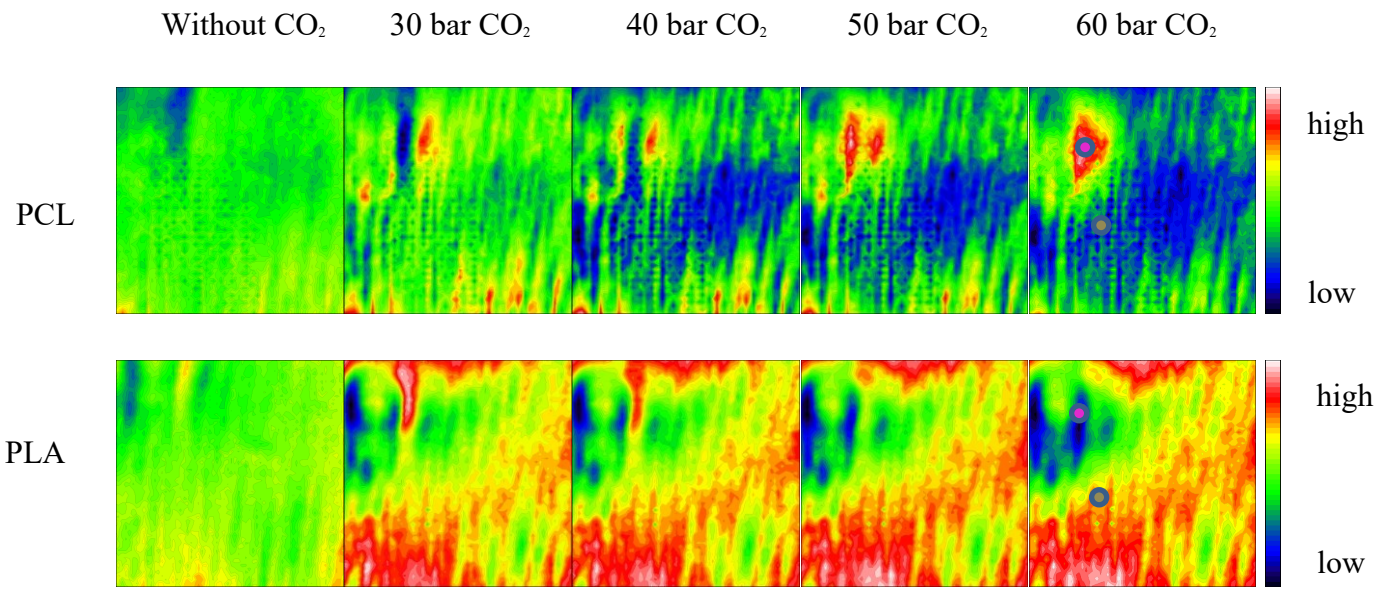

(b)

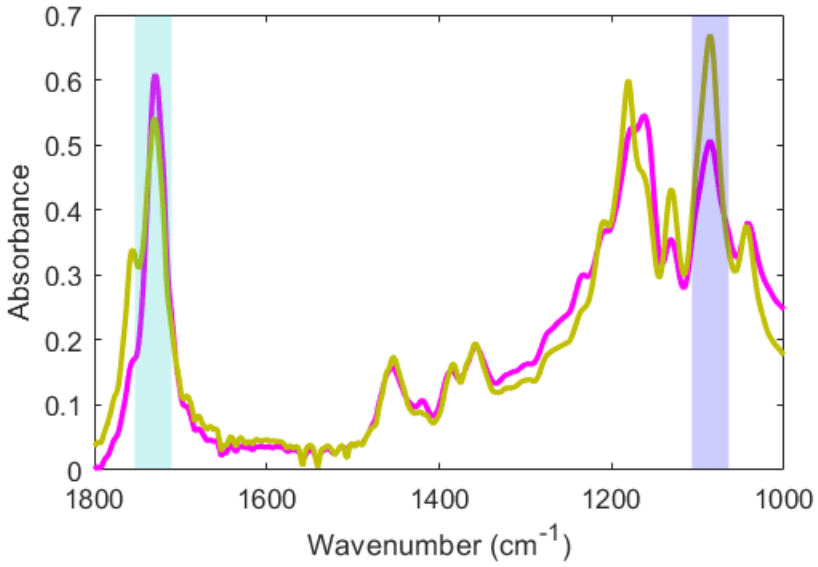

(c)

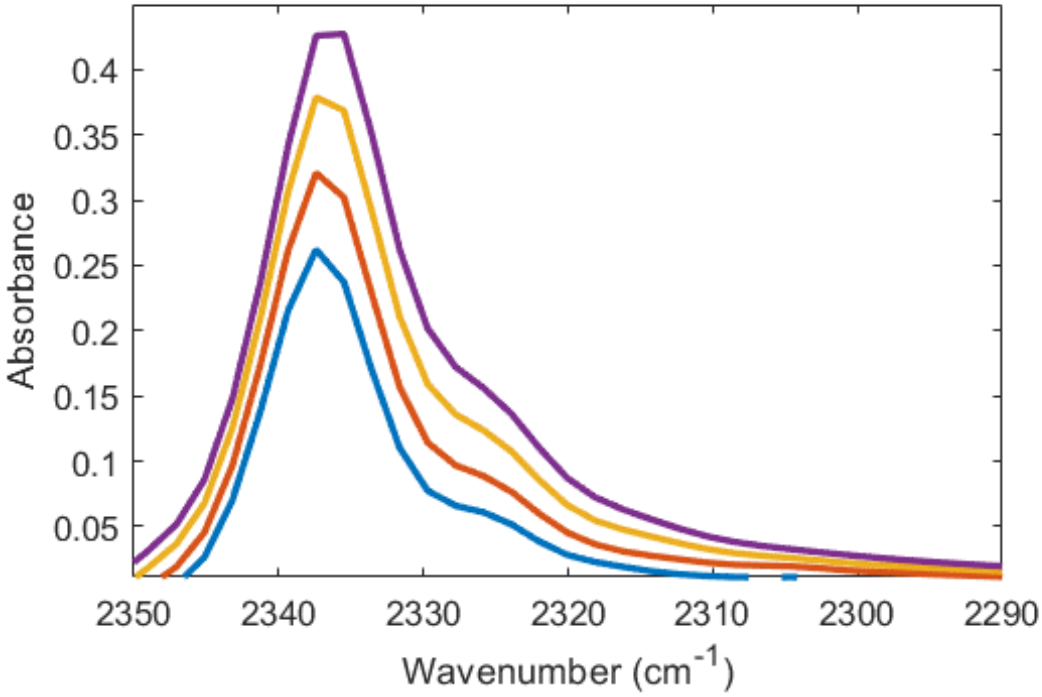

Figure 4.21 (a) ATR-FTIR spectroscopic images of the PCL (Mn=10000) and PLA blend at 30 °C in the absence of CO_2, with 30, 40, 50 and 60 bar CO_2. The top images are based on the spectral band of PCL while bottom images are based on that of PLA. (b): spectra were extracted from the PCL-rich domain indicated by a pink circle in the top right image and the PLA-rich domain indicated by a ginger circle in the bottom right image. (c): spectra were extracted from the whole imaged area at 30 °C under exposure to 30 (blue), 40 (brown), 50 (yellow) and 60 (purple) bar CO_2. (Source [9])

4.3.3 The investigation of effect of exposure time on the phase separation in PCL/PLA blends under high-pressure CO_2

As shown in figure 4.7, increasing exposure time can also enhance the extent of phase separation gradually in the PCL/PLA blend before reaching its equilibrium, which is indicated by the gradual separation and size change of PCL-rich domains and PLA-rich domains. This is because this blend needs some time to reach its equilibrium. However, the shape, size and location of blend component-rich domains in the images and absorbance of

bands in the spectra, measured after 60 min did not change. It indicates that increasing exposure time will no longer affect phase separation after the equilibrium reached. [9]

(a)

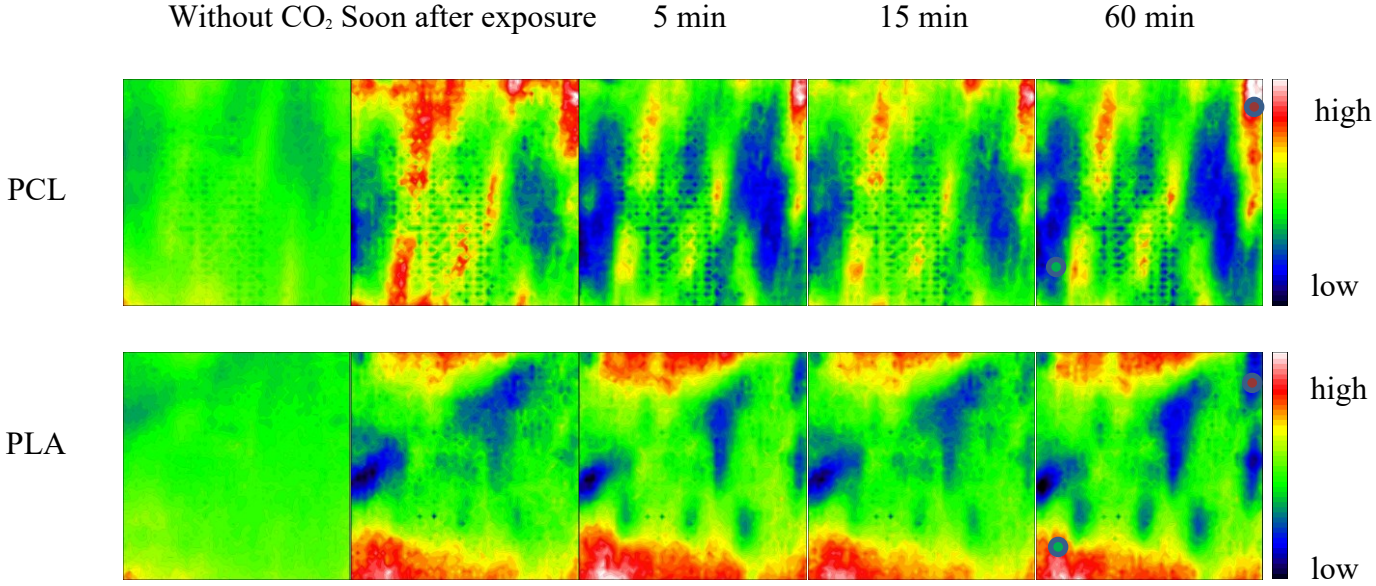

(b)

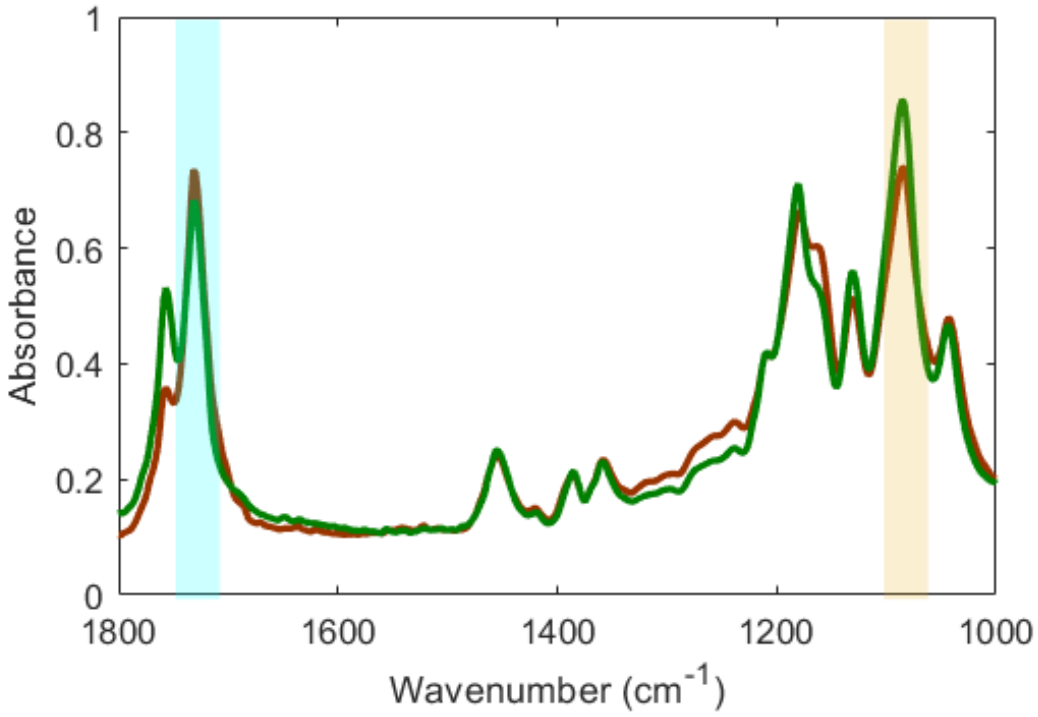

(c)

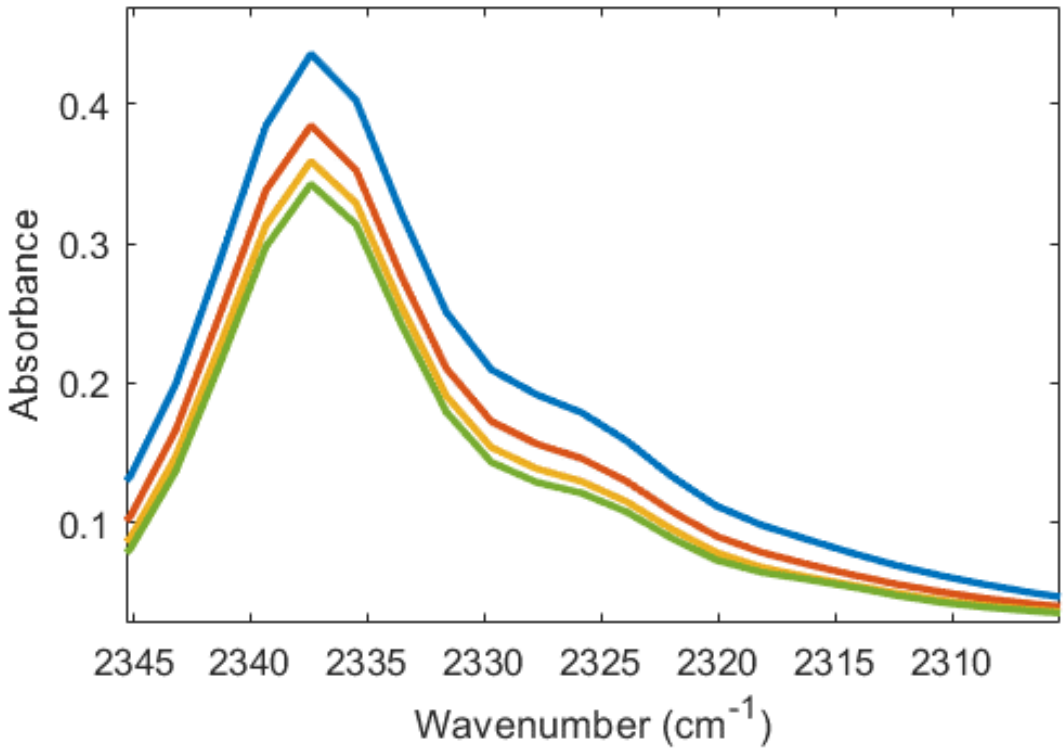

Figure 4.22 (a): ATR-FTIR spectroscopic images of the PCL (Mn=10000) and PLA blend at 45 °C in the absence of CO_2, soon after exposure to 60 bar CO_2, 5, 15 and 60 min. The top images are based on the spectral band of PCL while bottom images are based on that of PLA. (b): spectra were extracted from the PCL-rich domain indicated by a brown circle in the top right image and the PLA-rich domain indicated by a green circle in the bottom right image. (c): spectra were extracted from the imaged area soon after exposure to 60 bar CO_2 (blue), 5 (brown), 15 (yellow) and 60 (green) min. (Source [9])

4.3.4 The investigation of effect of heat on the phase separation in PCL/PLA blends under high-pressure CO_2

As mentioned in section 4.3.1, heat induces phase separation in PCL/PLA blends even without high-pressure CO_2. This is because increasing temperature leads to the increasing

chain and segmental mobility and then enhance the extent of phase separation. However, because the solubility of CO_2 in polymers decreases with increasing temperature, the CO_2 sorption in the polymer blend decreases with increasing temperature, which is indicated in the spectra (figure 4.8 (c)). The smaller concentration of CO_2 results in a higher T_g of polymer blend and thus has a negative effect on its phase separation. As a result, the effect of heat on phase separation in PCL/PLA blends under high-pressure CO_2 is difficult to predict. [9]

The formal measurement was also taken after the sample reaches its equilibrium. It can be found that phase separation in PCL/PLA blends under high-pressure CO_2 is enhanced gradually with increasing temperature as shown in figure 4.8. [9]

(a)

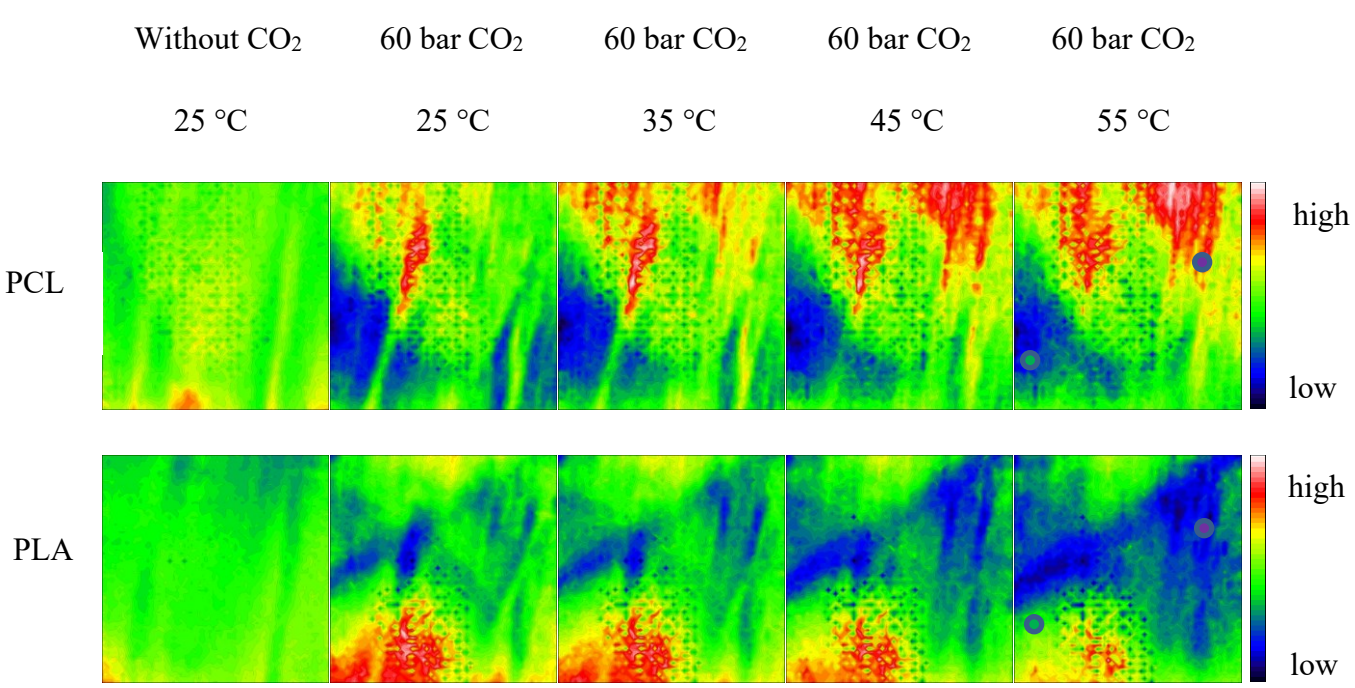

(b)

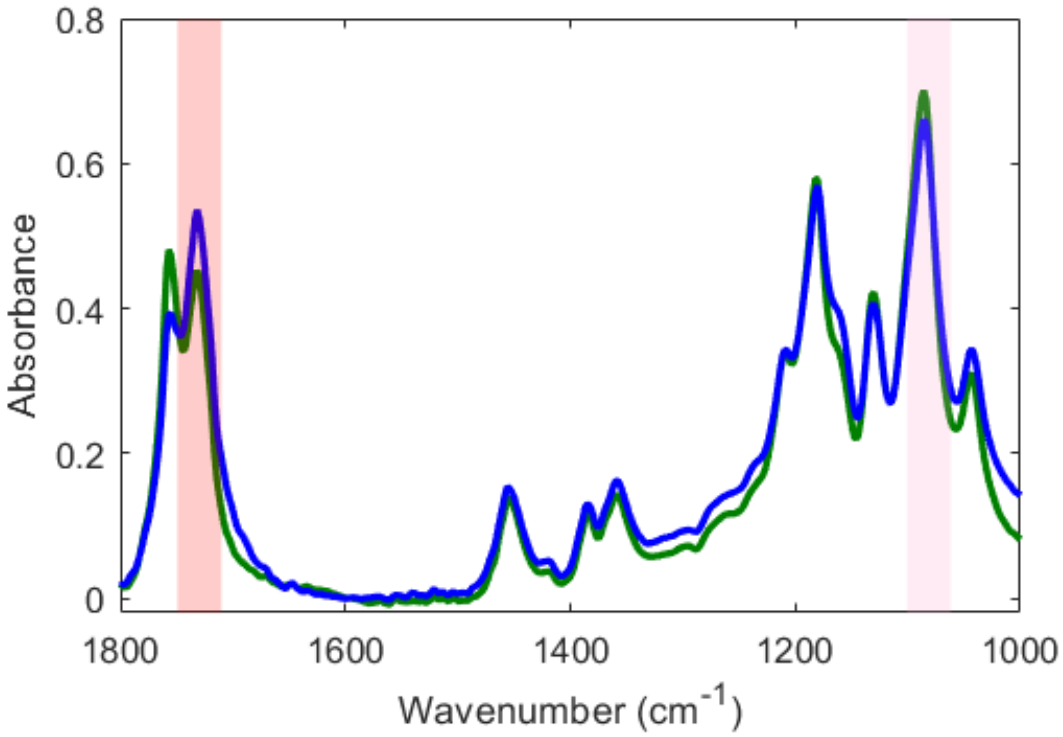
0.8
0.6
0.4
0.2
0
Absorbance
1800
1600
1400
1200
1000
Wavenumber (cm-1)

(c)

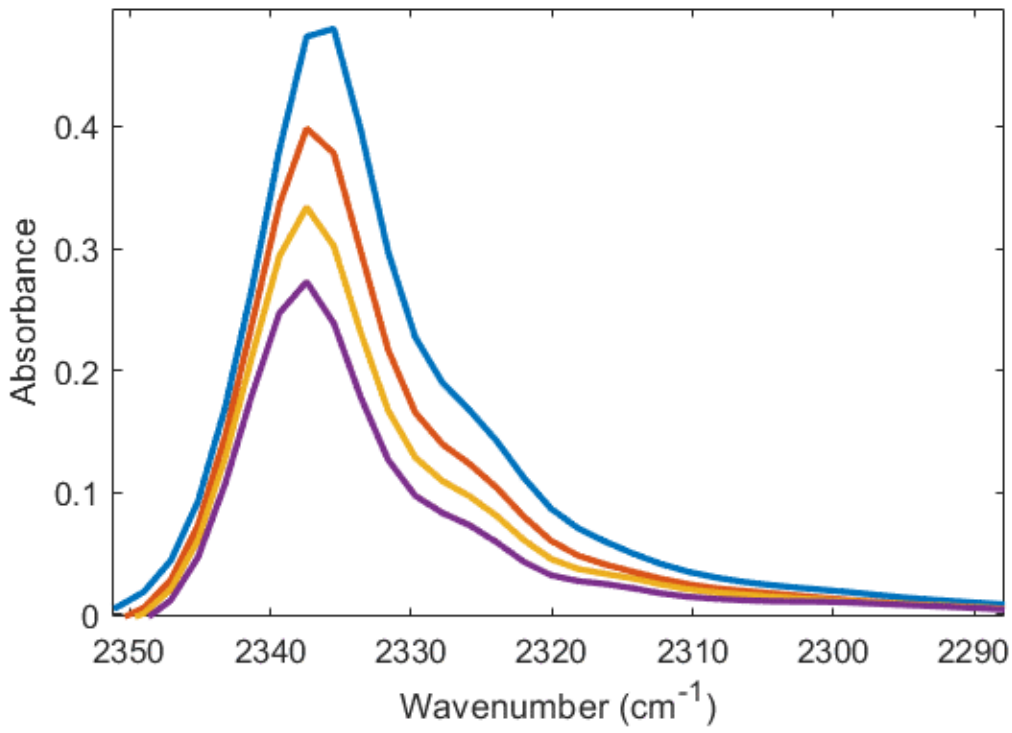
0.4
0.3
0.2
0.1
0
Absorbance
2350
2340
2330
2320
2310
2300
2290
Wavenumber (cm-1)

Figure 4.23 (a): ATR-FTIR spectroscopic images of the PCL (Mn=10000) and PLA blend in the absence of CO_2 at 25 °C, exposed to 60 bar CO_2 at 25 °C, 35 °C, 45 °C and 55 °C. The top images are based on the spectral band of PCL while bottom images are based on that of PLA. (b): spectra were extracted from the PCL-rich domain indicated by a blue circle in the top right image and the PLA-rich domain indicated by a green circle in the bottom right image. (c): spectra were extracted from the whole imaged area at 25 °C (blue), 35 °C (brown), 45 °C (yellow) and 55 °C (purple) under exposure to 60 bar CO_2. (Source [9])

PCL/PLA blends under 30 bar CO_2 and after depressurisation were measured and shown in figure 4.9 to explain this phenomenon. Because of the shrinkage of polymer blend after depressurisation, its density increases and the concentration of both PCL and PLA is greater. However, the shape, size and location of blend component-rich domains in the images are constant after depressurisation. It means that the phase separation of polymer blends is not reversible with reduced CO_2 pressure. As long as the polymer blend/CO_2 system is in equilibrium, only the increasing mobility of polymers caused by increasing temperature will affect the extent of phase separation. [9]

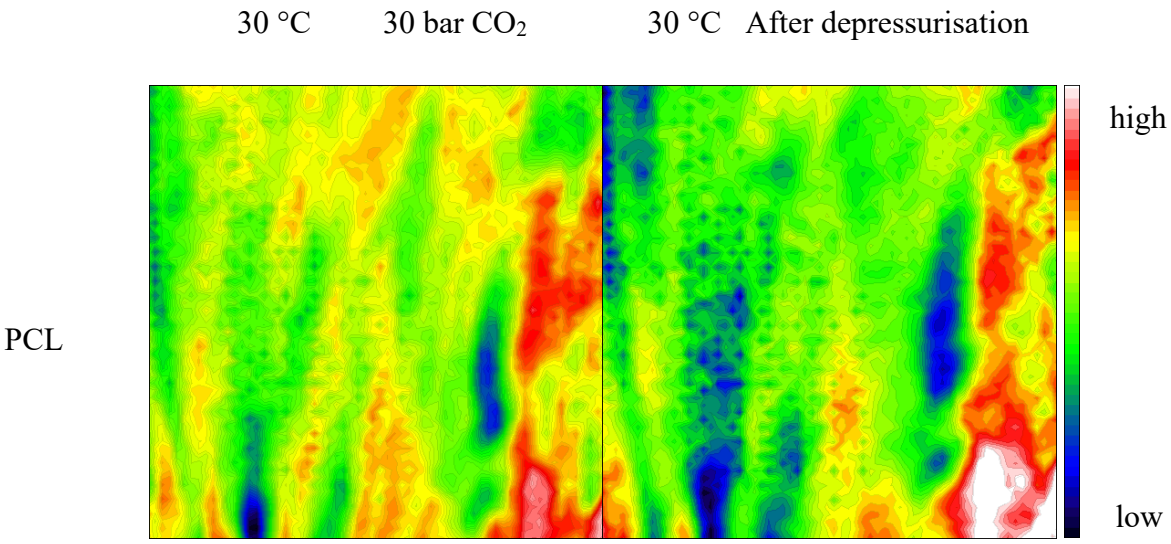

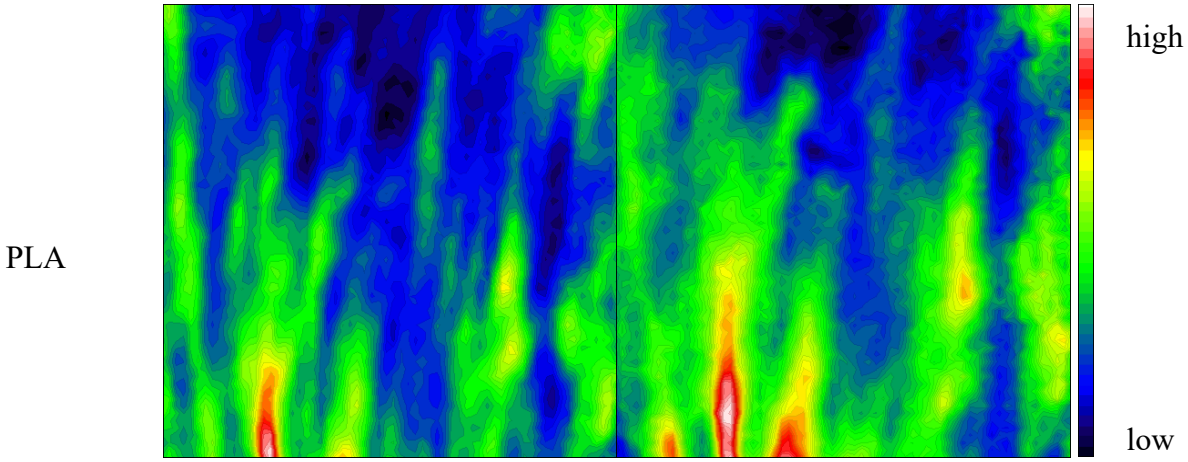

Figure 4.24 ATR-FTIR spectroscopic images of the PCL (Mn=10000)/PLA blend under exposure to 30 bar CO_2 and after depressurisation at 30 °C. The top images are based on the spectral band of PCL while bottom images are based on that of PLA. (Source [9])

4.3.5 The investigation of effect of polymer molecular weight on the phase separation in PCL/PLA blends under high-pressure CO_2

The effect of polymer molecular weight on phase separation was also assessed by changing the molecular weight of PCL from 10,000 to 93,000. It was found that high-pressure CO_2 can also induce phase separation in the new polymer blend and the effect of temperature, CO_2 pressure and exposure time on its extent of phase separation is the same. However, PLA/PCL (M_n=93,000 for PCL) blend film takes a shorter time to reach its equilibrium than PLA/PCL (M_n=10,000 for PCL) blend film under the same conditions (the same film thickness, the same CO_2 pressure and the same temperature). It can be explant by the higher LCST of PCL/PLA blends with a lower M_n of PCL, which indicates that PCL/PLA blends with a lower molecular weight PCL requires more heat to phase separate.[94] Because high-pressure CO_2 can mimic the effect of heat on the phase separation of LCST polymer blends, it is plausible to suggest that PCL/PLA blends with a lower molecular weight blend component need more heat, exposure time or CO_2 to further phase separate under high-pressure CO_2. [9]

4.3.6 The mechanism of phase separation in PCL/PLA blends under high-pressure CO_2

The average integrated absorbance of spectral band of PCL (1750 cm^{-1}-1700 cm^{-1}) in all of the pixels in the PCL-rich domains and the PCL-poor domains was calculated to obtain the average concentration of PCL in these areas. Likewise, the average PLA concentration in the PLA-rich domains and the PLA-poor domains can also be obtained via the band of PLA (1115 cm^{-1}-1058 cm^{-1}). As shown in figure 4.10, the concentration difference of blend component between blend component-rich domains and blend component-poor domains increases with increasing exposure time but keeps nearly constant with increasing CO_2 pressure or temperature. The same trend with the increasing CO_2 pressure and the increasing temperature is reasonable because high-pressure CO_2 can mimic the effect of heat. [9]

(a)

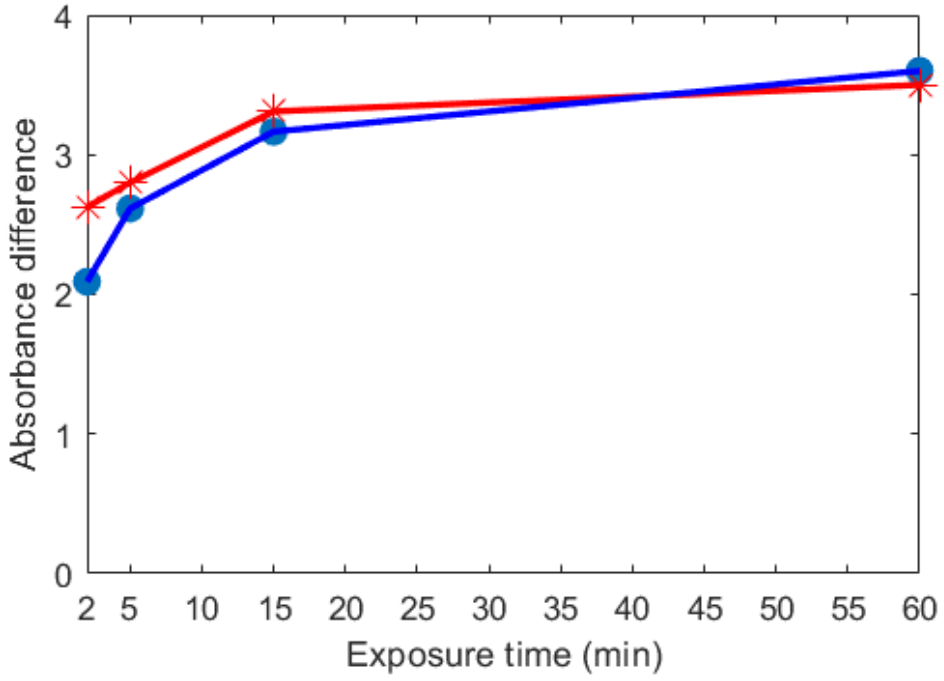

(b)

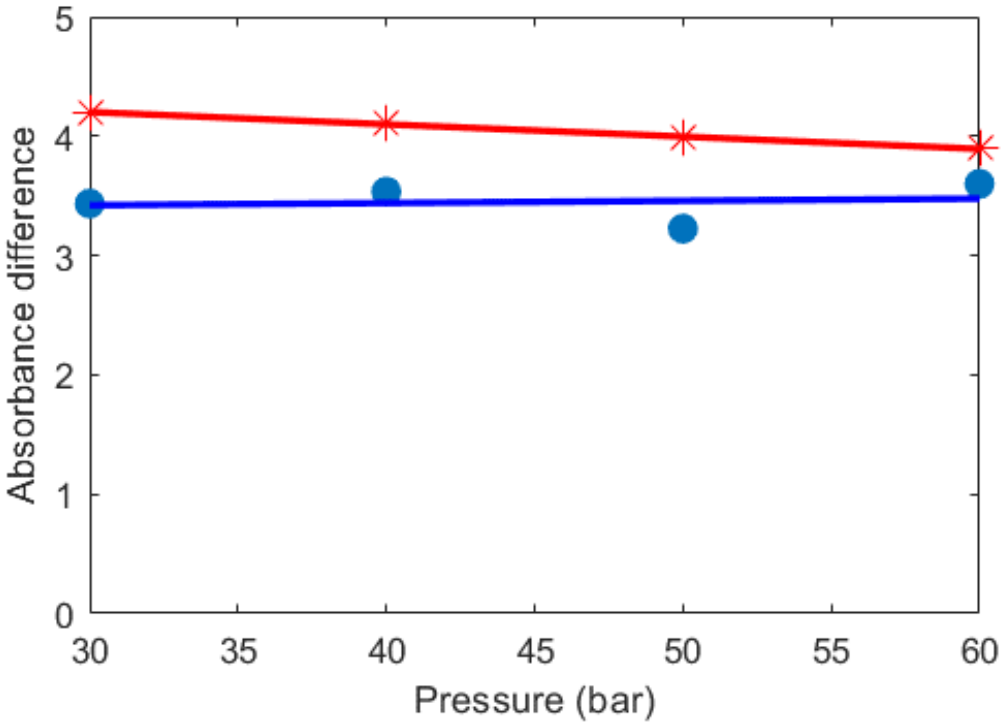
Absorbance difference
Pressure (bar)
0
1
2
3
4
5
30
35
40
45
50
55
60

(c)

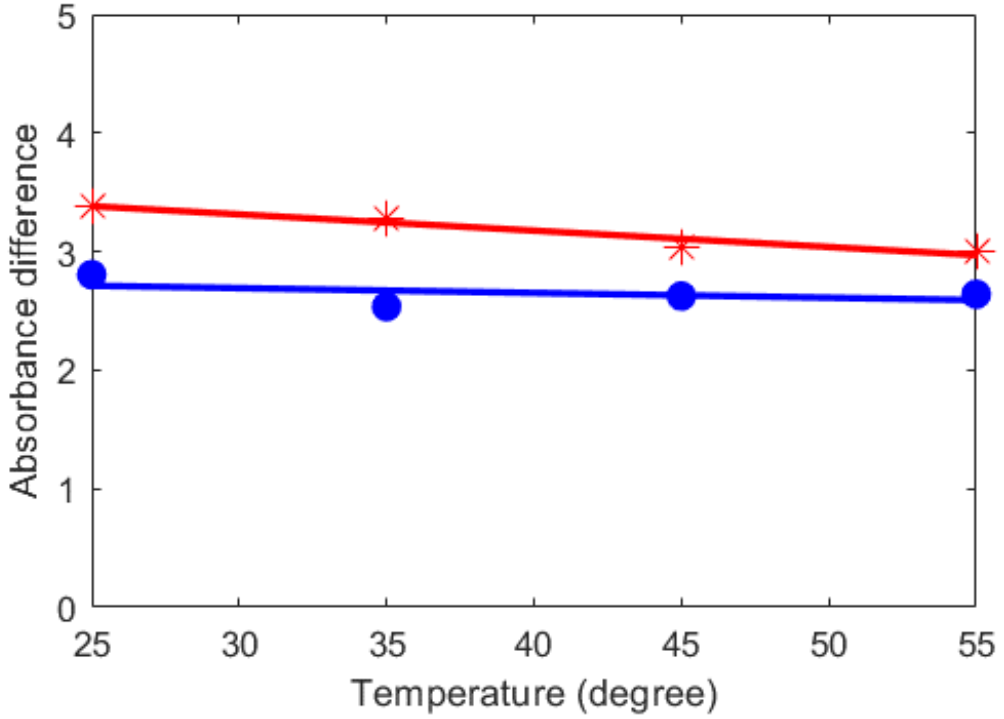
Absorbance difference
Temperature (degree)
0
1
2
3
4
5
25
30
35
40
45
50
55

Figure 4.25 Integrated absorbance difference of the spectral band of PCL between PCL-rich domains and PCL-poor domains (blue points and fitting curve) and integrated absorbance difference of the spectral band of PLA between PLA-rich domains and PLA-poor domains (red stars and fitting curve) with increasing exposure time (a), pressure (b) and temperature (c). (Source [9])

The mechanism of phase separation in LCST polymer blends under high-pressure CO_2 needs further investigation to explain the above phenomena. Because the concentration fluctuation increases with increasing exposure time before the equilibrium, the type of phase separation under high-pressure CO_2 at the early stage is spinodal decomposition process. This process occurs near the critical point in the phase diagram and it can be modelled by the Cahn-Hilliard equation. [9,103]

After the equilibrium reached, because increasing temperature or CO_2 pressure does not affect the concentration difference, the type of phase separation under high-pressure CO_2 at the late stage is nucleation and growth mechanism. It is because increasing CO_2 pressure leads to increasing Flory interaction parameter and thus decreasing critical point in the phase diagram. [8] As a result, both heat and increasing CO_2 pressure lead to the fact that the binodal becomes further above the critical point. [9,103]

4.4 Conclusion

In this chapter, in situ high-pressure ATR-FTIR spectroscopic imaging was applied to visualize the dynamic process of phase separation in biopolymer PCL/PLA blends under high-pressure CO_2, which is a good example of high-pressure CO_2-induced phase separation in LCST polymer blends. First of all, heat-induced phase separation in PCL/PLA blends was observed via in situ ATR-FTIR spectroscopic imaging, which indicates the feasibility of detecting phase separation through this technology. Because high-pressure CO_2 can simulate the effect of heat, this blend was exposed to high-pressure CO_2 and the occurrence of phase separation was visualized. Through varying different process variables (temperature, CO_2 pressure and exposure time), the changes in the extent of phase separation can be revealed by analysing the obtained ATR-FTIR spectroscopic images. The appearance and gradual

separation of PCL-rich domains and PLA-rich domains in the polymer blend shown in the spectroscopic images indicate the increasing extent of phase separation under different conditions. As a result, it can be demonstrated that the extent of phase separation in PCL/PLA blends under high-pressure CO_2 is enhanced with increasing exposure time, CO_2 pressure and temperature. It was also found that polymer blends with a larger molecular weight blend component are easier to phase separate under the same conditions, which is because the LCST of PCL/PLA blends increases with reducing M_w of one blend component. Finally, it was found that phase separation in this blend under high-pressure CO_2 is spinodal decomposition process before the equilibrium and nucleation & growth process after the equilibrium reached.[9]

With the help of this technology, the change of processing conditions, such as exposure time, temperature and pressure, can control the morphology of a specific LCST polymer blend system in situ and then influence the final processed products and materials. This study is the first step toward the realization of this potential. Another advantage of spectroscopic imaging is the ability to investigate the interactions occurring in the multicomponent polymer system, which will be explored in the next chapter. [9]

Chapter Five

Intra- and Intermolecular Interactions in the Polymer Blends under High-pressure CO_2 studied by Two-Dimensional Correlation Analysis and Two-Dimensional Disrelation Mapping

5. Inter- and Intramolecular Interactions in the Polymer Blends under High-pressure CO_2 studied by Two-Dimensional Correlation Analysis and Two-Dimensional Disrelation Mapping

As mentioned in the previous chapter, high-pressure and supercritical CO_2 may benefit the polymer processing. Thus, the mechanisms of polymer-polymer interaction with or without high-pressure CO_2 are worthy of further investigation. This chapter presents the application of two-dimensional (2D) correlation analysis and 2D disrelation mapping to datasets of PCL/PLA blend before and under exposure to high-pressure CO_2 obtained by in situ ATR-FTIR spectroscopic imaging. The specially designed polymer interface was prepared to distinguish the interactions between the same type of polymer molecules and different types of polymer molecules. [15]

This work demonstrates that the number of all three types of interactions: interaction between PCL molecules and PLA molecules, interaction between PCL molecules and interaction between PLA molecules in the polymer interface under exposure to high-pressure CO_2 decreases compared with that in the polymer interface before exposure to high-pressure CO_2 through comparing the disrelation intensity. The occurrence of phase separation in the PCL/PLA blend under high-pressure CO_2, which is visualized in chapter 4, can be explained by the increase in the Flory interaction parameter caused by weaker interactions between polymer molecules. The findings from this work are beneficial for polymer processing with high-pressure and supercritical CO_2. [15]

5.1 Motivation and scientific background

As mentioned in section 2.4, high-pressure and supercritical CO_2 is widely used in polymer processing as a viscosity modifier, plasticizing agent, reaction medium and foaming agent.

Thus, to fully realize the potential of polymer processing with it, the mechanisms of polymer-polymer interactions need more investigation.[80] To be more detailed, the interaction between additives and functional groups of polymers is hindered by the non-covalent bonds between polymer molecular chains. Then the access of these additives into the space between polymer molecules will be inhibited. As a consequence, weakening the polymer-polymer interactions, which promotes the penetration of polymer additives, can modify the polymer properties. However, the pharmaceutically important hydrogen bond interaction in some kinds of polymer blends is an exception. For instance, the hydrogen bond interaction in poly(ethylene glycol) (PEG) / polyvinylpyrrolidone (PVP) blends has a great influence on the elastic and adhesive properties, when these blends are used as transdermal delivery devices. [56] In summary, the investigation of inter- and intramolecular dipole-dipole interaction between polymers can predict and then improve the polymer properties. [15]

There are two species of polymers with C=O groups in the polymer sample under exposure to high-pressure CO_2: the free species and interacted species. The interacted species can also be divided into two species: the one interacted with CO_2 and the other one interacted with the C=O groups of other polymer molecules.[14,28] When PCL/PLA blends are exposed to high-pressure CO_2, the situation will become more complex because both polymers have carbonyl groups. The inter- and intramolecular dipole-dipole interactions (C=O···C=O) occur between a PCL molecule and a PLA molecule or between the same type of polymer molecules (PCL molecules or PLA molecules). Since all these three interactions lead to a different trend of absorbance change from the non-interacted C=O groups in the polymer and then result in cross-peaks in 2D correlation spectra, it is challenging to distinguish them through the conventional 2D correlation analysis. As a result, a specific PCL/PLA interface was designed in this study to distinguish these three types of inter- and intramolecular dipole-dipole interactions (C=O···C=O). [15]

In chapter 4, ATR-FTIR spectroscopic imaging was applied to visualize phase separation of PCL/PLA blends under high-pressure CO_2. It was found that the extent of phase separation is enhanced with increasing temperature, CO_2 pressure and exposure time.[9] Another study has investigated the mechanisms of possible interactions existing in polymers under high-pressure CO_2. It is assumed that high-pressure CO_2 breaks partly the polymer-polymer interactions but there is no strong spectroscopic evidence for this assumption.[14] Nevertheless, this work has highlighted that the prediction of polymer behaviour and the

improvement of polymer properties will both benefit from the understanding of polymer-polymer interactions. Thus, in this chapter, two steps were taken to demonstrate it: (1) investigating the polymer-polymer interactions before exposure to high-pressure CO_2. (2) investigating the polymer-polymer interactions under high-pressure CO_2. With the help of 2D correlation analysis and 2D disrelation mapping, ATR-FTIR spectroscopic imaging was applied in this chapter to investigate the interaction occurring in PCL/PLA interfaces before and under exposure to high-pressure CO_2. [15]

5.2 Experimental section

5.2.1 Materials

PCL, PLA and CO_2 used in this chapter are the same as those used in chapter 4. The chemical structures of PCL and PLA are shown in Figure 5.1. [15]

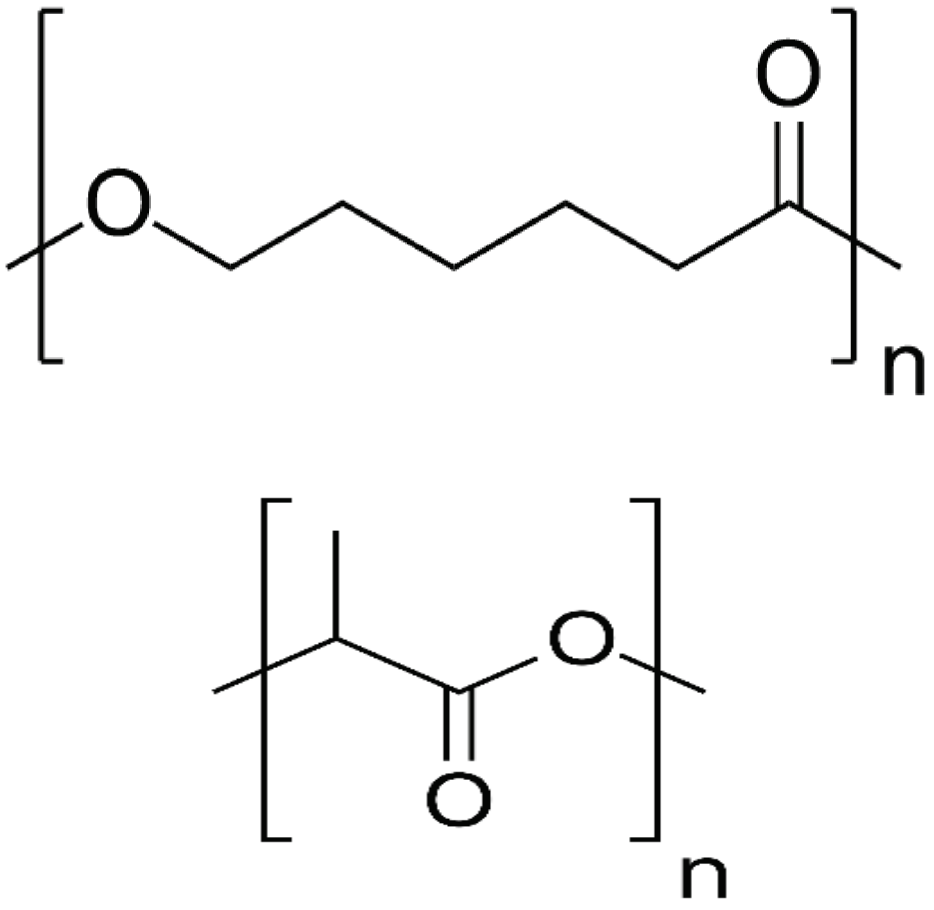

Figure 5.26 Chemical structures of PCL (top) and PLA (bottom). (Source [15])

5.2.2 Polymer interface preparation

The dried PLA was dissolved in chloroform (99.2% chloroform, 0.8% ethanol) to prepare the PLA solution and then the solution was cast onto the diamond to create a PLA film. After the film was fully dried, a scalpel was used to cut the formed film into two halves along the central line of diamond. Half of the film was disposed while the other half was covered by a glass slide. Then dried PCL was also dissolved in chloroform to obtain the PCL solution and then cast on the remaining half of the diamond. [79] The contact between PCL and PLA was ensured to be intimate and uniform because the PCL solution was liquid when it contacted the PLA half-film. It was also ensured that the size and thickness of both PCL half-film and PLA half-film were almost the same. Similar to chapter 4, the concentration of chloroform in the polymer sample was also monitored by the ATR-FTIR spectrometer to confirm that it had completely evaporated from the sample before taking measurements. [15]

5.2.3 In situ ATR-FTIR spectroscopic imaging measurements

An Alpha FTIR spectrometer (Bruker Corp.) was used to measure the conventional ATR-FTIR spectra of each component in PCL/PLA blends, separately. A Tensor 27 FTIR spectrometer (Bruker Corp.), as detailed in section 3.2, was applied to measure the ATR-FTIR spectroscopic images with an FPA detector. A spectral resolution of 4 cm^{-1} and 64 co-added scans were applied. [15]

5.2.4 High-pressure experimental apparatus

The high-pressure set-up is detailed in section 3.3. [15]

5.2.5 2D correlation analysis and 2D disrelation map

2D correlation analysis was used to process with sets of spatially resolved spectra obtained from varied spectral positions. [15]

Through assuming a spectral data matrix **A** made up of *m* rows of spectra and *n* columns of spectral variables, a set of dynamic spectra $\widetilde{\mathbf{A}}$ are defined through subtracting an average spectrum. Then the synchronous correlation spectrum **Φ** can be obtained as

$$\mathbf{\Phi} = \frac{1}{m-1}\widetilde{\mathbf{A}}^T\widetilde{\mathbf{A}} \qquad (5\text{-}1)$$

The absolute value of disrelation spectrum $\mathbf{\Lambda}_{ij}$ can be obtained by

$$\left|\mathbf{\Lambda}_{ij}\right| = \sqrt{\mathbf{\phi}_{ii}\mathbf{\phi}_{jj} - \mathbf{\Phi}_{ij}^2} \qquad (5\text{-}2)$$

where $\mathbf{\phi}_{ij}$ means the *i*th row and *j*th column element of the synchronous correlation matrix defined by Eq. (5-1). [15]

The intensity of a synchronous 2D correlation spectrum $\mathbf{\phi}_{ij}$ corresponds to the similarity in changes of the spectral intensities at the *i*th and *j*th spectral variables (e.g. wavenumber) observed within a measured area. While the intensity of a disrelation spectrum $\mathbf{\Lambda}_{ij}$ represents the dissimilarity of changes of the spectral intensities at the *i*th and *j*th spectral variables appearing in the spatial region. [46,104] When employing 2D correlation analysis to spectroscopic imaging data, the disrelation intensity is more important. For instance, a substantial level of disrelation intensity will appear when physically or chemically meaningful changes occur. Thus, one can further utilize this feature of disrelation intensity to construct disrelation maps in order to identify the pertinent spectral variations within a spectroscopic image. In the protocol of disrelation mapping, disrelation analysis is applied to a small select local window within the full spectral image. Then the window is incremented stepwise so as to cover the whole spectral image. Disrelation intensity only becomes significant in the regions where physically or chemically meaningful variations take place. This technology is suitable to pinpoint the region of interest within a vast spectral dataset. [15]

5.3 Results and discussion

5.3.1 The evidence of inter- and intramolecular dipole-dipole interactions (C=O···C=O) between polymer molecules before exposure to high-pressure CO_2

The research focus is the interfacial area between PCL bulk area and PLA bulk area. It is because the inter- and intramolecular dipole-dipole interactions (C=O···C=O) between PCL molecules and PLA molecules only occur in this area. Meanwhile, the inter- and intramolecular dipole-dipole interactions between PCL molecules only occur in PCL bulk area while those between PLA molecules only occur in PLA bulk area. As a result, because of the special structure of PCL/PLA interface, these three types of interactions are well distinguished in it. Moreover, PLA with a higher M_w was chosen in this work to enhance the intermolecular dipole-dipole interactions between PCL and PLA in the interfacial area. This is because the smaller PCL molecules are much easier to enter the free volume of larger PLA molecules. It will result in the increasing possibility for the interaction between PCL and PLA. On the other hand, PLA, which has a higher proportion of C=O groups, is more likely to interact with PCL when contacting PCL. [15]

5.3.1.1 ATR-FTIR spectroscopic imaging

According to the research in chapter 4, the spectral band at 1721 cm^{-1} and the spectral band at 1083 cm^{-1}, which correspond to PCL and PLA, were used to construct ATR-FTIR spectroscopic images of their distribution. [9] As shown in figure 5.2, PCL and PLA are well separated in the interface and the interfacial area is clearly represented by green pixels and blue pixels. It was observed that the shape of interfacial area in the centre-right image is like a hook. The interfacial region is the narrowest at the right side of ‘hook’ and the second narrowest at its left side. This indicates that the PCL bulk area and the PLA bulk area are closest in these two regions of the image. [15]

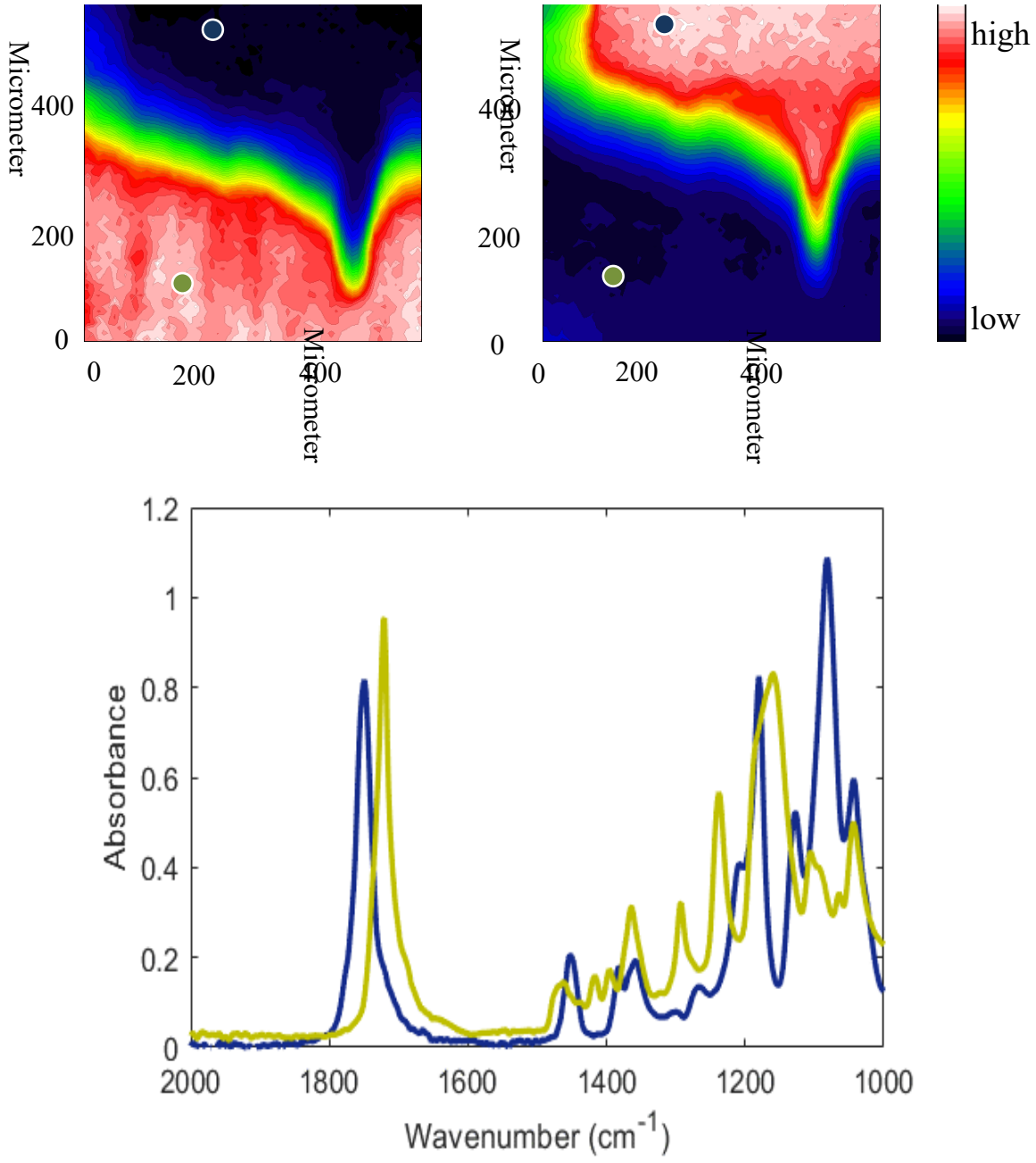

Figure 5.27 Top: ATR-FTIR spectroscopic images of the PCL/PLA interface in the absence of CO_2 at 30 °C. The images are based on the spectral band of PCL (1733 cm^{-1}-1708 cm^{-1}) (left) and PLA (1115 cm^{-1}-1058 cm^{-1}) (right). Bottom: spectra were extracted from the PCL bulk area indicated by a brown circle and the PLA bulk area indicated by a blue circle in the top images, respectively. (Source [15]**)**

5.3.1.2 Synchronous spectra and disrelation spectra

Figure 5.3 (top) and figure 5.3 (bottom) show the synchronous and disrelation spectra which were derived from the ATR-FTIR spectra of the interface at 30 °C, respectively. As shown in figure 5.3 (top), one can observe several auto peaks including (1721 cm^{-1}, 1721 cm^{-1}) and (1753 cm^{-1}, 1753 cm^{-1}), which indicates that the change in the concentration of both PCL and PLA is great within the spatial region. It is because of the phase separation in the PCL/PLA interface. The negative synchronous cross peaks including (1721 cm^{-1}, 1753 cm^{-1}) indicate that the concentration of one polymer increases while that of the other one reduces as a function of spatial position, which is another evidence of the occurrence of phase separation in the interface. [15]

As shown in figure 5.3 (bottom), several cross peaks, which represents dissimilar changes of the pattern of spectral absorbance, were observed in the disrelation spectra. The cross-peaks (1753 cm^{-1}, 1721 cm^{-1}) correspond to the C=O group of PLA and PCL, which are caused by phase separation of the PCL/PLA interface. The auto peaks (1721 cm^{-1}, 1721 cm^{-1}) and (1753 cm^{-1}, 1753 cm^{-1}) in the synchronous spectra are split into cross peaks (1713 cm^{-1}, 1730 cm^{-1}) and (1737 cm^{-1}, 1751 cm^{-1}) in the disrelation spectra. It implies that the spectral absorbance for C=O groups of PCL at 1730 cm^{-1} and 1713 cm^{-1} change in different manners. Meanwhile, the spectral absorbance for C=O groups of PLA at 1737 cm^{-1} and 1751 cm^{-1} also change in different manners. The appearance of theses disrelation correlation peaks indicates the specific states of both PCL and PLA molecules in the interface. It suggests that the absorbance changes observed at 1713 and 1737 cm^{-1} are ν(C=O) modes of PCL and PLA, which represent the unusual molecular environment of the components. Positional shifts of the carbonyl bands can be explained by the existence of an inter- and intramolecular dipole-dipole interaction (C=O···C=O) between the polymers. This is because the strength of molecular-level interactions has a great effect on the band position of FTIR spectrum. [46] The appearance of inter- and intramolecular dipole-dipole interaction (C=O···C=O) can then be demonstrated by a band position shift to a lower wavenumber. As a result, it suggests that the lower wavenumber bands at 1713 and 1737 cm^{-1} are likely to correspond to the interacted C=O groups of PCL and PLA, respectively. They are the best current model to explain these two bands though these assignments are not so definitive. [15]

Figure 5.3 also shows a cross peak (1751, 1760 cm^{-1}) which means that the origin of band at 1760 cm^{-1} is not as same as that at 1751 cm^{-1} (interfacial interaction band). Although the current research community cannot explain the origin of this band, at least it can be concluded that the band at 1760 cm^{-1} is not associated with the interfacial interaction band at 1751 cm^{-1} and the normal amorphous band at 1737 cm^{-1} of PLA. As a result, it suggests that the subtle disrelation peak at 1760 cm^{-1} represents the presence of little crystalline component, which is difficult to identify by the examination of original FTIR spectra. Thus, this discovery proves the power of 2D correlation technology to identify the subtle but important change in the spectral feature. [15]

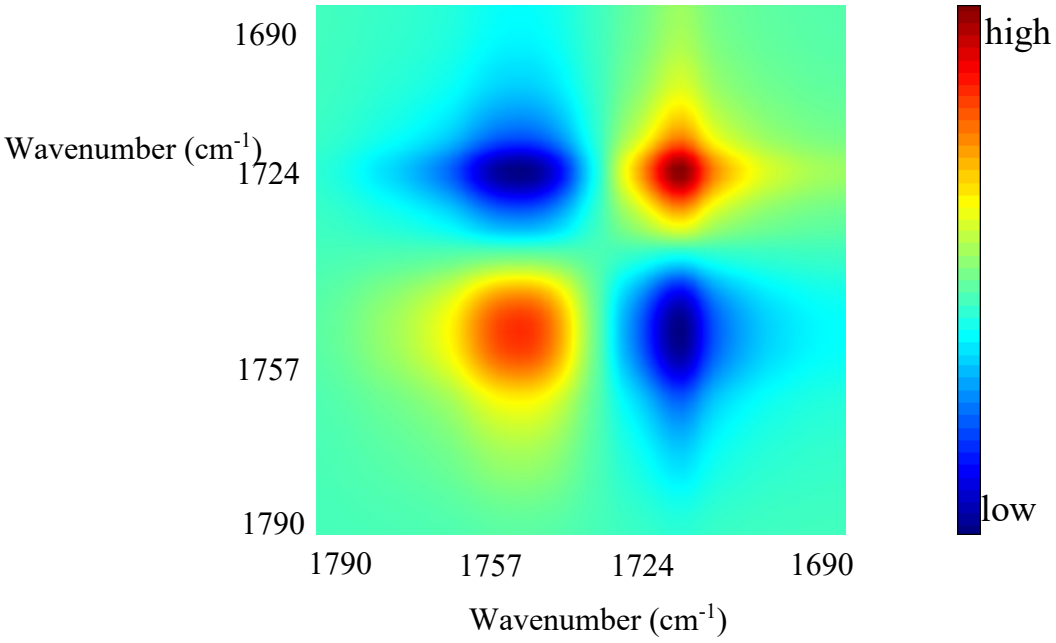

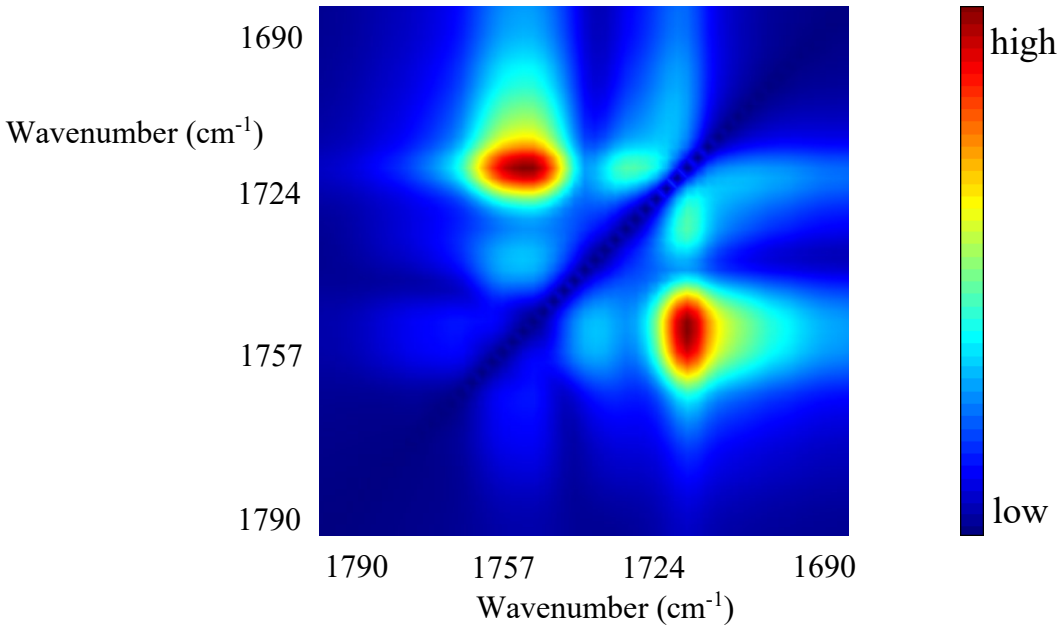

Figure 5.28 Synchronous (top) and disrelation (bottom) spectra derived from ATR-FTIR spectra of the PCL/PLA interface at 30 °C. (Source [15]**)**

Thus far, it is concluded that the interaction between C=O groups occurs. However, it is not clear whether it is the inter- and intramolecular dipole-dipole interaction (C=O···C=O) between the same type of polymer molecules or the intermolecular dipole-dipole interaction (C=O···C=O) between different type of polymer molecules (PCL and PLA). As a consequence, the disrelation map would be applied for further investigation. [15]

5.3.1.3 Disrelation Map

As shown in figure 5.2, When PCL and PLA contact, they diffuse into each other and coexist in the interfacial area. As mentioned above, because of the special design of the polymer interface, both of these two polymers are more likely to interact with each other in the interfacial area. In addition, the concentration of PCL reduces gradually from the bottom to the top part of the imaged area while that of PLA reduces gradually from the top to the bottom part of the imaged area. The narrower the interfacial area, the higher the concentration of PCL and PLA are on its both sides. Thus, it is supposed that the intermolecular dipole-dipole interactions (C=O···C=O) between PLA molecules and PCL molecules are more likely to occur in the narrower interfacial area. [15]

The convolution filter, which is a spatial filter based on the 2D correlation function, was applied to highlight the areas where disrelated variation between ν_1 and ν_2 occurs. [46] Thus, this filter can highlight the interactions between polymer molecules in this work. In order to enhance the contribution from all correlation intensity, the smallest size of the convolution window: 3×3 was chosen. [15]

As shown in figure 5.4, the disrelation map derived from the spectral absorbance of the bands at 1737 cm^{-1} and 1751 cm^{-1} was prepared to visualize the different trends of the change in the spectral absorbance of interacted C=O groups and non-interacted C=O groups of PLA. It was found that the appearance of strong disrelation intensity (bright blue) is mainly in the same area as the interfacial region and PLA bulk area in the ATR-FTIR images (figure 5.2), which can be explained by the fact that there is an additional contribution accelerating or delaying the absorbance change of the band of the C=O groups in PLA. To be more specific, the absorbance variation in the band of the interacted C=O group of PLA does not follow the trend of that of the non-interacted C=O group of PLA. It implies that the interaction between PLA molecules appears in the interfacial region and PLA bulk area. [15]

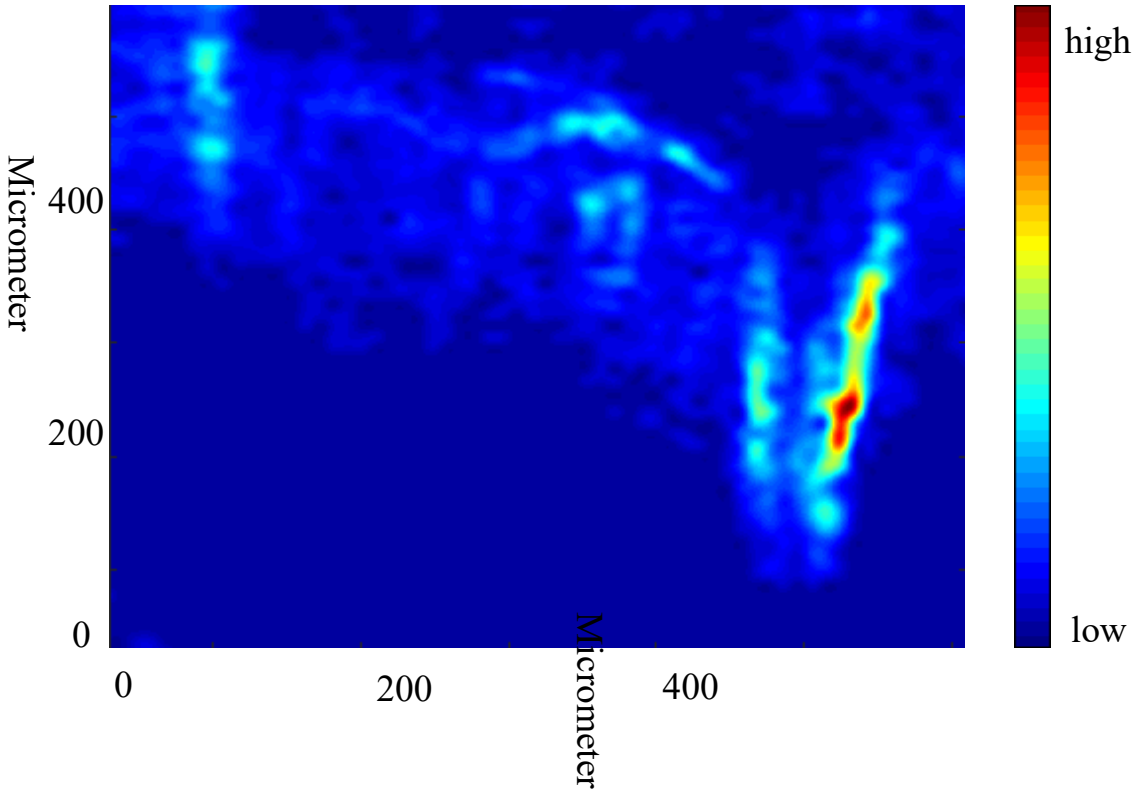

Figure 5.29 Disrelation map of the PCL/PLA interface obtained by calculating disrelation intensity between 1751 cm^{-1} and 1737 cm^{-1}, corresponding to the non-interacting C=O groups and interacting C=O groups of PLA, respectively. (Source [15]**)**

If there is only interaction between the same type of polymer molecules existing, the disrelation intensity in the interfacial area will not be as strong as that in the PLA bulk area. This is because the concentration of PLA in the PLA bulk area is higher than that in the interfacial area. However, it was found that the disrelation intensity in the PLA bulk area is much weaker than that in the interfacial area. It indicates that an additional contribution exists to accelerate or delay the absorbance change of band of the C=O groups of PLA and it only appears when PLA contacts PCL. Moreover, the disrelation intensity becomes stronger with reducing width of the interfacial area and peaks at the right side of the 'hook', which is the narrowest interfacial area. This indicates that the additional contribution becomes stronger with increasing concentration of contacting PCL and PLA. Thus, it can also be proved that the interaction between PCL and PLA exists. [15]

As shown in figure 5.5, a disrelation map derived from the spectral absorbance of the bands at 1713 cm^{-1} and 1730 cm^{-1} was prepared to visualize the different trends of the absorbance change in the bands of interacted C=O groups and non-interacted C=O groups of PCL. Likewise, disrelation intensity appears in the PCL bulk area, which indicates the occurrence of the interaction between PCL molecules. But the strength of this type of interaction is much weaker than that of the interaction between PLA molecules. This is because the dipole-dipole interactions (C=O•••C=O) are fewer in PCL compared with the same weight PLA. The proportion of C=O groups in PCL is lower than that in PLA. [15]

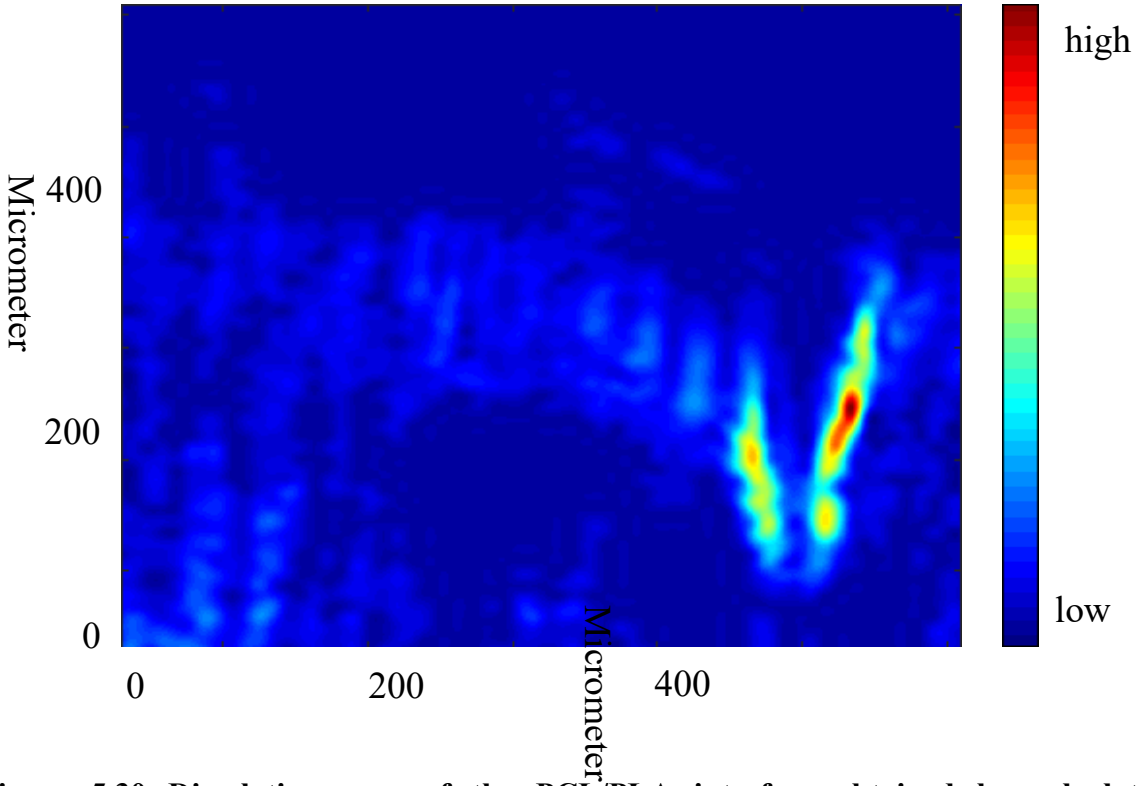

Figure 5.30 Disrelation map of the PCL/PLA interface obtained by calculating disrelation intensity between 1730 cm^{-1} and 1713 cm^{-1}, corresponding to the non-interacting C=O groups and interacting C=O groups of PCL, respectively. (Source [15]**)**

Disrelation intensity also appears in the interfacial area, which suggests that the interaction between C=O groups in PCL and C=O groups in PLA exists. Likewise, the disrelation intensity becomes stronger with narrower interfacial area and peaks at the right side of 'hook' (the narrowest interfacial area). It suggests that the additional contribution, which accelerates or delays the absorbance variation of the band of C=O groups of PCL, becomes stronger with rising concentration of contacting PCL and PLA. This discovery also demonstrates the occurrence of the interaction between PCL and PLA. [15]

To summarise, the interaction between PCL molecules is proved by the appearance of disrelation intensity in the PCL bulk area, while the interaction between PLA molecules is proved by the appearance of disrelation intensity in the PLA bulk area. The interaction between the PCL molecule and PLA molecule is proved by the strong disrelation intensity in the interfacial area of PCL and PLA. In fact, the evidence of such development of inter- and intramolecular dipole-dipole interactions (C=O•••C=O) was also provided by a previous study based on ATR-FTIR spectroscopy. [15,28]

5.3.2 The evidence of inter- and intramolecular dipole-dipole interactions (C=O···C=O) between polymer molecules under exposure to high-pressure CO_2

5.3.2.1 ATR-FTIR spectroscopic images

As shown in figure 5.6, there is still phase separation in the PCL/PLA interface under exposure to high-pressure CO_2 but the interfacial area becomes closer to the bottom part of imaged area. It can be found from the spectra (figure 6(c)) that the CO_2 sorption in PLA is higher than that in PCL, which is because PLA with a higher proportion of C=O groups for the Lewis acid-base interaction has a greater affinity for CO_2. Because the CO_2 sorption leads to polymer swelling, the greater CO_2 sorption, the greater extent of polymer swelling. Then the greater extent of PLA swelling results in the displacement of the interfacial region. Moreover, a new PCL/PLA interfacial area appears in the bottom right part of imaged area. According to the previous study, even 60 bar CO_2 cannot induce crystallization of both blend components in PCL/PLA blends. [9] Moreover, the peak of C=O stretching band will shift if crystallization is induced. [16] No strong spectroscopic evidence of crystallization, such as peak shift, appears in the spectra shown in figure 5.2 (bottom) and figure 5.6 (bottom). Thus, it can be concluded that there is no crystallization occurring at the interface under exposure to high-pressure CO_2. More importantly, it is assumed that the studied inter- and intramolecular interactions occur between polymer molecules in the amorphous region. This is because the polymer molecules in the crystalline domains have already been involved in interactions within corresponding crystalline domains. [15]

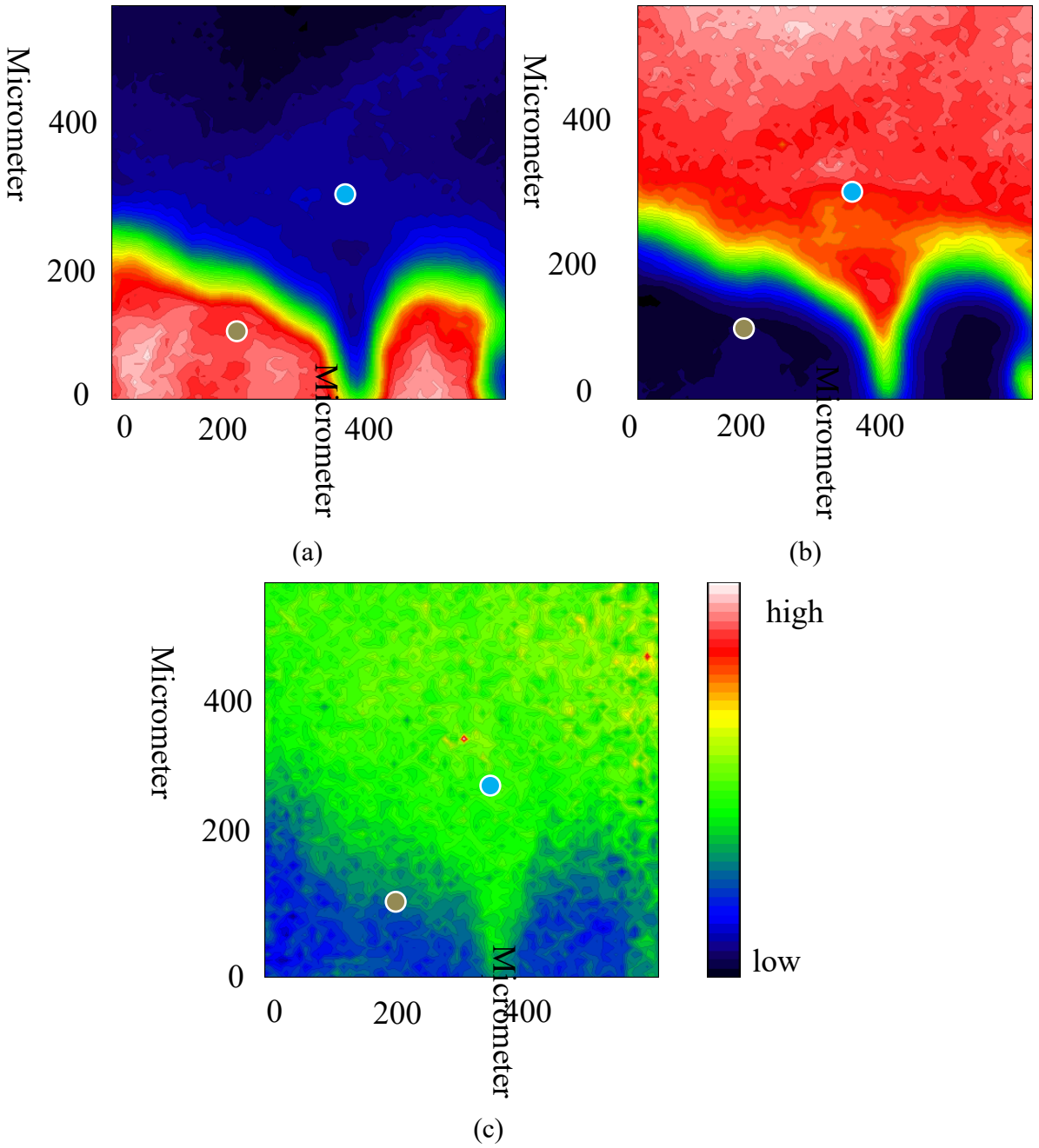
Micrometer
400
200
0
0
200
400
Micrometer
(a)
Micrometer
400
200
0
0
200
400
Micrometer
(b)
Micrometer
400
200
0
0
200
400
Micrometer
high
low
(c)

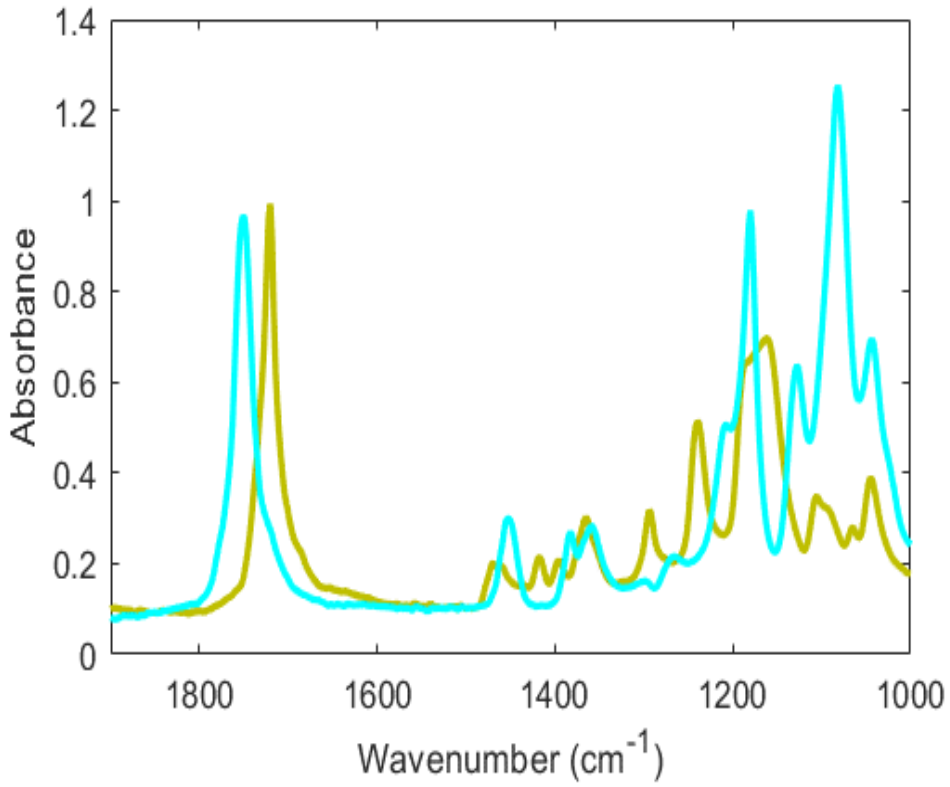

Figure 5.31 Top: ATR-FTIR spectroscopic images of the PCL/PLA interface with 30 bar CO_2 at 30 °C. The images are based on the spectral band of PCL (1733 cm^{-1}-1708 cm^{-1}) (a), PLA (1115 cm^{-1}-1058 cm^{-1}) (b) and CO_2 (2355 cm^{-1}-2315 cm^{-1}) (c). Bottom: spectra were extracted from the PCL bulk area indicated by a brown circle and the PLA bulk area indicated by a blue circle in the images, respectively. (Source [15]**)**

5.3.2.2 Disrelation Map

As shown in figure 5.7 (top), the disrelation map derived from the spectral absorbance of the bands at 1730 cm^{-1} and 1713 cm^{-1} (non-interacted C=O groups and interacted C=O groups of PCL) was prepared. Likewise, as shown in figure 5.7 (bottom), the disrelation map derived from the spectral absorbance of the bands at 1751 cm^{-1} and 1737 cm^{-1} (non-interacted C=O groups and interacted C=O groups of PLA). It can be observed that the disrelation intensity in both PCL bulk area and PLA bulk area is weaker under high-pressure CO_2, which is because high-pressure CO_2 breaks some of the interaction of PCL molecules and some of the interaction of PLA molecules. Meanwhile, it can be observed that the high disrelation intensity (bright blue) is in the same area as the interfacial region in the spectroscopic images

(figure 5.6). The disrelation intensity becomes stronger with narrower interfacial region and peaks at the right side of 'hook' (the narrowest interfacial region), which means that the interaction of PCL molecules and PLA molecules still exists. But the strength of the disrelation intensity is much weaker under high-pressure CO_2, which suggests that high-pressure CO_2 breaks some of the inter- and intramolecular dipole-dipole interactions (C=O···C=O) between PCL molecules and PLA molecules. It can also be observed that the disrelation intensity is abnormally strong in the bottom right part of the disrelation map, which is caused by the fact that this new interfacial region was just formed under high-pressure CO_2 so that high-pressure CO_2 don't have enough time to penetrate the newly formed interfacial region than the previous interfacial region. [15]

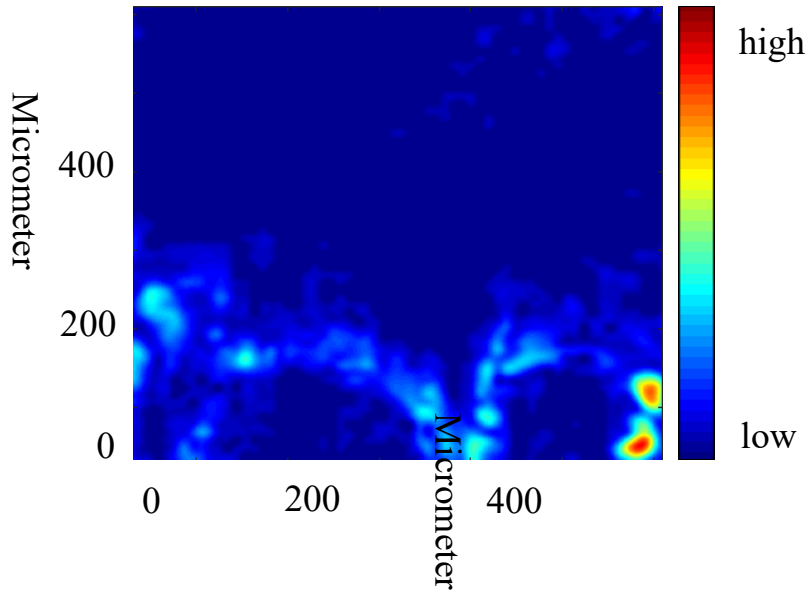

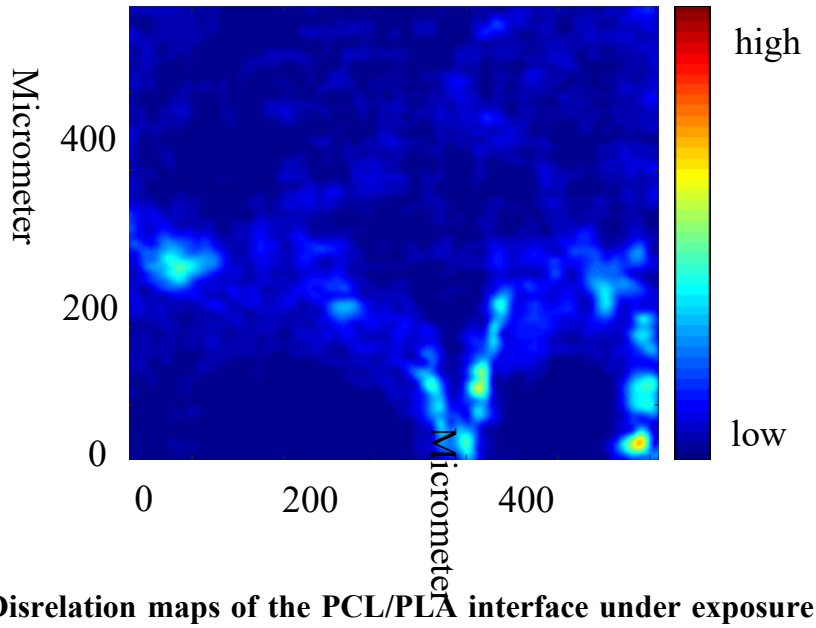

Figure 5.32 Disrelation maps of the PCL/PLA interface under exposure to 30 bar CO_2 obtained by calculating disrelation intensity between 1730 cm^{-1} and 1713 cm^{-1}(top) (corresponding to the non-interacted C=O groups and interacted C=O groups of PCL, respectively.) as well as disrelation intensity between 1751 cm^{-1} and 1737 cm^{-1}(bottom). (corresponding to the non-interacted C=O groups and interacted C=O groups of PLA, respectively.) (Source [15])

5.3.3 The effect of △χ on phase separation of polymer blend under high-pressure CO_2

The previous research based on ATR-FTIR spectroscopy provided plenty of evidence of the development of C=O···CO_2 complex structures. [28,60,105] Lewis acid-base interaction between CO_2 and these two polymers will occur after CO_2 penetrates the PCL/PLA blend. The results obtained in this chapter can help explain the occurrence of phase separation in PCL/PLA blends under exposure to high-pressure CO_2 visualized in Chapter 4.[9] From a thermodynamic view, the free enthalpy G (Gibbs free energy) obtained by equation 4-2 should be positive when phase separation occurs. [15]

Figure 5.4, 5.5 and 5.7 demonstrate the CO_2-weakened specific inter- and intramolecular interaction between the polymer molecules while the previous research demonstrates the appearance of Lewis acid-base interaction between C=O groups and CO_2. [28,60,105] Due to

the fact that the sum of χ_{PCL,co_2} and χ_{PLA,co_2} is larger than $\chi_{PCL,PLA}$, χ increases and the phase boundary in the phase diagram shifts to lower temperatures. [8,9,15]

5.4 Conclusion

In this chapter, the mechanisms of polymer-polymer interactions were investigated using 2D correlation analysis and 2D disrelation mapping. A special PCL/PLA interface was designed in this work to distinguish the intermolecular dipole-dipole interaction (C=O···C=O) between PLA molecule and PCL molecule from that intra- and intermolecular interactions between the same type of polymer molecules. The occurrence of polymer-polymer interactions is proved by the synchronous and disrelation spectra derived from the ATR-FTIR spectra of the PCL/PLA interface. The obtained disrelation map shows the spatial distribution of all these three interactions: the interaction between PLA molecules mainly in the PLA bulk area, the interaction between PCL molecules mainly in the PCL bulk area, and the interaction between PCL molecule and PLA molecule in the interfacial area. Thus, it demonstrates that all of these three types of interactions occur in the PCL/PLA interface. Then the disrelation map suggests that the number of all these three types of polymer-polymer interactions decreases under high-pressure CO_2. Consequently, the 2D correlation analysis provides evidence of the break of some of the existing inter- and intramolecular dipole-dipole interaction (C=O···C=O) between polymer molecules, which inhibits the access of polymer additives to modify polymer properties. The high-pressure CO_2-weakened polymer-polymer interactions and the occurrence of Lewis acid-base interactions between C=O groups and CO_2 result in an increase of the Flory interaction parameter and then make the phase boundary in the phase diagram shift to lower temperatures. This result can help explain the occurrence of phase separation in this blend under exposure to high-pressure CO_2 visualized in chapter 4. [15]

This work proves the power of combining FTIR imaging with 2D correlation analysis and 2D disrelation map to identify different types of molecular interactions. This method is not limited to the polymer interface with C=O groups but has great potential to investigate other homopolymers or multicomponent polymer systems with different functional groups. This work is the first step toward the realization of this potential. [15]

Chapter Six

Simultaneous visualization of phase separation and crystallization in PHB/PLA blends with in situ ATR-FTIR spectroscopic imaging

6. Simultaneous visualization of phase separation and crystallization in PHB/PLA blends with in situ ATR-FTIR spectroscopic imaging

This chapter presents the application of in situ ATR-FTIR spectroscopic imaging to detect the phase separation and crystallization in PHB/PLA blends simultaneously. PHB/PLA blends are representative upper critical solution temperature (UCST) polymer blends, which indicates that they are miscible beyond the critical temperature for all compositions. This work visualized the dynamic process of crystallization and phase separation in this blend simultaneously in order to benefit the biopolymer processing. [16]

The first part of this chapter describes the isothermal crystallization process of homopolymers: PHB and PLA measured by ATR-FTIR spectroscopic imaging. The second section of this chapter focuses entirely on the isothermal crystallization process of PHB/PLA blends and the comparison of the extent of phase separation in this blend under different isothermal crystallization temperatures. It is found that crystallization slows down with increasing isothermal crystallization temperature and then leaves more time for phase separation. Finally, a mechanism of the isothermal crystallization process of the polymer blend was proposed. [16]

6.1 Motivation and scientific background

PHB, which can be obtained by bacterial fermentation, is an optically active aliphatic polyester. It has a quite low T_g, nearly 5 ˚C. This polymer is widely used in many fields, such as regenerative medicine and tissue engineering, because it is biodegradable and biocompatible. [106–108] However, its high degree of crystallization results in brittleness. Preparation of PHB copolymers and blending with other polymers are two common methods to improve its mechanical properties. Between them, polymer blending technique is more simple and PLA is one of the most suitable polymers to blend with PHB. [5,92] Compared with PHB, there is one less -CH_2- group in the chain backbone of repeating units in PLA. The

monomer of PLA, lactide, can be produced from natural resources and the final products of degradation (water and CO_2) are also non-toxic, so it is also one of the most popular biocompatible and biodegradable polymers. [75,109,110] More importantly, the stiffness and tensile strength of PLA is great and it cannot crystallize even under relatively high cooling conditions. [16,89,95,111]

The PHB/PLA (Figure 6.1) blend is an UCST polymer blend but its phase separation does not occur below the crystallization temperature of its blend components because they are both semi-crystalline polymers. On the other hand, the miscibility of PHB/PLA blends affects the crystallization behaviour of PHB and PLA. As a result, several methods, such as FTIR spectroscopy, polarized light microscopy and differential scanning calorimetry (DSC), have been applied to characterize the crystallization behaviour of both miscible and immiscible PHB/PLA blends. [66,68,84] Besides PHB/PLA blends, other UCST polymer blends, such as PCL/ polystyrene (PS) blend [112] and poly(ethylene-co-hexene) (PEH)/poly(ethylene-co-butene) (PEB) blend, [113] have also been investigated. It was demonstrated that the crystallization kinetics[113] and the final structure[112] of polymer blends are dependent on the competition between phase separation and crystallization, which results in the possibility of morphology control of the final products. [16,93]

In the previous studies, simultaneous crystallization of PHB and PLA in the miscible blends and their stepwise crystallization in the immiscible blends were investigated using dynamic analysis of FTIR spectroscopy.[84] However, the melt-crystallization process can only be studied in either immiscible state or miscible state due to the technical constraint. In this work, the dynamic process of crystallization and phase separation in the PHB/PLA blend was studied simultaneously using in-situ ATR-FTIR spectroscopic imaging. To the best of our knowledge, the imaging approach has never been used to simultaneous visualize the crystallization and phase separation of the polymer blend. [16]

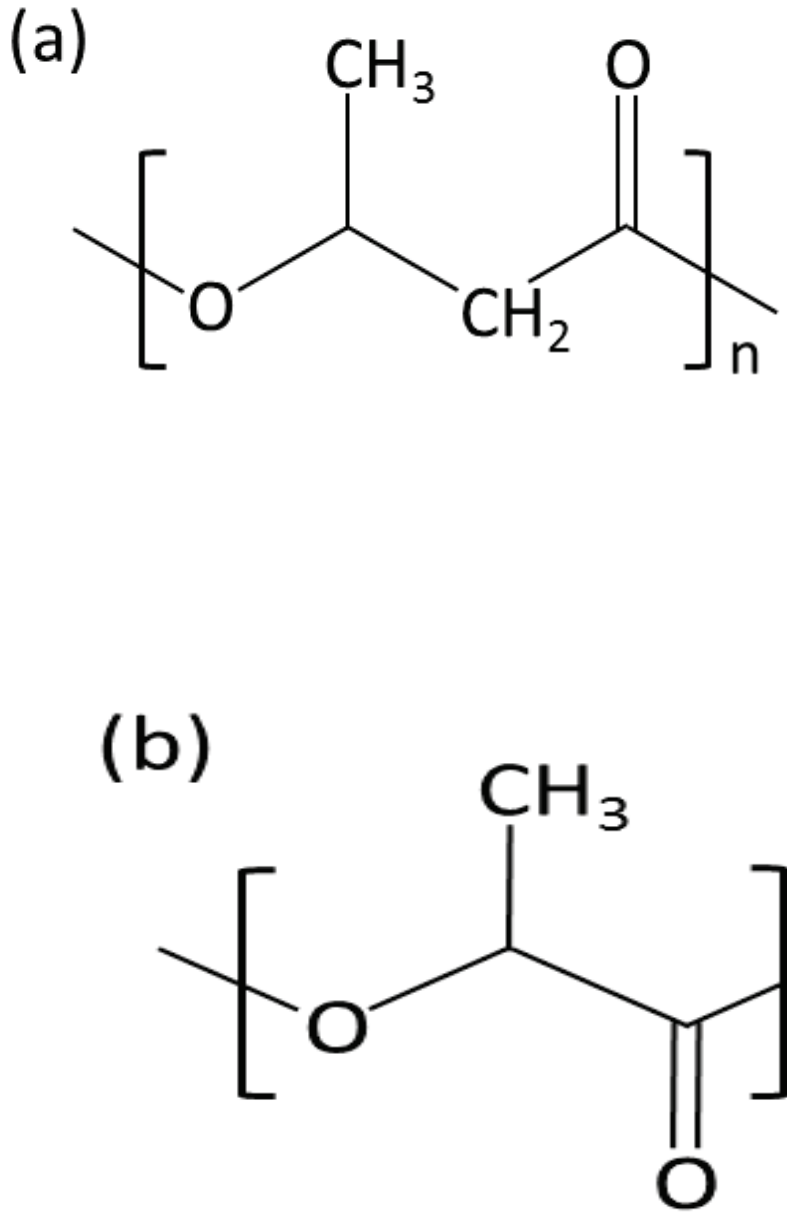

Figure 6.33 Chemical structure of (a) PHB and (b) PLA. (Source [16]**)**

6.2 Experimental section

6.2.1 Materials

PHB (M_w=5,000) was bought from Polysciences. Inc. PLA (M_w=50,000) was purchased from BMG Inc., Japan. The T_m of PHB and PLA are 163 ˚C and 182 ˚C, respectively. [16]

6.2.2 The preparation of PHB/PLA blends

The process of polymer blend preparation is the same as that described in section 4.2.2 except PHB took the place of PCL. [16]

6.2.3 In situ ATR-FTIR spectroscopic imaging

An Equinox 55 FTIR spectrometer (Bruker Corp.) with a MCT detector was used to measure the conventional ATR-FTIR spectra of pure PHB and PLA, separately. A Tensor 27 FTIR spectrometer (Bruker Corp.), as detailed in section 3.2, was applied to measure the ATR-FTIR spectroscopic images with a FPA detector. A spectral resolution of 4 cm^{-1} and 64 co-added scans were applied. The obtained images reveal the changes in spatial distribution and concentration of each component.[16,114]

6.2.4 Isothermal crystallization process of pure polymers and polymer blends

The polymer blend sample was heated to 185 ˚C through using a heater and left for 5 mins in order to remove the crystallites and erase thermal history. Then the samples were cooled down by ambient air to the requested isothermal crystallization temperatures. The cooling rates 14.5 ˚C/min, 14.3 ˚C/min, 14 ˚C/min, 13.6 ˚C/min, 13.25 ˚C/min, 13 ˚C/min and 12.5 ˚C/min are corresponding to the isothermal crystallization temperatures: 160 ˚C, 155 ˚C, 150 ˚C, 145 ˚C, 140 ˚C, 135 ˚C and 130 ˚C, separately. The smaller temperature difference between diamond crystal in the ATR accessory and ambient air, the slower cooling rate will become. The measurement took place in a 10 min interval and lasted for 6 hours. [16]

6.3 Results and Discussion

6.3.1 The investigation of isothermal crystallization process of homopolymers: PHB and PLA

ATR-FTIR spectra in the C=O stretching vibration region of pure PHB and PLA at different temperatures are shown in figure 6.2. Because the band at 1731 cm^{-1} and the band at 1748 cm^{-1} are the only bands of C=O group in the molten states of these polymers, they are assigned to the amorphous states of PHB and PLA, respectively. The band at 1720 cm^{-1} is due to the crystalline PHB because its absorbance increases while the absorbance of band corresponding to the ν (C=O) mode of amorphous PHB decreases during PHB crystallization. Likewise, the band at 1756 cm^{-1} is due to the crystalline PLA because its absorbance increases while the absorbance of band corresponding to the ν (C=O) mode of amorphous PLA decreases during PLA crystallization. Thus, the integration ranges used to generate spectroscopic images were selected as follows: 1730-1700 cm^{-1} for crystalline PHB and 1762-1753 cm^{-1} for crystalline PLA. Since these four bands corresponding to the ν (C=O) mode of amorphous PHB, amorphous PLA, crystalline PHB and crystalline PLA are well identified, it is feasible to use them to trace the isothermal crystallization process of these two polymers in situ. [16]

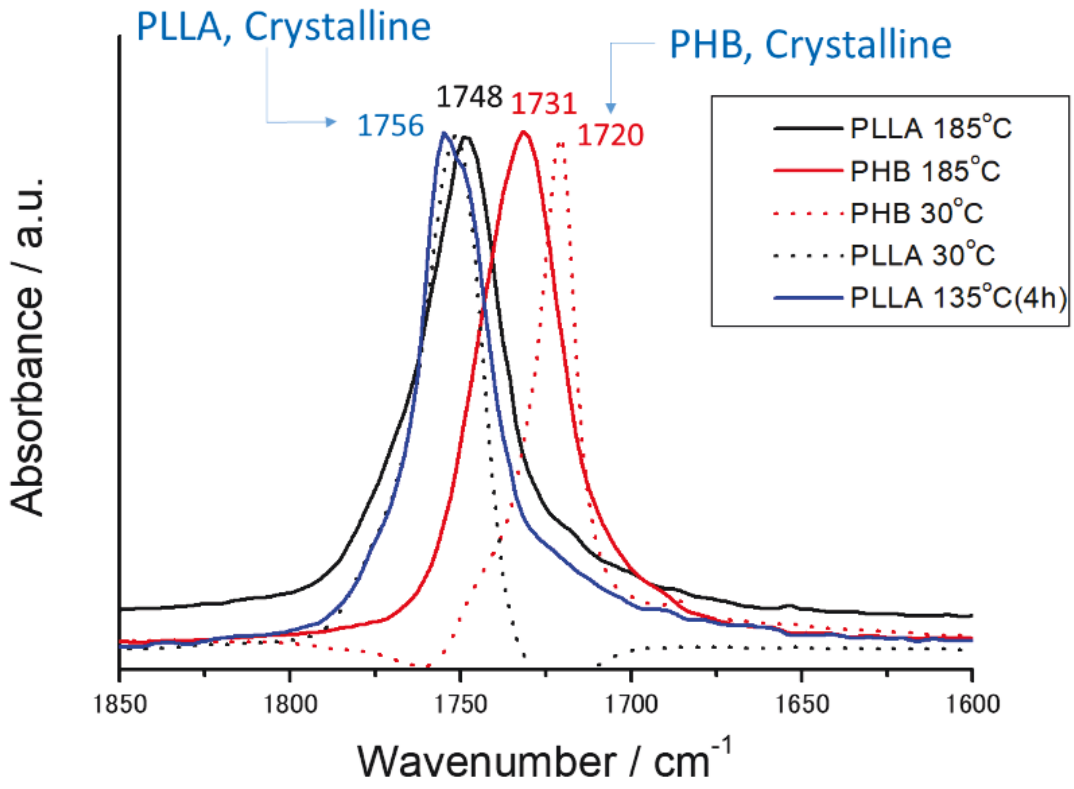

Figure 6.34 ATR-FTIR spectra in the C=O stretching vibration region of pure PHB and PLA at the molten state (185 ˚C), isothermal crystallization temperature (135 ˚C) and 30 ˚C. (Source [16]**)**

Firstly, ATR-FTIR spectroscopic imaging was used to measure the isothermal crystallization process of pure PHB and PLA at 160 ˚C, 155 ˚C and 150 ˚C, separately. The colour red represents a high degree of crystallization while the colour blue represents a low degree of crystallization. Figure 3 (top) shows that PHB did not crystallize even after 6 hours when the isothermal crystallization temperature (160 ˚C) was close to its T_m (163 ˚C). However, it partially crystallizes at 155 ˚C and crystallizes at 150 ˚C or below. As a result, it was demonstrated that the upper critical crystallization temperature (T_c) for PHB (M_w=5,000) is between 155 ˚C and 160 ˚C. On the other hand, as shown in figure 3 (middle), PLA crystallizes in the whole isothermal crystallization temperature range because even the highest isothermal crystallization temperature 160 ˚C is far from T_m (182 ˚C) of PLA. Thus, it can be demonstrated that T_c of PLA (M_w=50,000) is above 160 ˚C. [16]

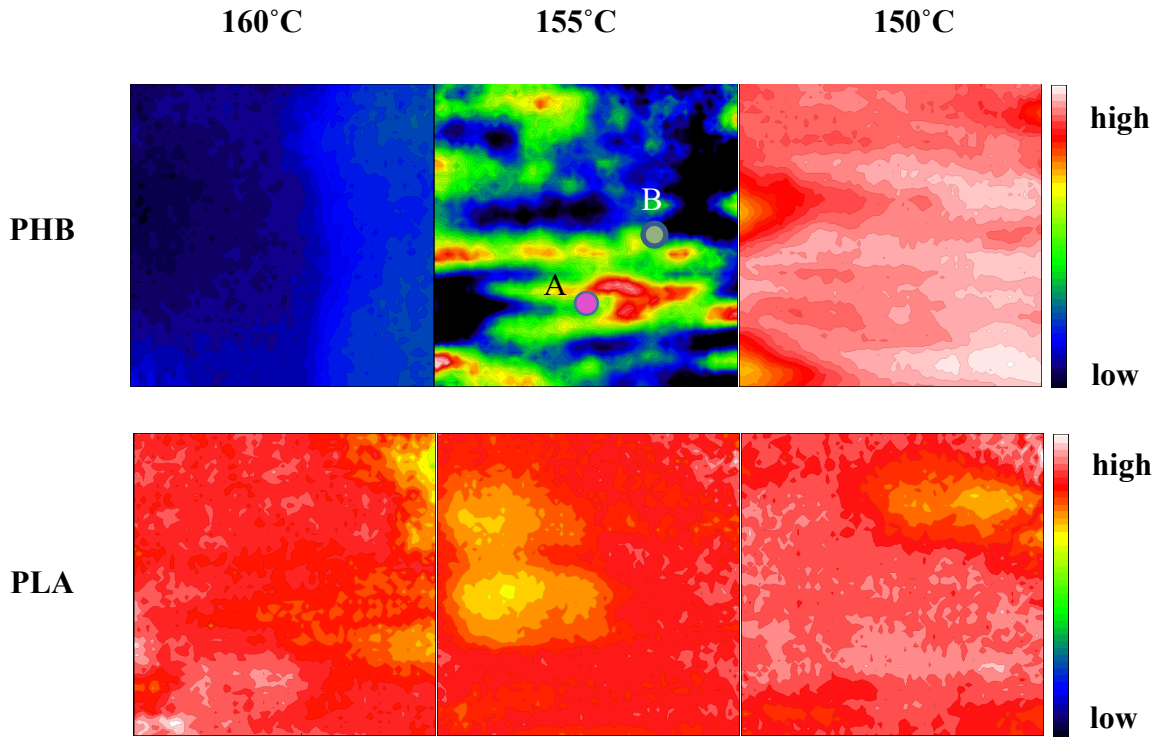
160˚C
155˚C
150˚C
PHB
A
B
high
low
PLA
high
low

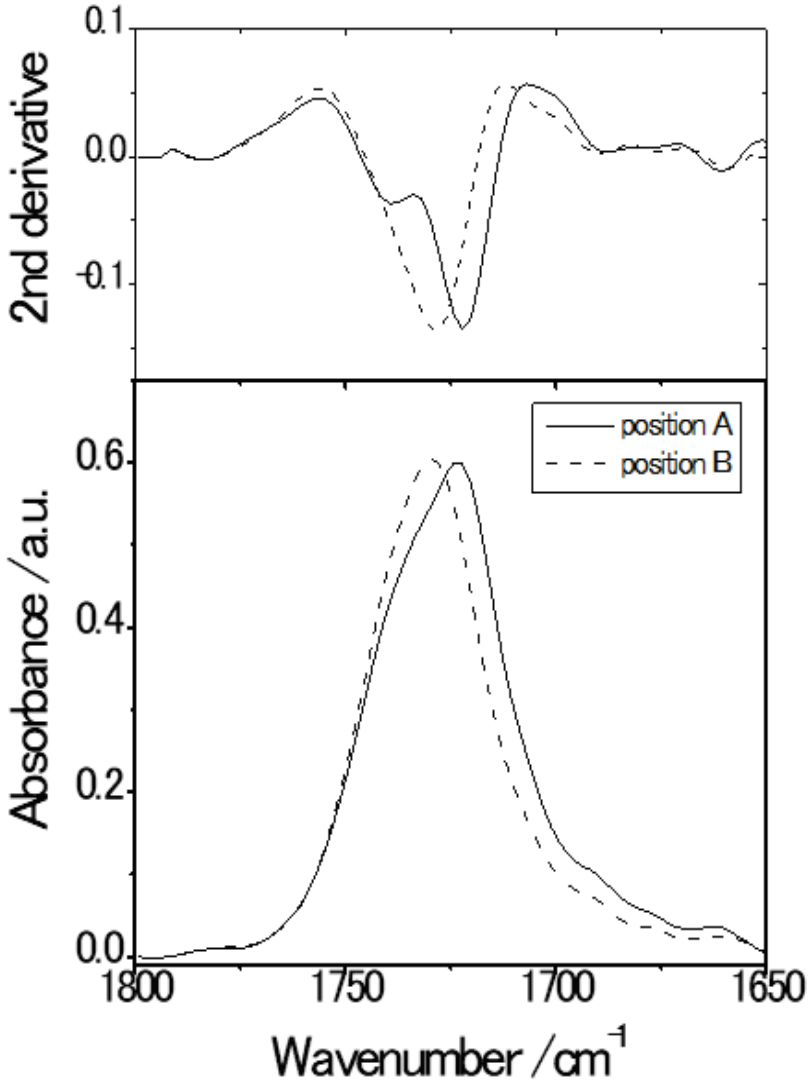

Figure 6.35 Top: ATR-FTIR spectroscopic images of PHB after isothermal crystallization at 160 (left), 155 (middle) and 150 ˚C (right) for 6 hours. These images are based on the distribution of integrated absorbance of the ν (C=O) band of crystalline PHB. Middle: ATR-FTIR spectroscopic images of PLA after isothermal crystallization at 160 (left), 155 (middle) and 150 ˚C (right) for 6 hours. These images are based on the distribution of integrated absorbance of the ν (C=O) band of crystalline PLA. Bottom: FT-IR spectra were extracted from the crystalline PHB-rich domain indicated by a pink circle (position A) and the crystalline PHB-poor domain indicated by a ginger circle (position B) in the top middle image. The second derivative spectra are attached above the FT-IR spectra. (Source [16])

Figure 6.4 shows the change in the normalized integrated absorbance of ν(C=O) band of both crystalline PHB and crystalline PLA as a function of time at different isothermal crystallization temperatures. It was found that the larger gap between isothermal crystallization temperature and T_c, the earlier polymer starts crystallization. When the isothermal crystallization temperature is far from its T_c, crystallization starts before jumping to its isothermal crystallization temperature. This is because the nucleation rate of polymers slows down with increasing isothermal crystallization temperature. [16]

As shown in figure 6.4, it was also found that the degree of crystallization of pure polymers increases with increasing isothermal crystallization time. Its speed at the early stage is high because of the main (bulk) crystallization, and decreases at the late stage because of decreasing crystallizable polymers and spherulitic impingement.[115] Furthermore, with decreasing isothermal crystallization temperature, the speed of crystallization increases and it takes less time to complete the crystallization process. It is because the mobility of polymer chains decreases and they are more difficult to move out from the crystal lattice, which makes the embryos (crystal-like regions) easier to reach their critical radius to form stable nuclei. Furthermore, the increasing density of polymers with decreasing isothermal crystallization temperature also promotes the formation of steady nuclei through density fluctuation.[59] Both of these two factors benefit the nucleation of crystals and thus promote crystallization. [16]

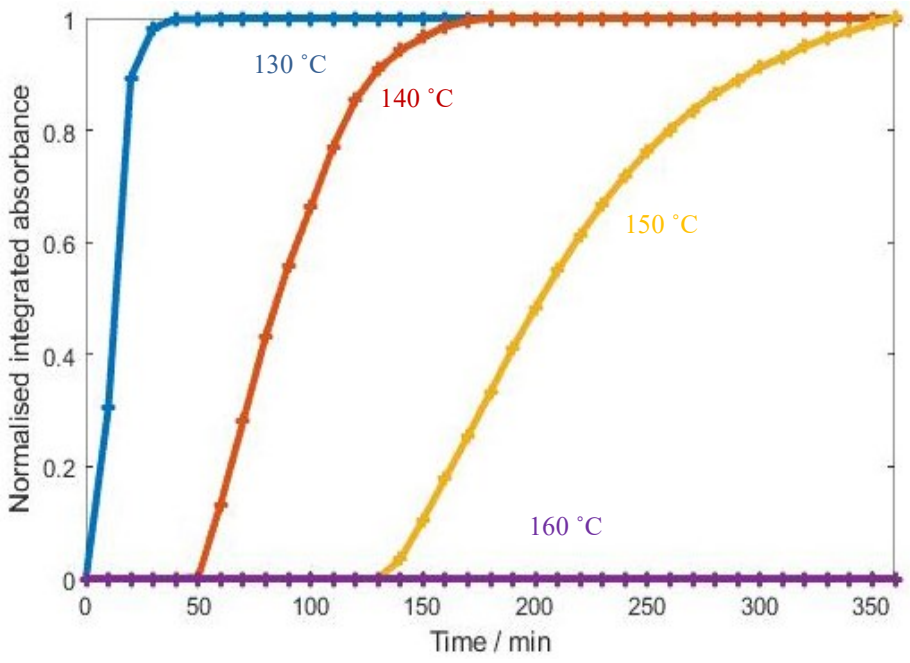

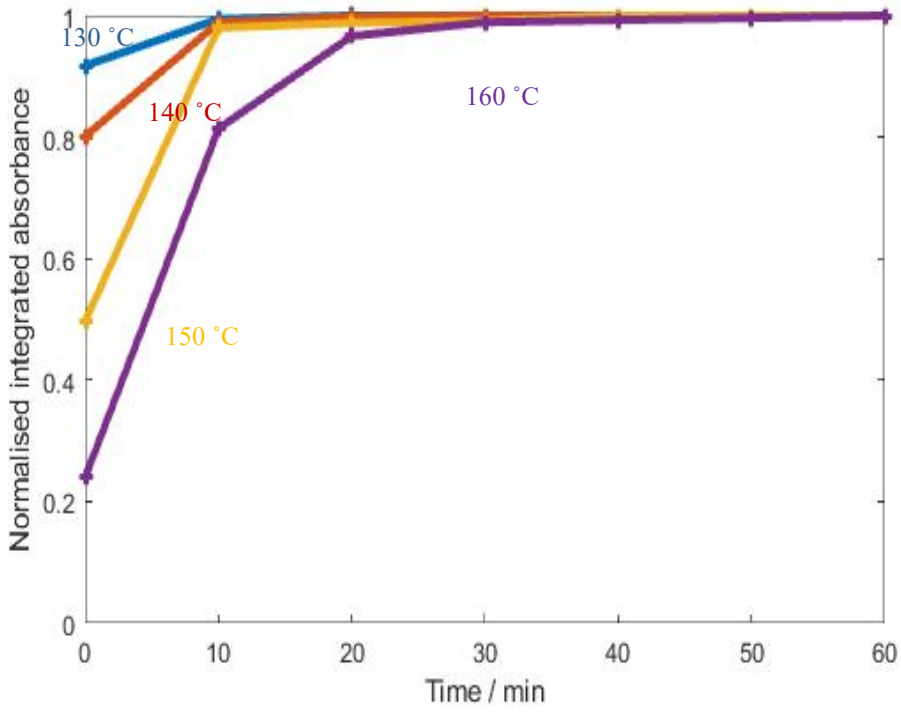

Figure 6.36 The normalized integrated absorbance of the ν (C=O) band of crystalline PHB (top) and the ν(C=O) band of crystalline PLA (bottom) as a function of isothermal crystallization time at 130 (blue), 140 (red), 150 (yellow) and 160 (purple) ˚C. (Source [16]**)**

Figure 6.5 (left) indicates that the concentration of amorphous PHB decreases while the concentration of crystalline PHB increases with decreasing isothermal crystallization temperature. Thus, it is demonstrated that the degree of crystallization in PHB increases with decreasing isothermal crystallization temperature. Below a certain isothermal crystallization temperature (140 °C or less), the increase in the degree of crystallization is only a little. Likewise, as shown in Figure 6.5 (right), the concentration of amorphous PLA decreases while the concentration of crystalline PLA increases with decreasing isothermal crystallization temperature. Although the change in the degree of crystallization is not as obvious as PHB, it can still be demonstrated that the degree of crystallization of PLA increases with decreasing isothermal crystallization temperature. Moreover, it can be found that the broad ν (C=O) band becomes sharper during the isothermal crystallization process, which is due to the band splitting. When an ordered structure like crystal is formed, the

dipole-dipole interactions between the C=O groups lead to band splitting, which agrees with the former research. [16,22]

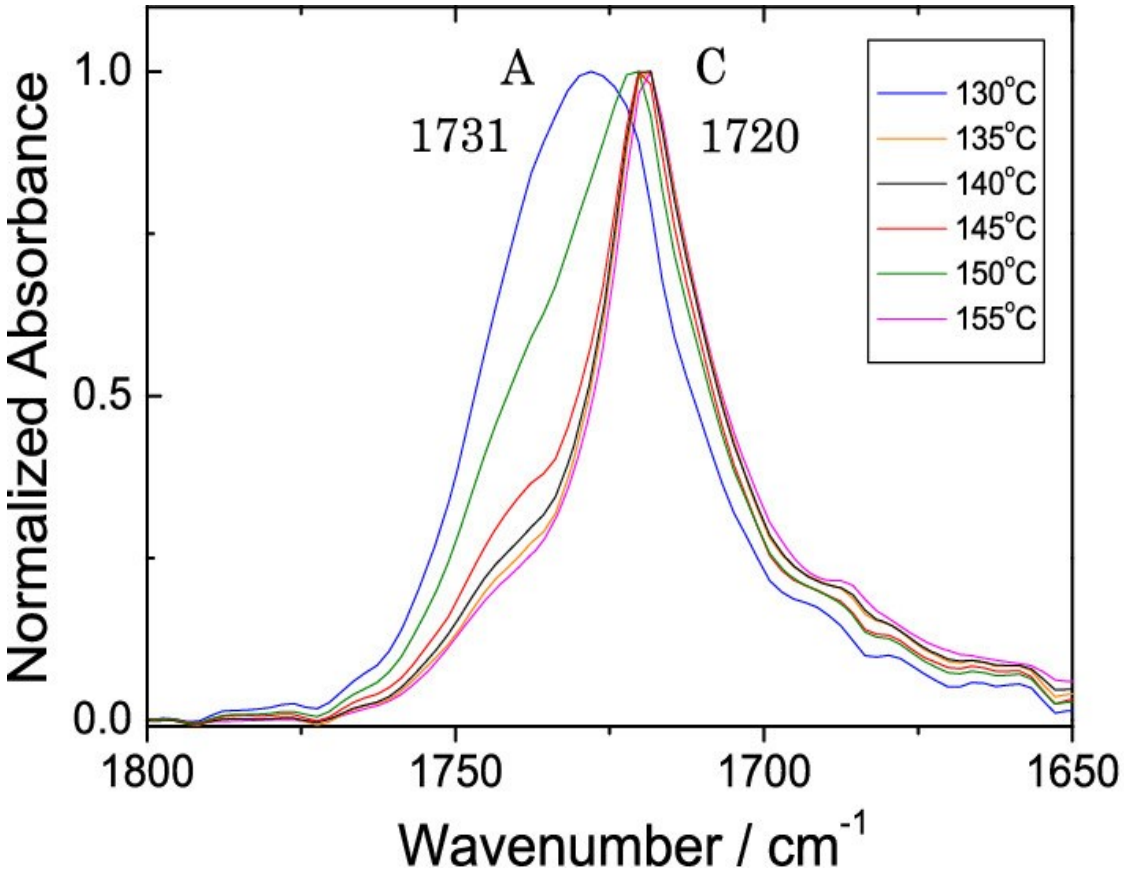

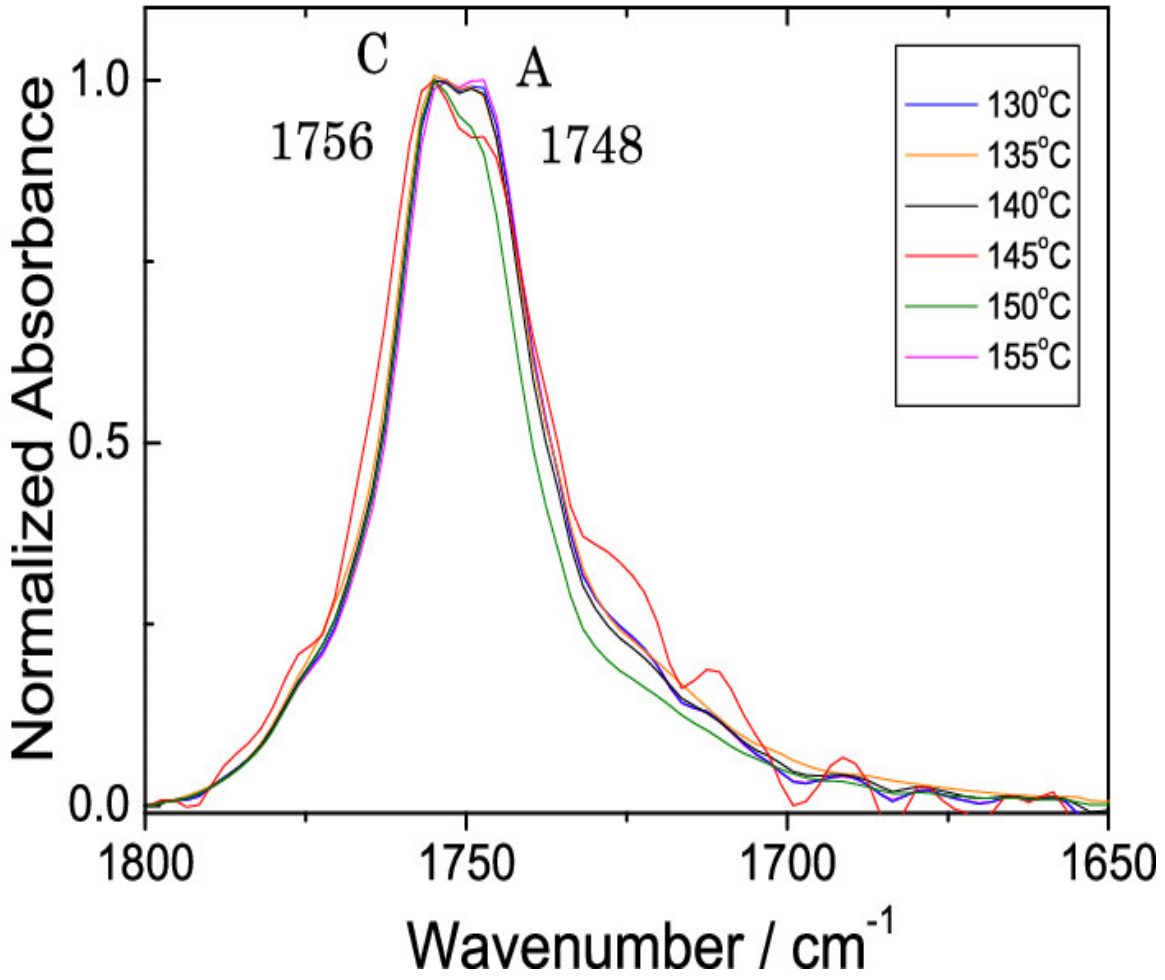

Figure 6.37 ATR-FTIR spectra in the region of ν (C=O) band of PHB (left) and PLA (right) extracted from the whole imaged area after isothermal crystallization at 130 (blue), 135 (orange), 140 (black), 145 (red), 150 (green) and 155 (pink) ˚C for 6 hours. (Where C means crystalline polymer and A means amorphous polymer) (Source [16])

6.3.2 The investigation of isothermal crystallization process of PHB/PLA (50/50) blends

PHB/PLA blend is miscible when the molecular weights of its components are low and it has an UCST curve. Koyama et al. and Blümm et al. have reported that immiscible PHB (M_w = 600,000)/PLA (M_w > 18,000) blends become miscible at room temperature with decreasing M_w of PLA. This is because the UCST curve goes down with decreasing molecular weight of PLA. [16,66,68,116]

In the former study, time-resolved FTIR spectroscopy was applied to investigate the isothermal crystallization process of miscible and immiscible PHB/PLA blends. [84,88] During the isothermal crystallization process of the miscible polymer blend, only one peak in the ν (C=O) band region can be observed at the molten state and it stays at the same position when its absorbance increases with time. Moreover, if T_m of each blend component are similar, simultaneous crystallization of PHB and PLA will occur in the miscible polymer blend. During the isothermal crystallization process of the immiscible polymer blend, an extra shoulder peak can be found in the ν (C=O) band region at the molten state. Instead of simultaneous crystallization, stepwise crystallization of PHB and PLA occurs in the immiscible polymer blend. As a result, it is proved that the miscibility of polymer blend has great effects on the crystallization behaviour of both polymers in the blend. In this work, with the advanced in situ ATR-FTIR spectroscopic imaging, the isothermal crystallization process of polymer blend (from the miscible molten state to the immiscible crystalline state) was explored. [16]

Figure 6.6 shows the time-dependent ATR-FTIR spectra of PHB/PLA blend during isothermal crystallization at 145 ˚C and their second derivative. The isothermal melt-crystallization process of PHB/PLA blends is the same as that of homopolymers. The factor that PHB/PLA (50/50) blends are miscible at the molten state can be proved by the only one peak (1734 cm^{-1}) in the ν (C=O) band region in the spectra. This band peaked at 1734 cm^{-1} consists of these ν (C=O) bands of molten PHB (1731 cm^{-1}) and molten PLA (1745 cm^{-1}). Because both amorphous PHB and PLA are liquid at their T_m, they are easy to mix and then lead to their homogeneous distribution in the polymer blend. Thus, it is assumed that amorphous PHB and PLA are intermolecularly mixed. Second derivatives were prepared to highlight the spectral changes during the isothermal crystallization process because of the overlapped bands of PHB and PLA in the original ATR-FTIR spectra. These three strong peaks at 1720, 1734, and 1756 cm^{-1} are assigned to the ν (C=O) bands of crystalline PHB, miscible PHB/PLA (50/50) blend, and crystalline PLA, respectively. The decreasing absorbance of the ν (C=O) band of miscible PHB/PLA blend indicates the decreasing concentration of amorphous polymers. While the increasing absorbance of the ν (C=O) band of crystalline PHB and PLA indicates the increasing concentration of crystalline polymers. Because crystallinity of PLA is low while that of PHB is high, the ν (C=O) band of amorphous PLA remains while that of amorphous PHB disappears after annealing at 145 ˚C.

It can be demonstrated that both amorphous PHB and PLA in the blend crystallize during the isothermal crystallization process. [16]

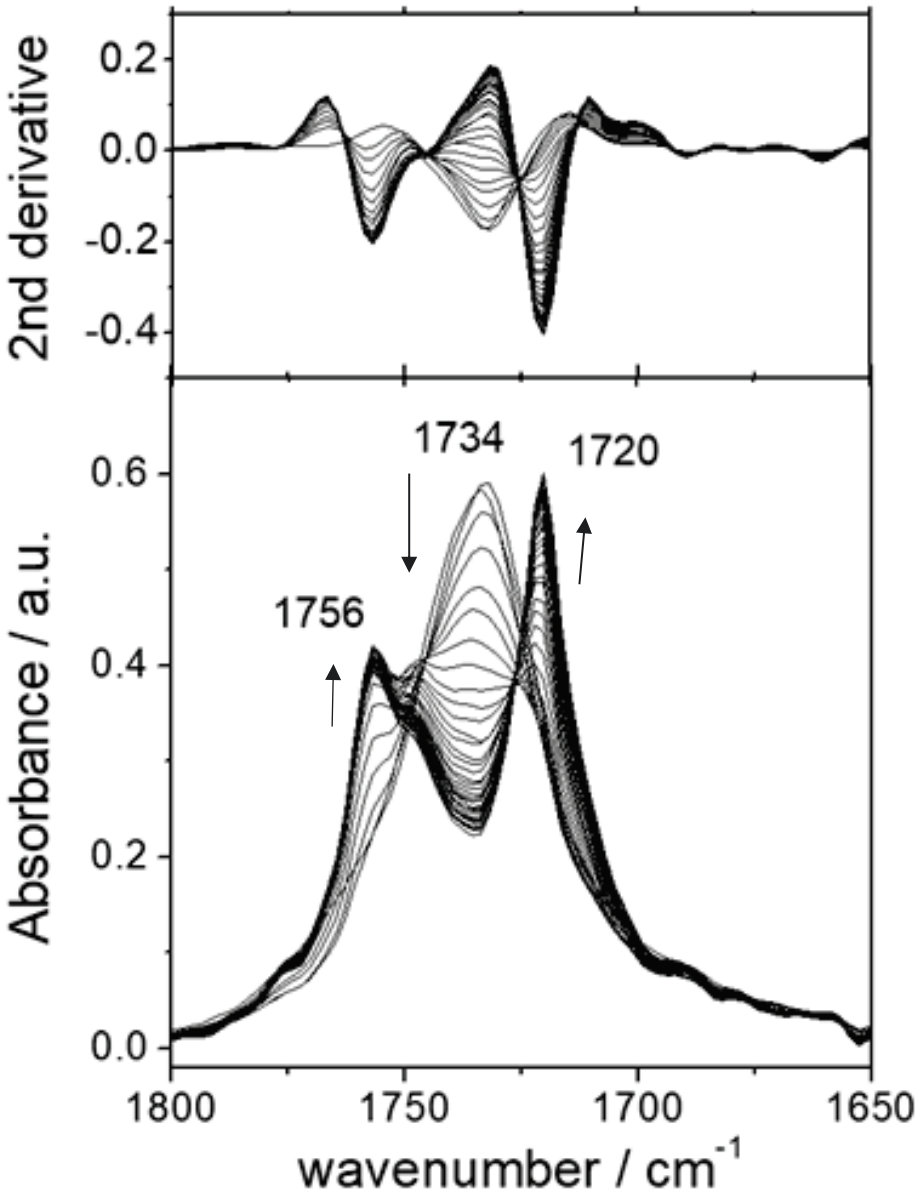

Figure 6.38 Time-dependent ATR-FTIR spectra of PHB/PLA (50/50) blend during isothermal crystallization at 145 ˚C (bottom) and their second derivative (top). (Source [16]**)**

Figure 6.7(a) depicts only a small amount of amorphous PLA crystallizes while amorphous PHB does not crystallize in the blend after annealing at 160 ˚C, which is indicated by the slight increase in the absorbance of the ν (C=O) band of crystalline PLA (1756 cm^{-1}) and no apparent ν (C=O) band of crystalline PHB. This result is constant with pure polymers above. Figure 6.7(b) reveals that the ν (C=O) band shows a shift from 1734 cm^{-1} (miscible state of the PHB/PLA blend) to 1720 cm^{-1} (crystalline state of pure PHB) during the annealing process at 140 ˚C. It means that crystalline PHB appears from the miscible PHB/PLA blend. The intermolecular interaction between PHB and PLA molecules in the miscible state turns to the inter- and intramolecular interaction between PHB and PHB molecules in the immiscible state. [16]

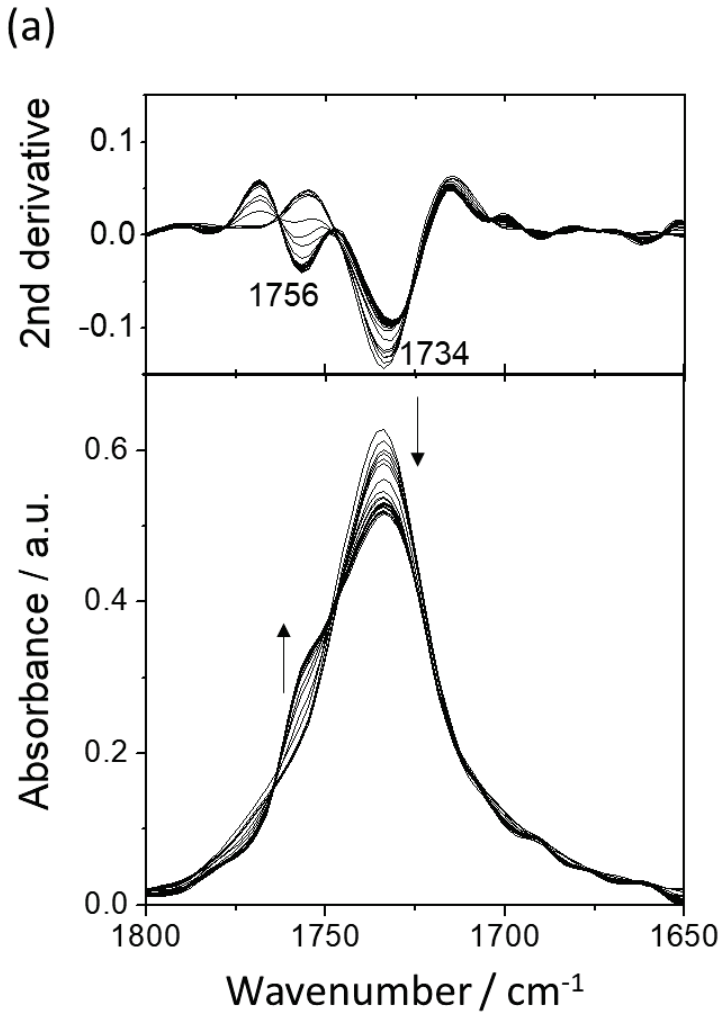

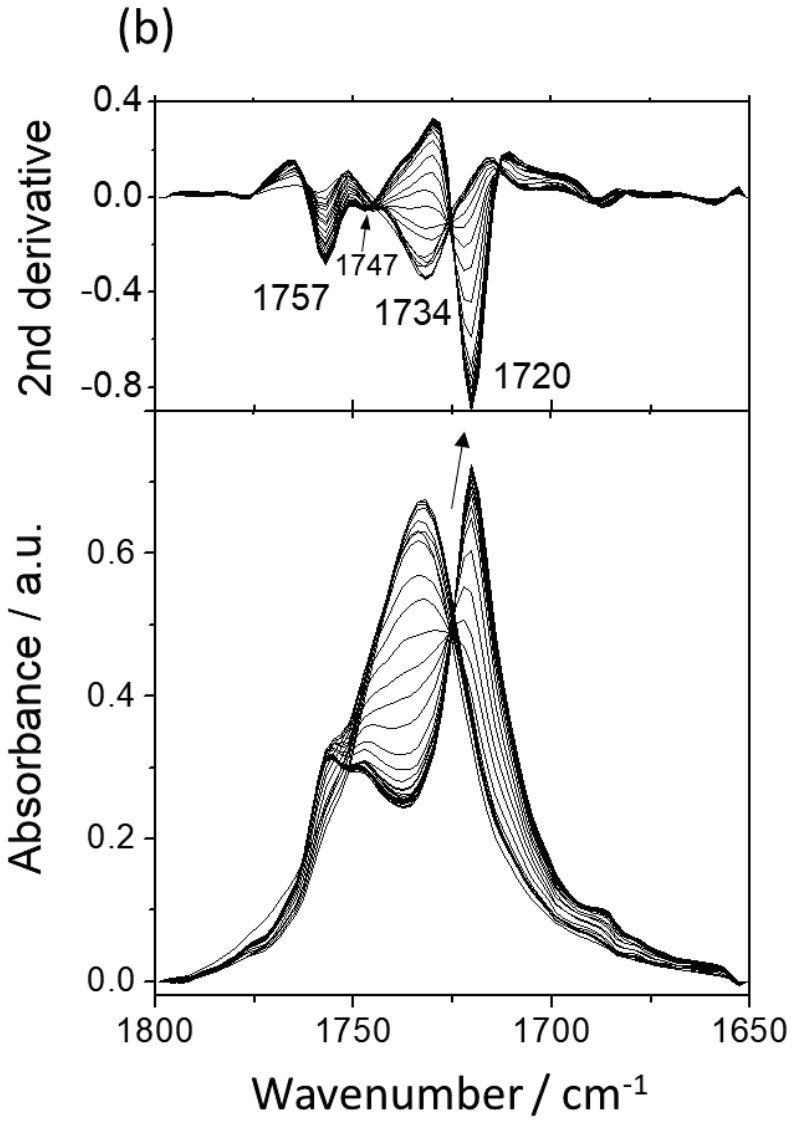

Figure 6.39 Time-dependent ATR-FTIR spectra in the ν (C=O) band region of PHB/PLA (50/50) blend during isothermal crystallization at (a) 160 and (b) 140 ˚C. (Source [16]**)**

Figure 6.8 shows the ATR-FTIR spectroscopic images of the PHB/PLA blend which was measured soon after the temperature decreases to 150 ˚C, 60, 120, 180, and 360 min later. The occurrence of phase separation during the isothermal crystallization process is indicated by the appearance and gradual separation of crystalline PHB-rich domains and crystalline PLA-rich domains in these spectroscopic images. Soon after the temperature decreases to 150 ˚C, both PHB and PLA are amorphous. After 60 min, PHB does not crystallize while PLA

starts crystallization. The relatively higher concentration of crystalline PLA at the top part of images implies that phase separation starts before the occurrence of crystallization in the polymer blend, which agrees with the previous research of Chuang et al. [69,117] This is because PHB does not have enough free energy to come over the energy barrier of the stable nucleus formation at the early stage. [117] The size change and graduate separation of crystalline PHB-rich domains and crystalline PLA-rich domains indicate that the extent of phase separation is enhanced with increasing annealing time. After 6 h, it can be observed that crystalline PHB-rich domains and crystalline PLA-rich domains are separated to a great extent. Spectra in figure 6.8 (bottom) also demonstrate that the concentration of crystalline PLA in the crystalline PLA-rich domains is higher than that in crystalline PLA-poor domains and the concentration of crystalline PHB in the crystalline PHB-rich domains is higher than that in crystalline PHB-poor domains. As a result, it can be demonstrated that phase separation occurs before crystallization and then they proceed simultaneously. [16]

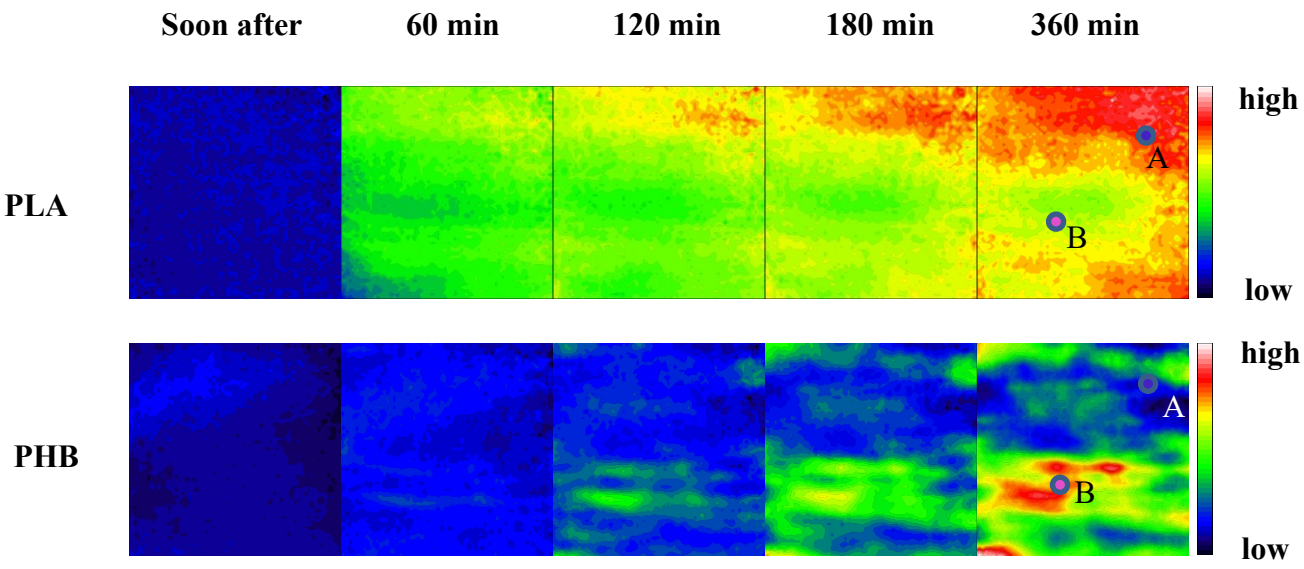

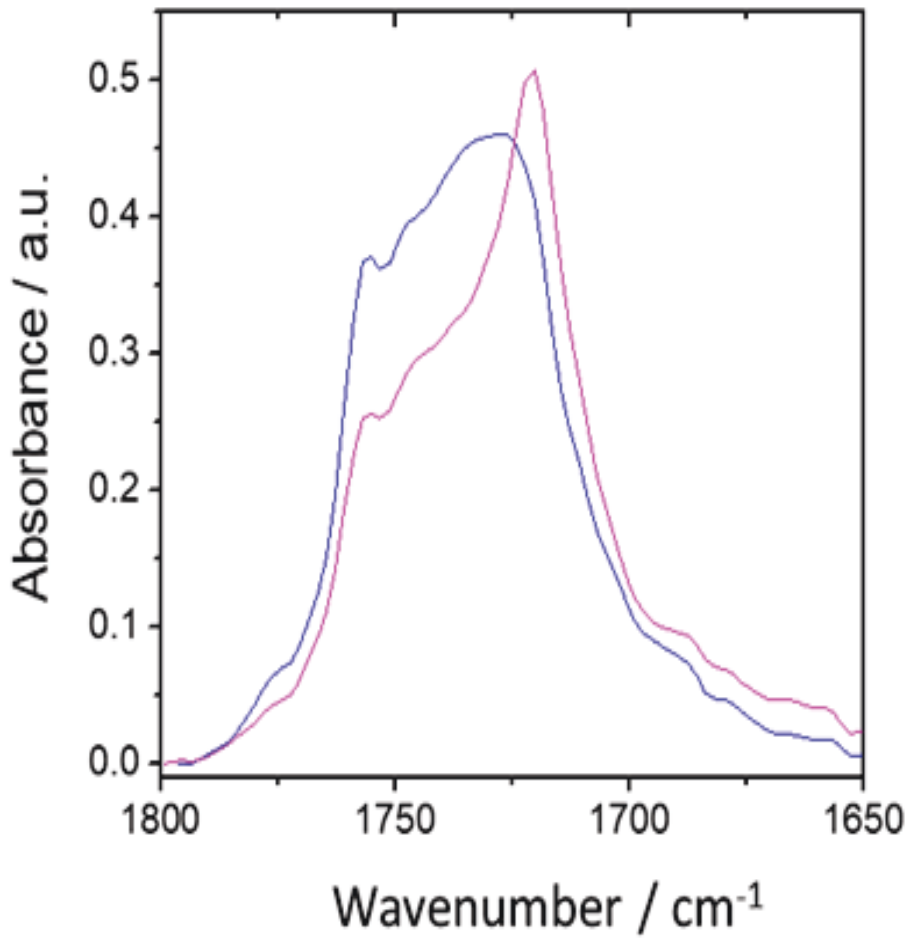

Figure 6.40 Top: ATR-FTIR spectroscopic images of the PHB/PLA blend measured soon, 60 min, 120 min, 180 min and 360 min after temperature decreases to 150 ˚C. The top row images were developed based on the distribution of integrated absorbance of the ν (C=O) band of PLA crystal while the bottom row images were obtained based on that of the ν (C=O) band of PHB crystal. Bottom: spectra were extracted from the PLA crystal-rich domain indicated by a dark blue circle (position A) in the top right image and the PHB crystal-rich domain indicated by a pink circle (position B) in the middle right image. (Source [16])

As mentioned in Section 6.3.1, T_c for pure PHB is below 160 ˚C while that for pure PLA is above 160 ˚C, which means that the critical temperature of phase separation and crystallization in the PHB/PLA blend is less than 160 ˚C. PHB/PLA (50/50) blend samples

were annealed at different isothermal crystallization temperatures in this work. It was found that both phase separation and crystallization occur in the blend when the annealing temperature is 150 ˚C. When the annealing temperature is 155 ˚C, PHB in the polymer blend does not crystallize even after annealing for 6 h, which was indicated by the fact that no ν (C=O) band of crystalline PHB appears in the spectra. This is because the appearance of PLA affects the crystallization of PHB and also leads to T_m depression. [118] Thus, it can be concluded that the critical temperature for phase separation and crystallization of PHB/PLA (50/50) blends is between 150 and 155 ˚C. [16]

The effect of isothermal crystallization temperature on the extent of phase separation in the polymer blend was also investigated. As shown in figure 6.9, crystalline PHB-rich domains and crystalline PLA-rich domains are separated to a great extent when the isothermal crystallization temperature is 150 ˚C. Since PHB is partially crystallized even after annealing for 6 h, there is no PHB crystal on the top side of images. Thus, it suggests that the extent of phase separation is very high because there is no crystalline PHB in the crystalline PLA-rich domains. When the annealing temperature is 145 ˚C, most crystalline PHB-rich domains and crystalline PLA-rich domains are separated but some of them are overlapped. With a lower annealing temperature, crystalline PHB-rich domains and crystalline PLA-rich domains are more overlapped and less separated. As a result, it is concluded that the extent of phase separation in the blend is weaker with decreasing annealing temperature. [16]

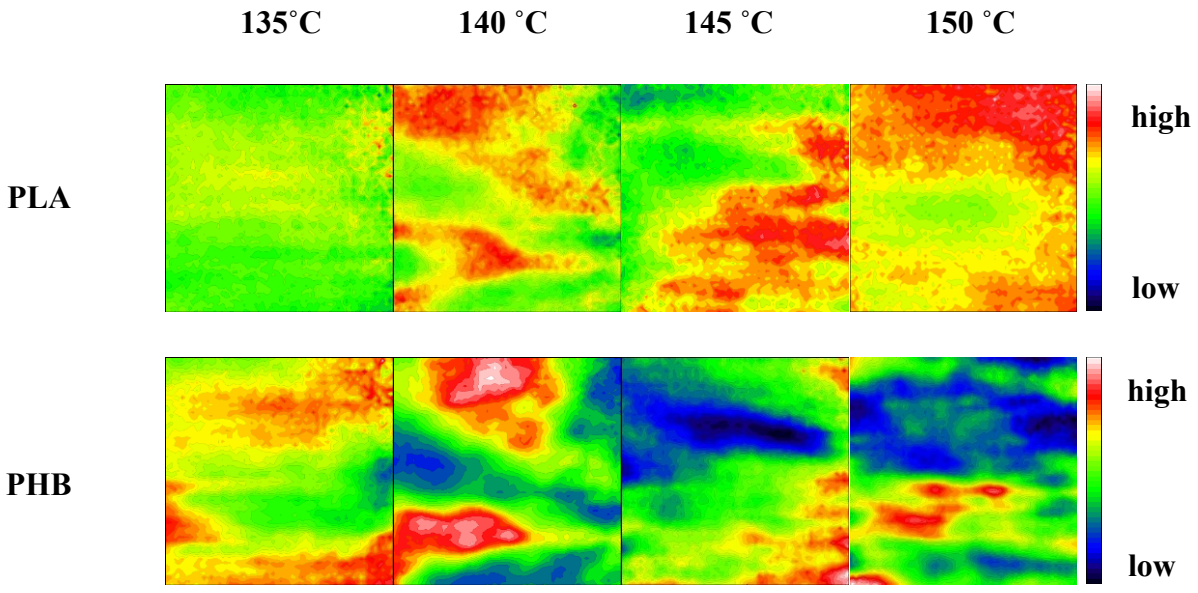

Figure 6.41 ATR-FTIR spectroscopic images of the PHB/PLA blend after cooling to the isothermal crystallization temperature at 135, 140, 145 and 150 ˚C for 6 hours. The top row images are based on the distribution of integrated absorbance of the ν (C=O) band of PLA crystal while the bottom row images are based on that of the ν (C=O) band of PHB crystal. (Source [16]**)**

The normalized integrated absorbance change in the ν (C=O) band of crystalline polymers in the blend with increasing annealing time was plotted to explain this phenomenon. Since PHB is partially crystallized and not all of the imaged area is occupied by crystalline PHB at 150 ˚C, the normalized integrated absorbance change in the ν (C=O) band of crystalline polymers at this temperature was not discussed in this chapter. As shown in figure 6.10, the isothermal crystallization process of polymers in the blend has a similar trend as that of pure polymers before blending shown in figure 6.4. With increasing annealing temperature, the crystallization start time of polymers becomes later and the crystallization process time becomes longer. This finding is consistent with the study of Hashimoto that the greater thermodynamic driving force leads to the earlier stage where the coarsening starts. [16,119]

It is also found that the rate of PLA crystallization after annealing at 140 ˚C is abnormally faster than that after annealing at 135 ˚C in the first 40 min. In pure polymers, there are only two factors that affect the rate of crystallization: the decreasing mobility and the increasing thermodynamic driving force with increasing undercooling. In polymer blends, another factor can also affect the rate of crystallization: the existence and crystallization of both blend components affect each other. [62] This factor will be discussed further in the next section. The rate of crystallization of polymers in the blend is lower than that without mixing, which is due to the appearance of other blend component and the dilution effect: the concentration of each blend component decreases after being mixed. When the annealing temperature is 145 ˚C, the rate of crystallization in PLA after 100 min is abnormally high. This is because PHB starts crystallization later and a smaller number of PHB crystals and nuclei have a weaker restriction on the crystallization of PLA. Moreover, PHB completes crystallization after 6 h so that the reduction of PHB crystallization rate is not shown in the profiles. [16]

In summary, the lower annealing temperature leads to the earlier start of polymer crystallization and less time for amorphous polymers to phase separate. The formed polymer

crystal is more stable and then becomes more difficult to phase separate. Moreover, PLA starts crystallization ahead of the temperature reaches the annealing temperature and then the PLA crystals fill the whole blend very fast. The resulting spatially limited region confines the movement of amorphous PHB. Both of these two factors 'freeze' the polymer chains and then prevent the further phase separation of polymer blend. In other words, the diffusion-limited mobility of polymers is the main reason for the weaker extent of phase separation with decreasing annealing temperature. On the other hand, the longer crystallization process time with increasing annealing temperature lets the lamellar stacks have more opportunities to expel the other type of polymer outside, which can enhance the extent of phase separation. This new discovery is meaningful to the process of UCST crystallizable polymer blend because the phase separation can be controlled through reducing the annealing temperature. [16]

(a)

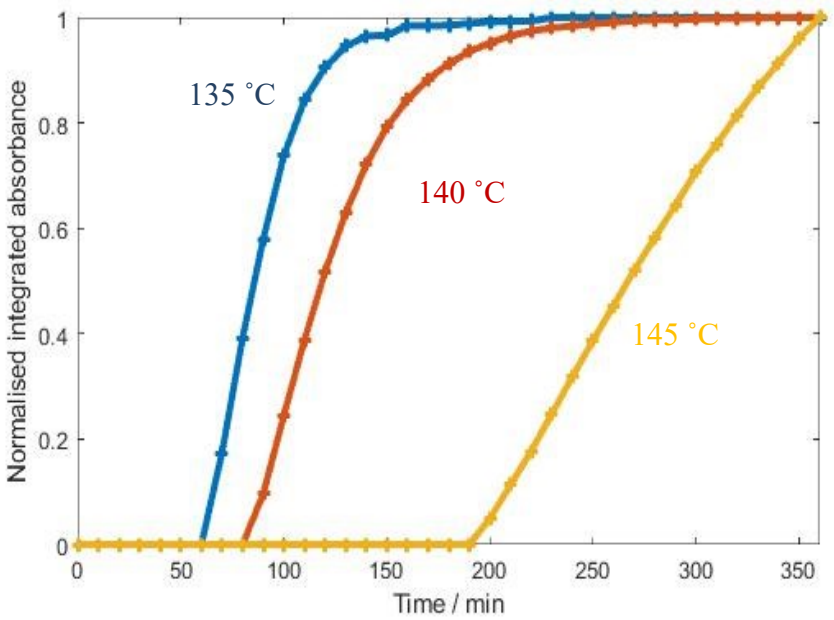

(b)

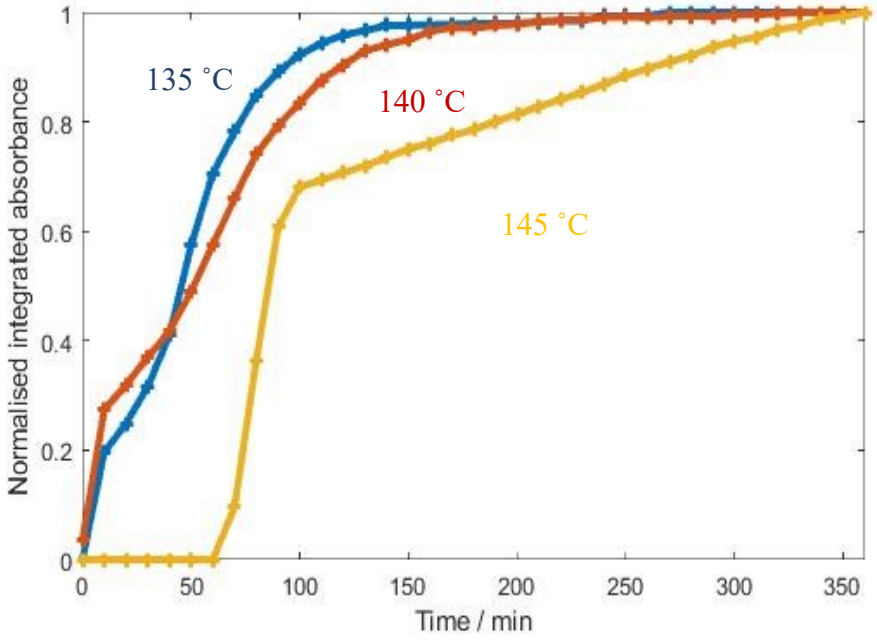

Figure 6.42 (a) Normalized integrated absorbance of the ν (C=O) band of crystalline PHB and (b) that of the ν (C=O) band of crystalline PLA in the polymer blend as a function of time extracted from the whole imaged area at 135 (blue), 140 (red), and 145 (yellow) ˚C. (Source [16])

As shown in figure 6.11, it can be observed that the degree of crystallization of PHB in the blend decreases with increasing annealing temperature, which is constant with the crystallization of PHB without blending. It is because the crystallization of PLA almost finishes when PHB starts crystallization. Furthermore, the degree of crystallization in PLA is lower than that of PHB, which was proved by the spectra shown in figure 6.11. Thus, the PLA crystals and nuclei do not affect PHB crystallization much. Likewise, the degree of crystallization of PLA in the blend also decreases with increasing annealing temperature from 140 to 155 ˚C, which is constant with the crystallization of PLA without blending. The reason for the lower degree of crystallization is because PHB starts crystallization after PLA almost finishes. Thus, the early stage of PLA crystallization, during which most PLA crystals form,

is not affected much by PHB crystallization except at too low isothermal crystallization temperature. [16]

The abnormally low degree of crystallization in PLA at 135 ˚C is because the large amount of PHB nuclei and crystal in the blend confines the PLA crystallization. After annealing at 135 ˚C, PHB starts crystallization very quickly and the degree of crystallization is also the highest. Moreover, the extent of phase separation is the weakest at that annealing temperature so that the concentration of PLA in PLA-rich domains is not high so that the dilution effect will also restrict its crystallization. [16]

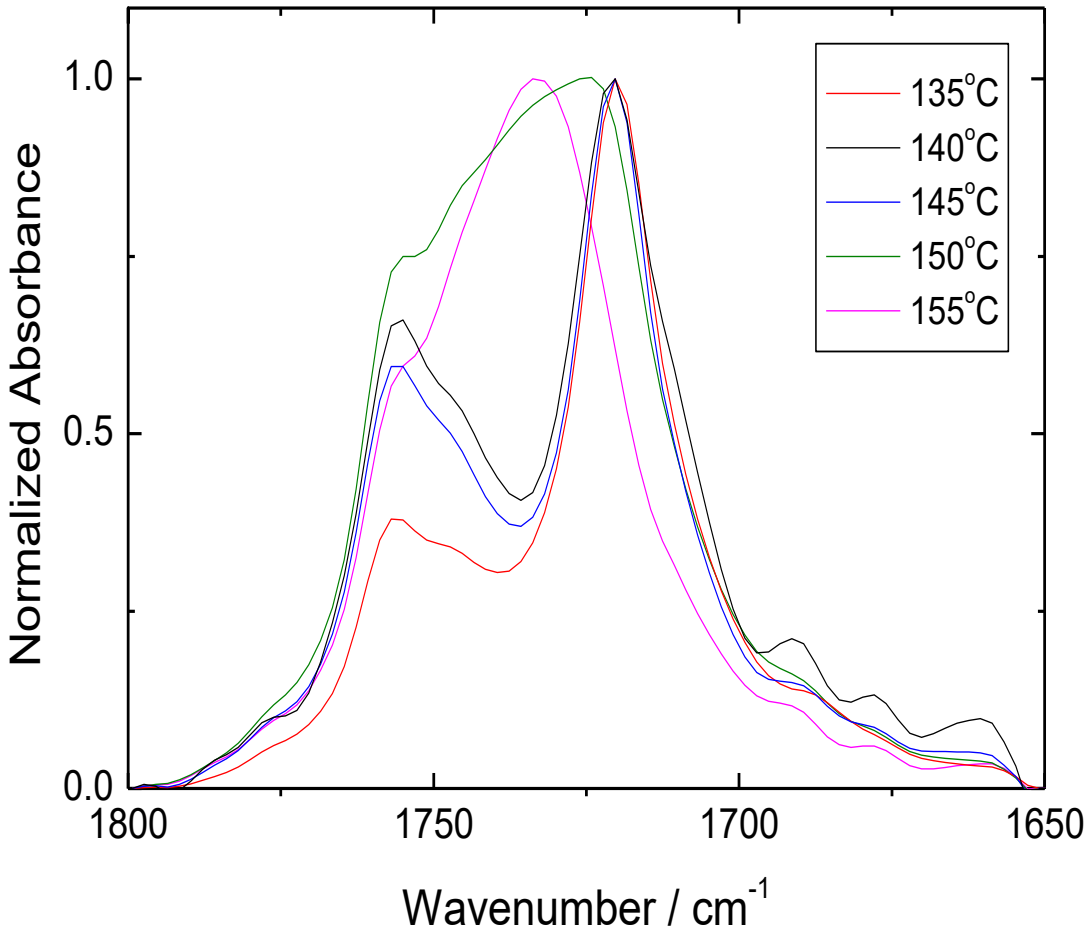

Figure 6.43 ATR-FTIR spectra in the region of ν (C=O) band of PHB/PLA blend extracted from the whole imaged area after isothermal crystallization at 135 (red), 140 (black), 145 (blue), 150 (green) and 155 (pink) ˚C for 6 hours. (Source [16])

6.3.3 Mechanism of phase separation and crystallization in the UCST crystallizable polymer blend

The mechanism proposed in the former research [112,117] was validated through the simultaneous visualization of crystallization and phase separation in polymer blends in this work. The coexistence and competition of crystallization and phase separation in the region below the melting curve of phase diagram, which was proposed by Chuang et al [117], are proved by the spectroscopic images in Figure 6.9. Meanwhile, more evidence was provided for the crystallization-induced phase separation [112], which was discussed in detail below. Moreover, new information revealed in this work was used to supplement and improve this mechanism. For example, the ATR-FTIR spectra (figure 6.7) indicate the transformation of intermolecular interaction between different polymers in the miscible blend to the intra- and intermolecular interactions between the same type of polymers in the phase-separated blend. More importantly, in the past, only several intermediate structures and the final structure were available to analyse because of the limitation of the conventional technology. Thus, most mechanisms proposed in the previous studies are segmentary and some important information, such as the change in the extent of phase separation, is lacked because the whole dynamic process has never been monitored in situ. [16]

According to the results obtained in this work, the mechanism of phase separation and crystallization in UCST crystallizable polymer blend during the isothermal crystallization process was summed. Figure 6.12 reveals the whole dynamic process of isothermal crystallization process. (1) After temperature reaches the critical point, amorphous-amorphous phase separation occurs and then amorphous PHB-rich domains and amorphous PLA-rich domains are formed. (2) The resulting local density fluctuations let the amorphous polymers have enough energy to overcome the energy barrier and then form nuclei. The PHB-rich domains behave as nuclei when they surround the PLA-rich domains, while the PLA-rich domains behave as nuclei when they surround the PHB-rich domains. These surrounded blend component-rich domains act as seeds for crystallization and then outward lamellar growth starts. (3) The phase separation-induced amorphous polymer-rich domains can accelerate the crystallization. This is because the amorphous polymer in this area has a higher concentration than other areas, which can promote the primary nucleation of the crystal. However, compared with pure polymer, the rate of crystallization is relatively slow

because of the dilution effect. PHB nuclides in the PHB-rich domains aggregate into the early-stage PHB spherulites while PLA nuclides in the PLA-rich domains aggregate into the early-stage PLA spherulites. On the other hand, PHB in PLA-rich domains (PHB-poor domains) and PLA in PHB-rich domains (PLA-poor domains) are difficult to nucleate because of their low concentrations in these areas. As the isothermal crystallization process proceeds, crystallization becomes the main process because the small diffusion constant in the crystalline polymer region hinders the phase separation. But the phase separation is not totally stopped because the crystal rejects the amorphous polymer into interlamellar, interfibrillar, and interspherulitic regions through using the stabilizing force during the lamella growth. [112] For instance, the PLA crystal rejects the amorphous PHB or the PHB crystal rejects the amorphous PLA. Then, larger amorphous polymer-rich domains are formed by merging the rejected amorphous polymers to minimize the surface energy. (4) Finally, the amorphous polymer in these amorphous polymer-rich domains starts crystallizing. The mechanism proposed above explains the observation through these ATR-FTIR spectroscopic images directly. [16]

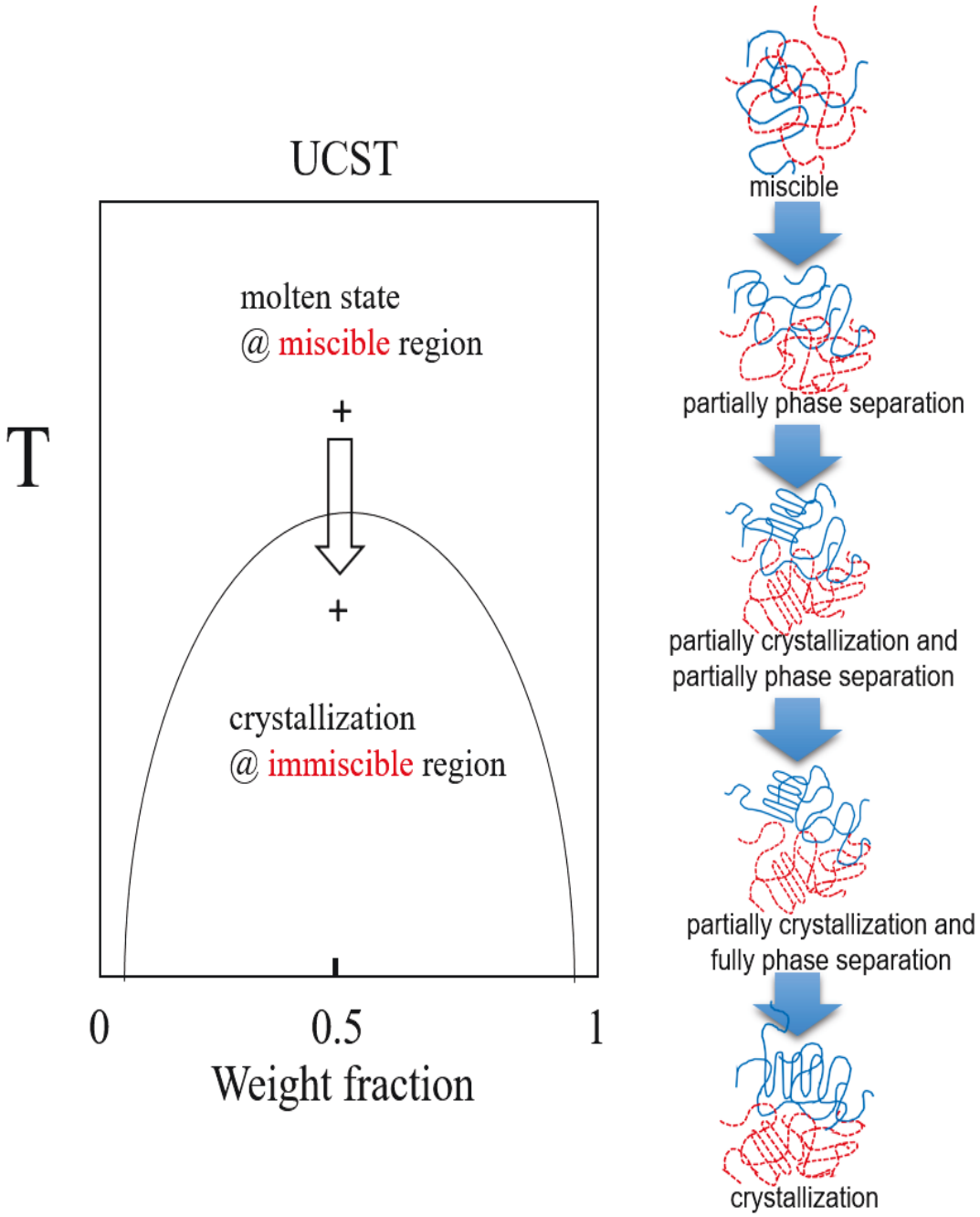

Figure 6.44 A schematic illustration of the whole dynamic process of phase separation and crystallization of PHB/PLA blends studied by in situ ATR-FTIR spectroscopic imaging. (Source [16])

6.4 Conclusions

In this chapter, the simultaneous visualization of the crystallization and phase separation in PHB/PLA blends has been realized for the first time through utilizing in situ ATR-FTIR spectroscopic imaging. [16]

First, the isothermal crystallization processes in pure polymers without blending: PHB and PLA were investigated. The upper critical crystallization temperature (T_c) and the onset time of crystallization at different annealing temperatures were obtained. It was observed that the degree of crystallization in polymers is enhanced with increasing annealing time. Furthermore, the rate of crystallization and the final degree of crystallization both decrease with increasing annealing temperature. [16]

Then, the isothermal crystallization process of PHB/PLA (50/50) blends was investigated. The peak shift of ν (C=O) band of PHB during the process indicates that the intermolecular interaction between PHB and PLA molecules in the miscible state changes to the inter- and intramolecular interactions between PHB and PHB molecules in the immiscible state. As shown in the obtained ATR-FTIR spectroscopic images, the appearance and gradual separation of crystalline PHB-rich domains and crystalline PLA-rich domains indicate the occurrence and progress of phase separation during the isothermal crystallization process. The increasing size of these two types of domains in the images and the increasing absorbance of the ν (C=O) band of the crystalline polymers in the spectra, which were observed simultaneously, both indicate the greater degree of crystallization with increasing annealing time. The critical temperature for phase separation and crystallization in the PHB/PLA (50/50) blend is between 150 and 155 ˚C. Since the faster crystallization rate leaves less time for amorphous polymers to phase separate, the extent of phase separation in the blend becomes weaker with decreasing annealing temperature. The degree of crystallization in the blend components decreases with increasing annealing temperature. [16]

Finally, the mechanism of the isothermal crystallization process in the UCST crystallizable polymer blend was summarized. Decreasing the annealing temperature is proved to be an effective method to constrain phase separation between these two blend components and tailor the final morphology in UCST crystallizable polymer blends for practical applications. [16]

Chapter Seven

Visualization of inter- and intramolecular interactions in PHB/PLA blend during isothermal melt-crystallization using ATR FTIR spectroscopic imaging

7. Visualization of inter- and intramolecular interactions in PHB/PLA blend during isothermal melt-crystallization using ATR FTIR spectroscopic imaging

This chapter presents the application of in situ ATR-FTIR spectroscopic imaging to study the inter- and intramolecular interactions in PHB/PLA blends during isothermal melt-crystallization. These interactions in multicomponent polymer systems have great effect on their physical and chemical properties and thus have significant implications on their synthesis and processing. [17]

In chapter 6, it was found that the peak position of ν (C=O) band can reflect the nature of intermolecular interactions. The peak shift indicates that the intermolecular interactions between PHB and PLA in the miscible state (1733 cm^{-1}) turns to the inter- and intramolecular interaction (CH_3···O=C, 1720 cm^{-1}) within PHB crystal during the isothermal melt crystallization. However, these obtained ATR-FTIR spectroscopic images based on integrated absorbance can only reveal the spatial distribution of blend components. Thus, in this chapter, I proposed a novel approach of plotting the peak position of a spectral band to reflect the spatial distribution of different intra- and intermolecular interactions. The obtained ATR-FTIR spectroscopic images based on the band position visualized the disappearance of the intermolecular interaction between PHB and PLA and the appearance of the inter- and intramolecular interactions within the PHB crystal during isothermal melt-crystallization. [17]

7.1 Motivation and scientific background

PHB is one of the most popular biopolymers derived from microorganisms. T_g of this semi-crystalline polyester is approximately 4 °C. [120–123] PLA is also a biodegradable semi-crystalline polyester, which can be derived from chemical synthesis.[75,106] Like PHB, it is also a widely used biodegradable polymer. The melting temperatures of high molecular weight PHB and PLA are similar, which are between 170 °C and 180 °C. PHB has a high

degree of crystallization (approximately 60-70% for the perfect stereo regularity produced by bacteria) while PLA has a lower degree of crystallization because of its slower rate of crystallization. In the crystal lamellae of PHB, there is an intermolecular hydrogen bond between the H atom of CH_3 group and the O atom of C=O group, which can link two adjacent parallel chains. Although this type of hydrogen bonding is weak, it plays an important role in chain folding and stabilization of the crystal lamellae. [67,109,132–134,124–131] It can also affect the polymer process greatly through enhancing the 'molecular friction' in the polymer molecular chain. [17]

Apart from biodegradability and biocompatibility, the properties of PHB/PLA blends can be controlled by the blend composition, which results in the expansion of applications. It was reported that in the molten state, PHB/PLA blends with high molecular weight blend components are inhomogeneous while those with a low molecular weight PLA (M_w < 18,000) are miscible. [6,66,68,84] Because both blend components are semi-crystalline polymers, PHB/PLA blends crystallize at the temperature below their T_m. PHB (M_w = 5,000)/PLA (M_w = 50,000) blends show UCST curves in the available temperature range. In chapter 6, simultaneous visualization of crystallization and phase separation in PHB/PLA blends was realized using in situ ATR-FTIR spectroscopic imaging. The appearance and gradual separation of crystalline polymer-rich domains were indicated in the time-dependent spectroscopic images. [16] An important finding in this study is that as phase separation progresses, the intermolecular interactions between PHB and PLA in the miscible state change to inter- and intramolecular hydrogen bonds between PHBs in the immiscible state. Because the position of ν (C=O) band in the spectrum reveals the situation of inter- and intramolecular hydrogen bonds, the change of interactions leads to a unique peak shift of the ν (C=O) band, which cannot be observed in the spectrum of immiscible PHB/PLA blend and PHB homopolymer.[84] Thus, this chapter aims to visualize the change of intra- and intermolecular interactions induced by crystallization and phase separation using ATR-FTIR spectroscopic images based on the band position. [17]

This methodology was invented by Chan et al to observe the crystalline polymorphs of drugs. [135] After then, Shinzawa et al applied the NIR imaging analysis based on band position shift to the tablet analysis containing cellulose. [136,137] In this chapter, we attempted to use ATR-FTIR spectroscopic images based on the band position to analyse inter- and intramolecular interactions in PHB/PLA blends. Furthermore, through comparing the images

based on the band position with the images based on the integrated absorbance, [5,9,15,36,41,138,139] we can demonstrate the potential of ATR-FTIR spectroscopic images based on the band position as a new method to visualize different types of inter- or intramolecular interactions. To the best of our knowledge, this work is the first attempt to visualize different types of inter- or intramolecular interactions between polymer molecules in the multicomponent polymer system using spectroscopic images based on the band position. [17]

7.2 Experimental Section

7.2.1 Materials

PHB (M_w = 5,000 g/mol, Figure 7.1(a)) and PLA (M_w = 50,000 g/mol, Figure 7.1(b)) used in this chapter are the same as those used in Chapter 6. T_m of these two polymers are 163 and 182 ˚C, respectively. [17]

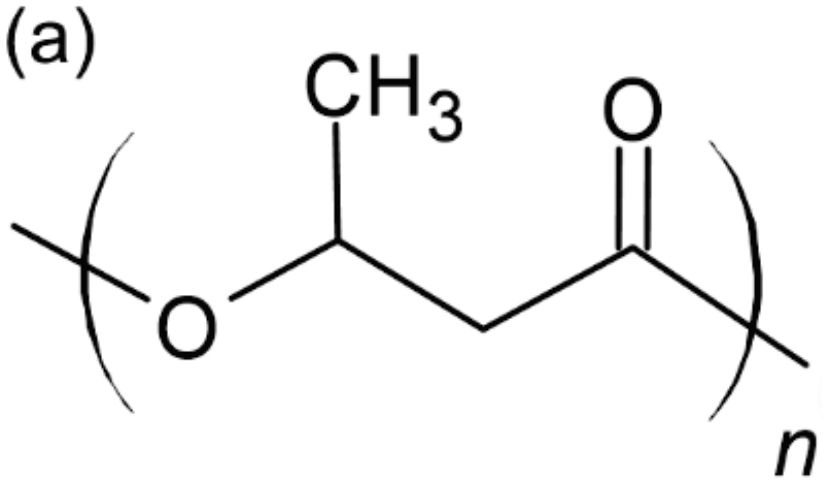

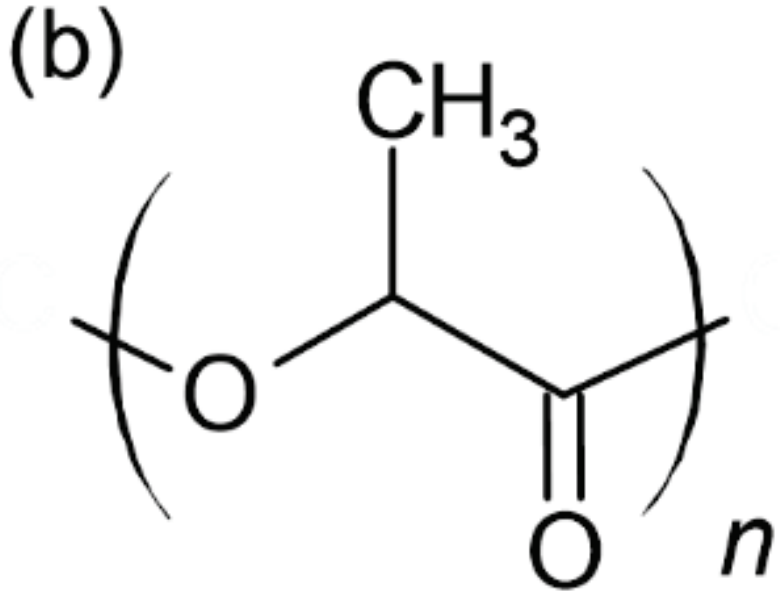

Figure 7.45 Chemical structures of (a) Poly(3-hydroxybutyrate) (PHB) and (b) Poly(L-lactide) (PLA). (Source [17])

7.2.2 The preparation of PHB/PLA blend

The process of polymer blend preparation is the same as that described in section 6.2.2 except the weight ratio of PHB to PLA changes from 50wt%/50wt% to 75wt%/25wt%. The process of isothermal melt crystallization is the same as that in section 6.2.4. [17]

7.2.3 In situ ATR-FTIR spectroscopic imaging

An Equinox 55 FTIR spectrometer (Bruker Corp.) with a MCT detector was used to measure the conventional ATR-FTIR spectra of pure PHB and PLA, separately. A Tensor 27 FTIR spectrometer (Bruker Corp.), as detailed in section 3.2, was applied to measure the ATR-FTIR spectroscopic images with a FPA detector. A spectral resolution of 4 cm^{-1} and 64 co-added scans were applied. The obtained spectroscopic images based on integrated absorbance reveal the changes in spatial distribution and concentration of each component. In terms of spectroscopic images based on the band position, the wavenumber of maximum absorbance

in the ν (C=O) band region of PHB and PLA for all of the pixels were collected through MATLAB. Spectroscopic images based on the band position, which can reveal the distribution of peak positions, were prepared with GraphR. A colour bar from red (high value) to blue (low value) is placed beside the spectroscopic images. The imaged area is ca. 0.6 × 0.55 mm^2 with a spatial resolution of ca. 10–12 μm. The size of PHB spherulites ranges from ten to hundreds of micrometres, which depends on the experiment conditions and molecular weights. [17,140,141]

7.3 Results and discussion

7.3.1 Phase separation and crystallization processes of PHB/PLA (75/25) blend monitored by spectroscopic images based on the band position

Figure 7.2 is the phase diagram of PHB/PLA blends ($M_{w,PHB}$ = 5,000 and $M_{w,PLA}$ = 50,000), which shows the critical temperature for phase separation and crystallization at different compositions. In this work, the PHB/PLA (75wt%/25wt%) blend with a higher concentration of PHB was chosen because the ν (C=O) band of crystalline PHB is more independent than that of crystalline PLA. Its critical temperature for phase separation and crystallization is less than or equal to 145 ˚C. [16,17]

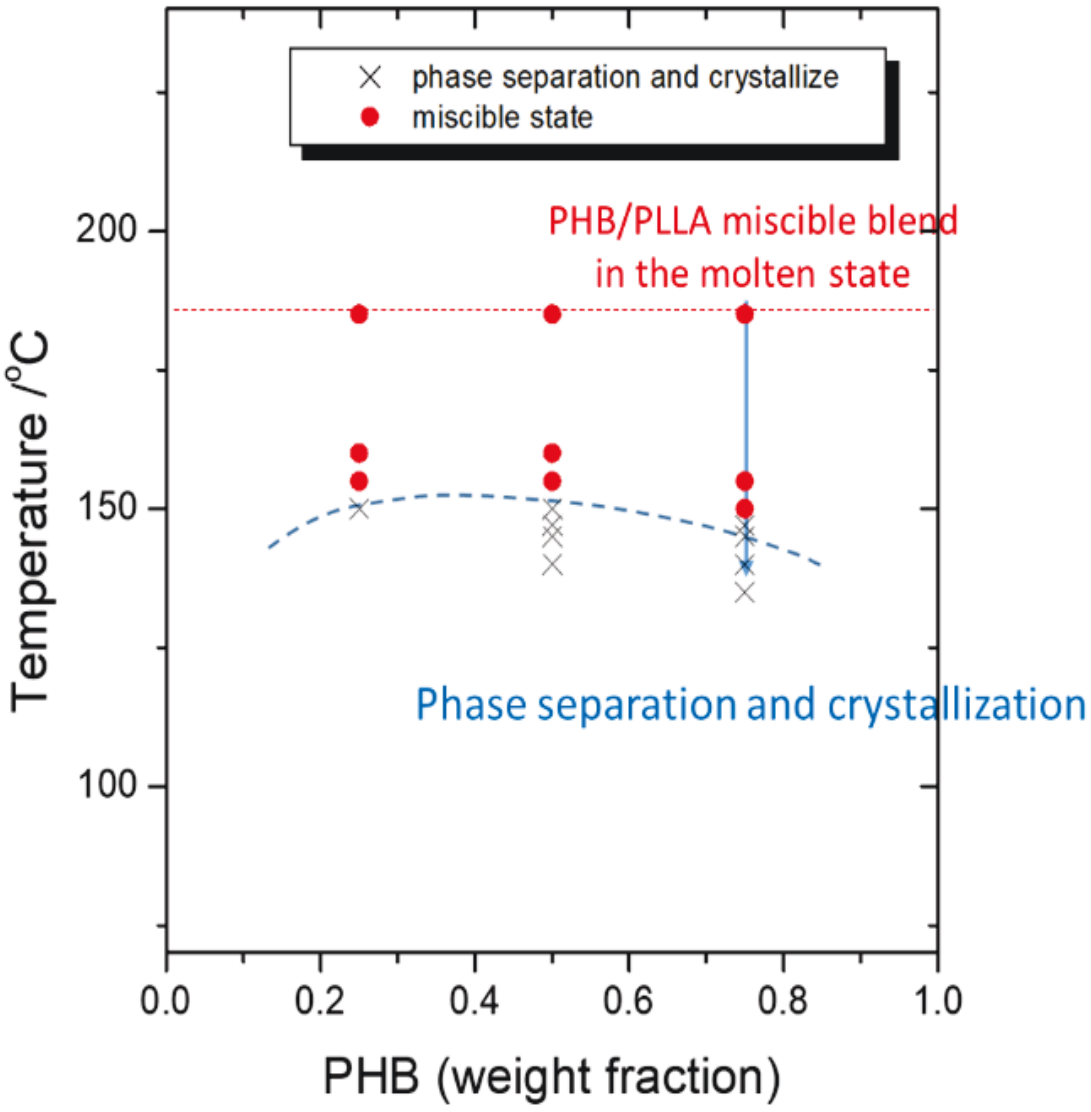

Figure 7.46 The phase diagram of PHB/PLA blends ($M_{w,PHB}$ = 5,000 and $M_{w,PLA}$ = 50,000). (Source [17])

Figure 7.3 is the time-dependent ATR-FTIR spectra in the ν (C=O) band region of PHB/PLA (75/25) blend during isothermal melt crystallization at 145 ˚C. There are three bands (1720, 1733, and 1756 cm^{-1}) in the ν (C=O) band region, which are assigned to C=O stretching modes of the crystalline PHB (PHB(C)), miscible PHB/PLA blend, and crystalline PLA (PLA(C)), respectively. It is assumed that amorphous PHB and PLA are intermolecularly

mixed in the miscible PHB/PLA blend. The absorbance of ν (C=O) band of crystalline PLA is low due to its low concentration and crystallinity. Thus, the research focus of this work is the ν (C=O) band of crystalline PHB. During phase separation and crystallization, the ν (C=O) band at 1733 cm^{-1} ascribed to the miscible state of PHB/PLA blend decreases and then shifts gradually as a function of time. Finally, it moves to 1720 cm^{-1}, which is the ν (C=O) band of crystalline PHB. As a result, the shift of band position indicates the changes of the status of ν (C=O) band during isothermal melt crystallization of PHB/PLA (75/25) blend as a function of time. [17]

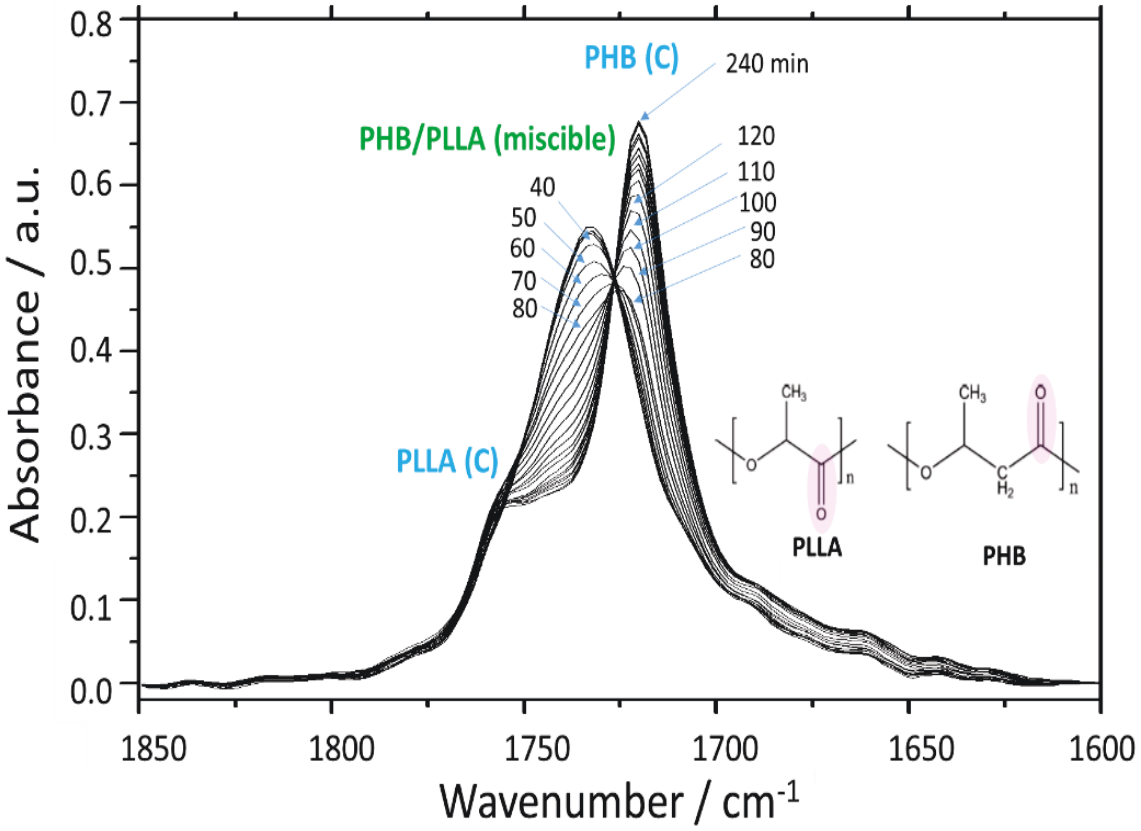

Figure 7.47 Time-dependent ATR-FTIR spectra of PHB/PLA (75/25) blend during isothermal melt crystallization at 145 ˚C. The ν (C=O) bands of crystalline PHB (PHB(C)), miscible PHB/PLA blend, and crystalline PLA (PLA(C)) are 1720, 1733, 1756 cm^{-1}, respectively. (Source [17])

In the previous study, the band position of ν (C=O) band does not shift during isothermal melt crystallization of pure PHB. [84] However, the shift of band position occurs in the ν (C=O) band during isothermal crystallization process of PHB/PLA blends. This reveals that the intermolecular interaction between PHB and PLA in the miscible state transfers to the inter- and intramolecular interaction within PHB crystal in the immiscible state. [16] Therefore, the previous study laid the basis for the application of ATR-FTIR spectroscopic images based on the band position as an effective method to visualize the changes in these inter- and intramolecular interactions during the isothermal melt crystallization of PHB/PLA blends. [17]

Figure 7.4 plots the peak position of the ν (C=O) band versus isothermal crystallization time in PHB/PLA (75/25) blends. It was found that no shift in the peak position occurs after 2 hours, while the increase of absorbance continues. It can be observed that the ν (C=O) band of crystalline PLA appears at 1756 cm^{-1} in the spectra. However, its low absorbance, as shown in figure 7.3, makes it difficult to analyse the peak shift from the miscible state to PLA crystalline state. Thus, the analysis of spectroscopic images based on the band position mainly relies on the ν (C=O) band of miscible PHB/PLA blend and crystalline PHB. The ν (C=O) band at 1733 cm^{-1} is assigned to the intermolecular interaction between PHB and PLA in the miscible state while the ν (C=O) band at 1720 cm^{-1} is assigned to the inter- and intramolecular interactions within the PHB crystal. [17]

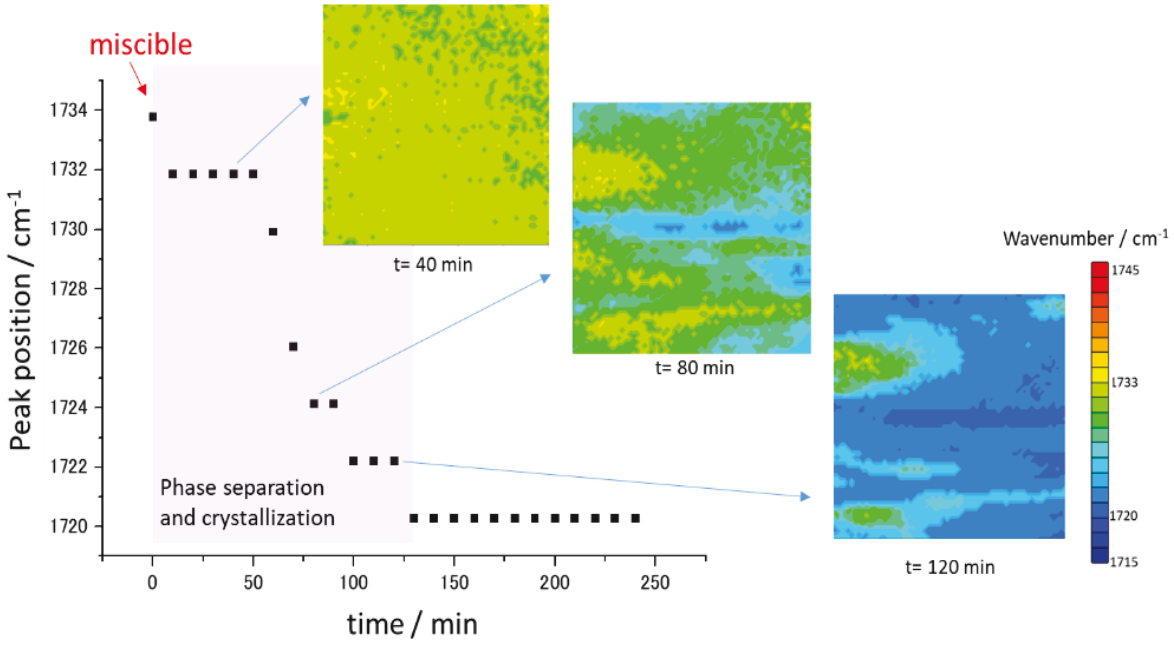

Figure 7.48 ATR-FTIR spectroscopic images generated by plotting the peak position of the ν (C=O) band for the PHB/PLA (75/25) blend during isothermal melt crystallization at 145 ˚C as a function of time. The size of each image is 0.6 mm × 0.55 mm. (Source [17]**)**

7.3.2 Spectroscopic images based on the band position of PHB/PLA (75/25) blends

Figure 7.5 shows time-dependent spectroscopic images based on ν (C=O) band position in the PHB/PLA (75/25) blend during isothermal melt crystallization at 145 ˚C. It shows the time-dependent band position shift of ν (C=O) band in each pixel. The range of wavenumber of all spectroscopic images is the same (maximum (red) is 1745 cm^{-1} and minimum (blue) is 1715 cm^{-1}). The obtained spectroscopic images reveal the spatial distribution of the peak position of the ν (C=O) band. In this work, we define the peak position as "the wavenumber of the band with the greatest absorbance". Soon after reaching the required isothermal crystallization temperature, the peak position of nearly all pixels remains at 1733 cm^{-1}, which reveals that the intermolecular interaction between PHB and PLA appears in the whole

polymer blend. After 60 minutes, the peak position of the pixels in the right side of imaged area becomes less than 1733 cm^{-1}, which indicates the break of the intermolecular interaction between PHB and PLA. After 120 minutes, the intermolecular interaction between PHB and PLA, indicated by yellow and yellow green in the spectroscopic images, disappears gradually. On the other hand, the inter- and intramolecular interaction within PHB crystal, indicated by blue in the spectroscopic images, start to occur in a larger area. [17]

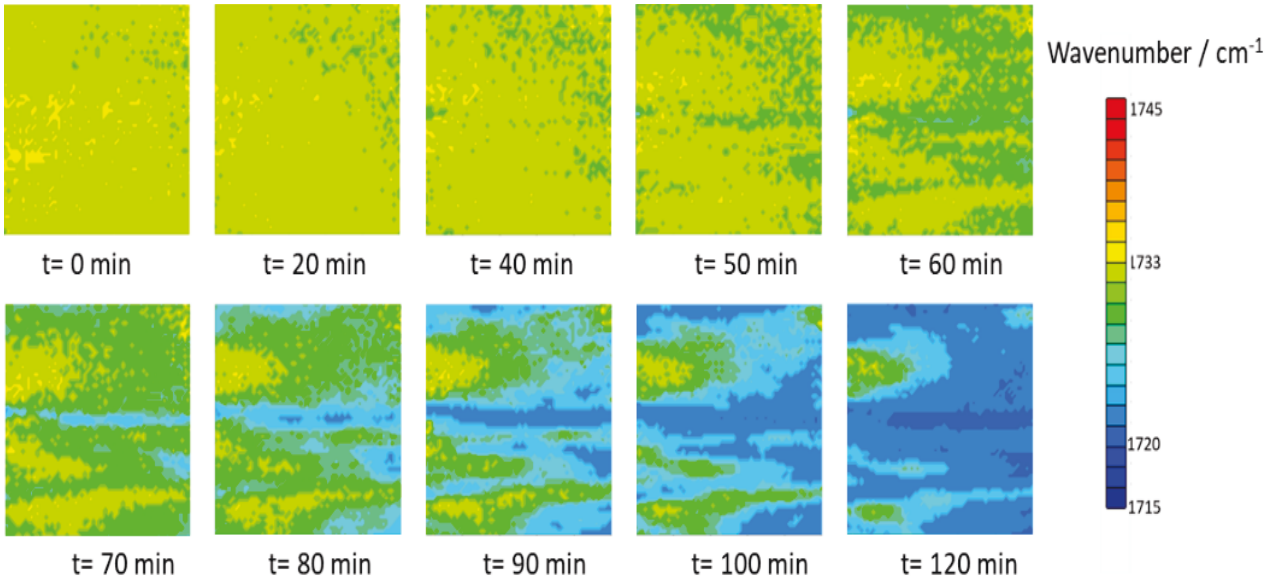

Figure 7.49 Spectroscopic images of the PHB/PLA (75/25) blend generated by plotting the peak position (from 1745 to 1715 cm^{-1}) of the ν (C=O) band during isothermal crystallization process at 145 ˚C as a function of time. The size of each image is 0.6 mm × 0.55 mm. (Source [17]**)**

Figure 7.6 shows the spectroscopic images based on integrated absorbance of PHB/PLA (75/25) blend during the isothermal crystallization process at 145 ˚C. It was observed that PHB and PLA are quite miscible in the polymer blend soon after temperature decreases, which is consistent with the corresponding spectroscopic images based on the band position: the intermolecular interaction between PHB and PLA appears in the whole polymer blend. After 120 mins, the spectroscopic images based on integrated absorbance indicate the occurrence of phase separation, which also agrees with the disappearance of intermolecular interaction between PHB and PLA indicated in the corresponding spectroscopic images based

on the band position. Moreover, crystalline PHB-rich domains (Figure 7.6 (120 min)) are in the same place where the inter- and intramolecular interactions within PHB crystal occur, as revealed in Figure 7.5 (120 min). These results demonstrate that the spectroscopic images based on the band position are consistent with the spectroscopic images based on integrated absorbance. [17]

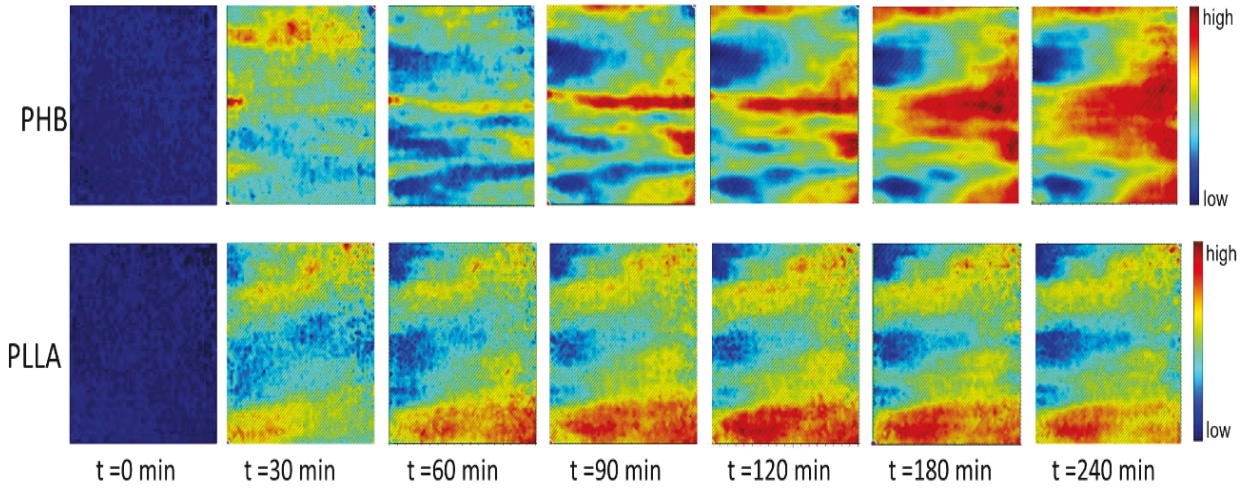

Figure 7.50 ATR-FTIR spectroscopic images of the PHB/PLA (75/25) blend as a function of time during the isothermal crystallization process at 145 ˚C. The images were prepared based on the distribution of integrated absorbance of the ν (C=O) band of PHB crystal (1730-1700 cm^{-1}, top) and that of PLA crystal (1762 -1753 cm^{-1}, bottom). The size of each image is 0.6 mm × 0.55 mm. (Source [17]**)**

Figure 7.7 shows the time-dependent absorbance change of the ν (C=O) band representing the miscible PHB/PLA blend and crystalline PHB, the peak position of ν (C=O) band of crystalline PHB, and the second derivatives intensity of ν (C=O) band of crystalline PLA. ν (C=O) band of crystalline PLA at 1756 cm^{-1} is obvious but its absorbance is weak because the concentration of PLA is low. Thus, the 2^{nd} derivative intensity of ν (C=O) band of crystalline PLA at 1756 cm^{-1} is plotted in Figure 7.7. [17]

After temperature decreases to 145 ˚C, as shown in figure 7.7, the absorbance of the ν (C=O) band at 1733 cm^{-1}, assigned to the miscible PHB/PLA blend, decreases gradually. Meanwhile,

the ν (C=O) band of crystalline PLA appears and the ν (C=O) band of miscible PHB/PLA blend starts to shift to 1720 cm^{-1}. After ca. 80 mins, the absorbance of ν (C=O) band of crystalline PHB at 1720 cm^{-1} starts to increase. Because of the low concentration of PLA in the PHB/PLA (75/25) blend, ν (C=O) band of crystalline PLA appears as a shoulder peak. The absorbance of ν (C=O) band of crystalline PHB starts to increase when the peak shift nearly completes. In this multicomponent polymer system, the molecular weight of PLA is larger than that of PHB. Moreover, the crystallization temperature of PLA (~160 ˚C) is also higher than that of PHB (~150 ˚C). Thus, during the isothermal melt crystallization process of PHB/PLA (75/25) blend at 145 ˚C, crystalline PLA appear first. [17]

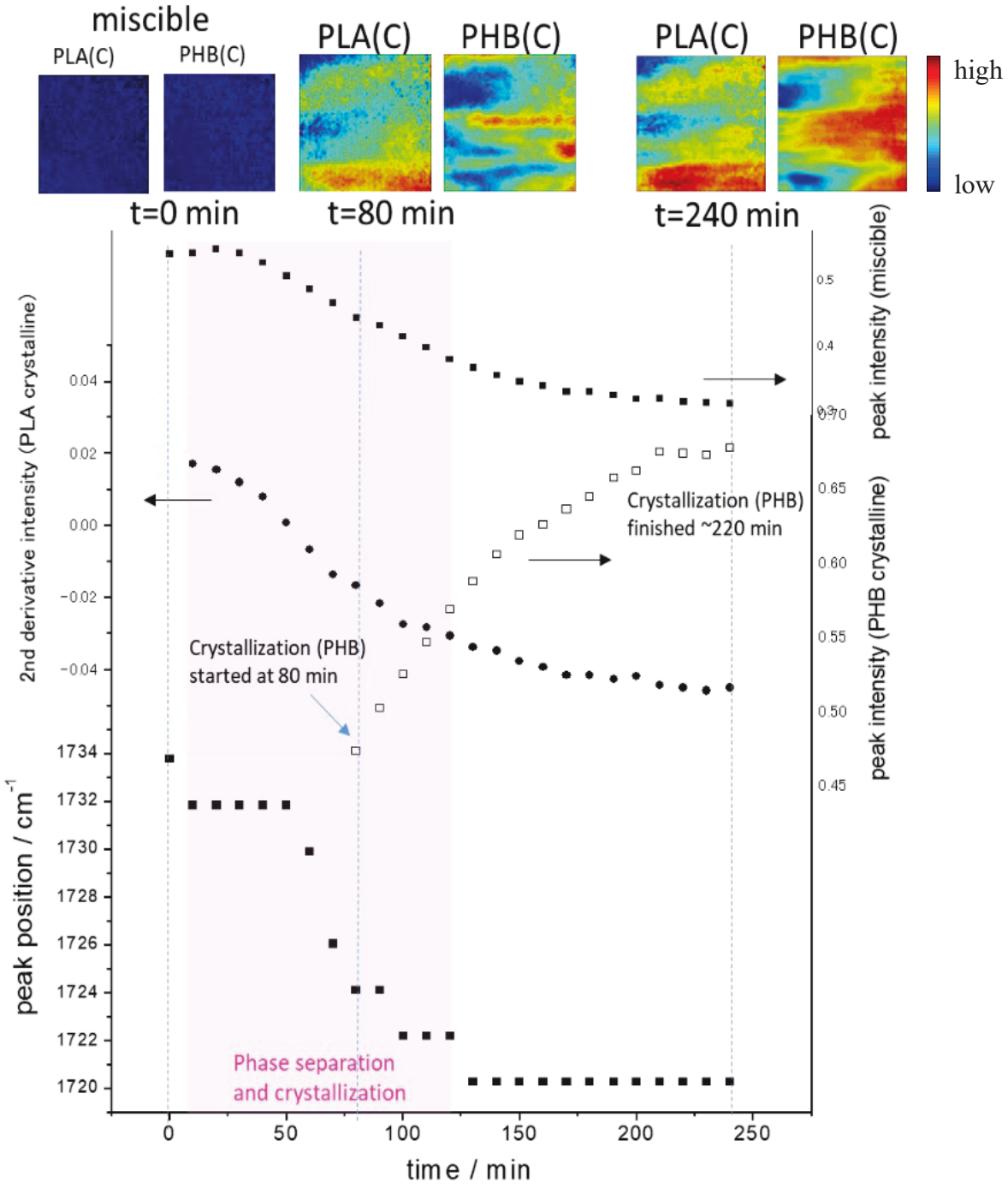

Figure 7.51 Time-dependent absorbance change of the ν (C=O) band assigned to the miscible PHB/PLA blend and crystalline PHB, second derivatives intensity of ν (C=O) band of crystalline PLA, and peak position of ν (C=O) band of crystalline PHB with spectroscopic images based on the integrated absorbance of the ν (C=O) band of crystalline PHB at 1730-1700 cm^{-1} region (PHB(C)) and that of crystalline PLA at 1762 -

1753 cm^{-1} region (PLA(C)) during the isothermal crystallization process at 145 ˚C. The size of each image is 0.6 mm × 0.55 mm. (Source [17]**)**

7.3.3 The comparison between spectroscopic images based on band position and those based on integrated absorbance of the same spectral band

In this chapter, spectroscopic images based on band position are compared with those based on integrated absorbance. As mentioned in section 7.3.2, these two types of spectroscopic images show a good correspondence during the isothermal melt crystallization of PHB/PLA blends. Figure 7.8 shows the time-dependent spectroscopic images based on the band position (Figure 7.8 (a)) and spectroscopic images based on integrated absorbance (Figure 7.8 (b) and (c)) in the ν (C=O) band region of PHB/PLA (75/25) blend during the isothermal melt crystallization. Comparing these two types of spectroscopic images, the green region of the spectroscopic image (Figure 7.8(a)) corresponds to the yellow and red regions of spectroscopic images (Figure 7.8 (b)) at 60 min. After 90 min, the blue region of spectroscopic images (Figure 7.8 (a)) corresponds to the red region of spectroscopic images (Figure 7.8 (b)). The appearance of blue regions shown in the spectroscopic images based on band position reveals the disappearance of intermolecular interactions between PHB and PLA. This observation agrees with the disappearance of the homogeneous region and the appearance of the red region, which is shown in the spectroscopic images based on the integrated absorbance. In the early stage of isothermal melt crystallization, the yellow and red region in the spectroscopic images based on the integrated absorbance of ν (C=O) band of crystalline PHB correspond to the light blue and blue region shown in the spectroscopic images based on band position, respectively. [17]

Compared with PHB/PLA (50wt%/50wt%) blends investigated in chapter 6, the morphology of PHB/PLA (75wt%/25wt%) blends after isothermal melt crystallization for 6 hours is slightly different. A 3D continuous phase: sea-island structure with crystalline PHB and crystalline PLA was observed in the spectroscopic image. [17]

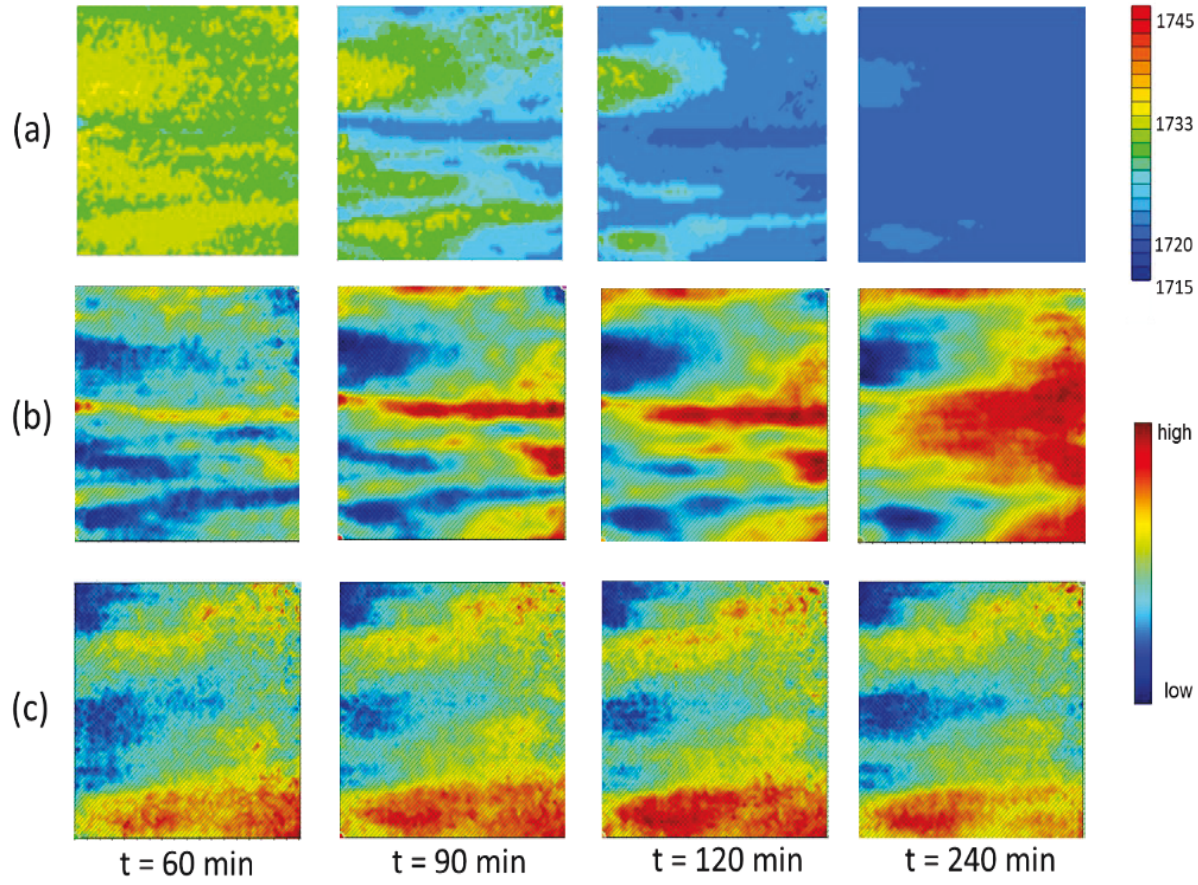

Figure 7.52 ATR-FTIR spectroscopic images of PHB/PLA (75/25) blends during the isothermal crystallization process at 145 ˚C as a function of time. The spectroscopic images based on the band position (a) and those based on the integrated absorbance were prepared by ν (C=O) band region between 1730 -1700 cm^{-1} for crystalline PHB (b) and that between 1762 -1753 cm^{-1} for crystalline PLA (c), respectively. The size of each image is 0.6 mm × 0.55 mm. (Source [17])

7.3.4 The feasibility of spectroscopic images based on the band position to investigate the isothermal melt crystallization of PHB/PLA blends at different temperatures

The isothermal melt crystallization of PHB/PLA blends at 140 ˚C was investigated in order to demonstrate that the spectroscopic images based on the band position are feasible to

investigate this type of process at different temperatures. Figure 7.9 shows the spectroscopic images based on the band position and spectroscopic images based on the integrated absorbance of the ν (C=O) band of crystalline PHB during isothermal melt crystallization in PHB/PLA blends at 140 ˚C. The disappearance of intermolecular interaction between PHB and PLA, indicated by fewer pixels with yellow and yellow green in the corresponding spectroscopic image based on the band position (figure 7.9 (a)). The appearance of the inter- and intramolecular interactions within PHB crystal, indicated by more pixels with blue colour in the spectroscopic images based on the band position (figure 7.9 (a)), was found to be consistent with the appearance of crystalline PHB-rich domains in the corresponding spectroscopic images based on the integrated absorbance (figure 7.9 (b)). These results demonstrate that spectroscopic images based on the band position and spectroscopic images based on the integrated absorbance show a good correspondence and can be applied to visualize the intra- and intermolecular interactions when investigating the isothermal melt crystallization at different temperatures. [17]

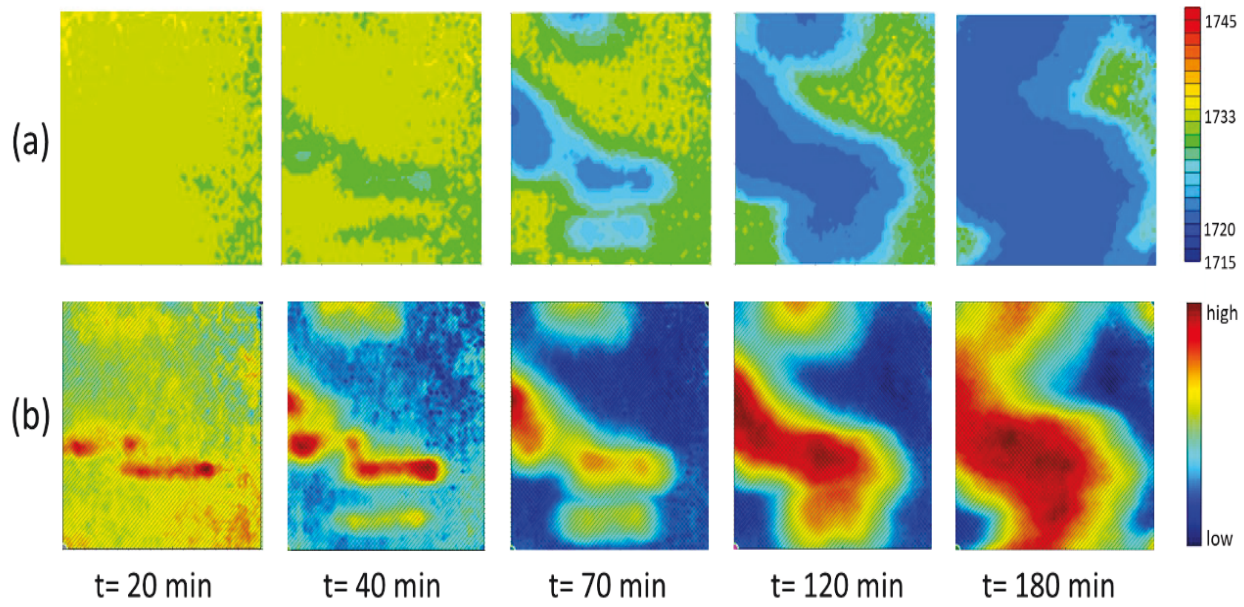

Figure 7.53 (a) ATR-FTIR spectroscopic images based on the peak position of the ν (C=O) band ; (b) ATR-FTIR spectroscopic images based on the integrated absorbance of the ν (C=O) band of crystalline PHB (1730-1700 cm^{-1}) during the isothermal melt

crystallization at 140 ˚C in the PHB/PLA (75/25) blend as a function of time. The size of each image is 0.6 mm × 0.55 mm. (Source [17]**)**

7.4 Conclusion

The inter- and intramolecular interactions occurring within polymer blends have great effect on their physical and chemical properties as well as their synthesis and processing. The conventional ATR-FTIR spectroscopic images based on integrated absorbance can reveal the distribution of different blend components but they cannot indicate the areas where the intermolecular interactions occur. Thus, a novel technique, the spectroscopic image based on the band position was introduced in this chapter in order to highlight these areas. The ν (C=O) band shift in the ATR-FTIR spectra during the isothermal melt crystallization indicates the change in intra- and intermolecular interactions in PHB/PLA blends. As a result, the spectroscopic images based on the band position were prepared in this chapter to visualize the distribution of different intra- and intermolecular interactions in PHB/PLA blends during the isothermal melt crystallization. The disappearance of intermolecular interactions between PHB and PLA, which is shown in the spectroscopic images based on band position, agrees with the disappearance of homogeneous region shown in the corresponding spectroscopic images based on the integrated absorbance. The appearance of the inter- and intramolecular interactions within PHB crystal, which is also shown in the spectroscopic images based on the band position, agrees with the appearance of crystalline PHB-rich domains in the corresponding spectroscopic images based on the integrated absorbance. This is the first time that the change of inter- and intramolecular interactions in the polymer blend has been visualized with the spectroscopic images based on the band position. Compared with the spectroscopic images based on the integrated absorbance, the direct observation of intermolecular interactions based on band shift can provide the specific information about the strength of interactions. This study proves that the spectroscopic images based on the band position can provide more information about the spatial distribution of different intra- and intermolecular interactions in the polymer blends and their changes induced by different perturbations, such as pressure, temperature, concentration and pH. [17]

Chapter Eight

Conclusion

8. Conclusion

8.1 Overall summary

1. The study of phase separation in LCST polymer blends under high-pressure CO_2 can provide an insight to their physical properties. Thus, this thesis first reports the study on visualization of the dynamic processes of phase separation in PCL/PLA blend under high-pressure CO_2 using in situ high-pressure ATR-FTIR spectroscopic imaging. The obtained ATR-FTIR spectroscopic images indicate that phase separation occurs in PCL/PLA blends with increasing temperature or under high-pressure CO_2. The change in the morphology of PCL/PLA blends, revealed by the ATR-FTIR spectroscopic images, can be applied to compare the extent of phase separation in this blend under different conditions. From this work, it is found that the extent of phase separation in PCL/PLA blends under high-pressure CO_2 is enhanced with increasing exposure time, CO_2 pressure and temperature. Finally, it was found that phase separation in this blend under high-pressure CO_2 is spinodal decomposition process before the equilibrium and nucleation & growth process after the equilibrium reached. This pioneering methodology opens possibilities to visualize the process of phase separation in LCST polymer blends. [9]

2. Exposing polymers to high-pressure CO_2 benefits polymer processing. As a result, ATR-FTIR spectroscopic images of PCL/PLA blends with or without high-pressure CO_2 were analysed using 2D correlation analysis and 2D disrelation mapping. The relatively weak dipole-dipole inter- and intramolecular interactions between polymer molecules were studied through 2D disrelation maps for the first time. With the specially designed PCL/PLA interface, the interactions between the same type of polymer molecules and different types of polymer molecules were distinguished. Under high-pressure CO_2, the number of all these three types of interactions: interaction between PCL and PLA, interaction between PCL and PCL as well as interaction between PLA and PLA decreases compared with that in the PCL/PLA interface before exposure to high-pressure CO_2. The induced increase in the Flory interaction parameter is the main reason for the occurrence of phase separation in the PCL/PLA blend under exposure to high-pressure CO_2, as described above. The findings of this work will benefit polymer processing with high-pressure and supercritical CO_2. [15]

3. The investigation of phase separation and crystallization in biopolymer blends is an important aspect of biopolymer processing. In this thesis, ATR-FTIR spectroscopic imaging was applied to visualize the process of crystallization and phase separation of PHB/PLA blends simultaneously in situ. The peak shift of the ν(C=O) band of PHB during the isothermal crystallization process indicated a transformation of the intermolecular interaction between PHB and PLA in the miscible state to the inter- and intramolecular interactions between PHBs in the immiscible state. The whole dynamic process of phase separation can be revealed by the appearance and gradual separation of crystalline PHB-rich domains and crystalline PLA-rich domains in the obtained ATR-FTIR spectroscopic images. As the isothermal melt crystallization progresses, the larger size of crystalline polymer-rich domains and the increasing integrated absorbance of the ν(C=O) band of crystalline polymers both indicate the increasing crystallinity in the polymer blend, which agrees with the isothermal crystallization process of pure polymers. It was also found that increasing isothermal crystallization temperature can enhance the extent of phase separation between crystalline PHB-rich domains and crystalline PLA-rich domains. It is because the process of crystallization slows down with higher annealing temperature, which leaves more time for phase separation. Crystallinity in PHB/PLA blends decreases with increasing isothermal crystallization temperature, which also agrees with that of pure polymers. At last, a new proposal for the mechanism of phase separation and crystallization in the UCST polymer blend system was discussed. It can be concluded that reducing the annealing temperature is an effective way to restrict the phase separation and thus control the final morphology in the UCST crystallizable polymer blends. [16]

4. The inter- and intramolecular interactions occurring within polymer blends have great effect on their physical and chemical properties as well as their synthesis and processing. [80] In this project, spectroscopic images were produced through plotting the peak position of a spectral band from the datasets generated by in-situ ATR-FTIR spectroscopic imaging. This method has been successfully applied to visualize changes in intra- and intermolecular interactions in PHB/PLA blends during the isothermal melt crystallization. This is because the peak position of ν (C=O) band can reflect the intra- and intermolecular interactions in PHB/PLA blends. The disappearance of intermolecular interactions between PHB and PLA and the appearance of the inter- and intramolecular interactions within PHB crystal were both visualized using the spectroscopic images based on the band position. This work shows the potential of spectroscopic images based on the band position to visualize different types of

intra- and intermolecular interactions between polymer molecules or between polymer and other additives in various types of multicomponent polymer systems. [17]

This thesis summarises the application of FTIR spectroscopy and spectroscopic imaging for the analysis of different polymer systems during my whole PhD study. The FTIR spectroscopic approaches developed in this project are suitable for the study of other homopolymers and multicomponent polymer systems. The application of spectroscopic techniques in polymer research is by no means exhausted and many emerging research fields exist to develop novel applications. A more thorough understanding of many types of polymer systems can reveal a wealth of information about polymer processing applications, such as drying, impregnation, extraction, blending and dyeing, both with or without high-pressure CO_2. The knowledge gained from these systems utilising lab-sized experiments can be applied on a larger scale, such as design novel processing routes.

8.2 Recommendations for future work

The main objective of this thesis is to demonstrate further the use of ATR-FTIR spectroscopy and ATR-FTIR spectroscopic imaging as a valuable analytical approach to investigate biopolymers and multicomponent biopolymer system. This research can also serve as the useful platform for the future development in this field. Investigation of the morphology, interaction and crystallization of biopolymers and multicomponent biopolymer system with and without high-pressure CO_2 can aid the design of biopolymer products and biopolymer process, which can establish the ATR-FTIR spectroscopy and spectroscopic imaging as a reliable technique for industrial applications.

Exciting opportunities exist for further investigation based on this work. Some recommendations for a continuation of the research described in this thesis are outlined in the following points.

1. ATR-FTIR spectroscopic imaging can be used to visualize phase separation in other LSCT polymer blend systems apart from PCL/PLA blends and interdiffusion in UCST polymer blends such as PHB/PLA blends.

2. Two different exploratory approaches could be used for the future research of the morphology and crystallization of biopolymers and multicomponent biopolymer system with and without high-pressure CO_2. One is a 'depth' based study. Biopolymers with different chain structure (grafted, network, hyperbranched and so on), polymer isomerism (sequence isomerism, stereoisomerism and structural isomerism), strength of Lewis base functional groups (soft and hard), degree of crosslinking and degree of branching can be investigated. The other one is a "breadth" based study. The effect of external stress, dispersant (making the distribution of polymers more evenly in supercritical fluids), modifier (enhancing the solubility of polymer in high-pressure CO_2) and treatment time during polymer processing on biopolymers and multicomponent biopolymer system under high-pressure and supercritical CO_2 can be explored.

3. The application of ATR-FTIR spectroscopy to study unsaturated polyketone with different concentration of carbonyl groups under high-pressure CO_2 represents an exciting new use for this technology. [28] However, some advancements could be made to further this study. For instance, polyketone/polyethylene glycol (PEG) blends under high-pressure CO_2 can be investigated. The hydroxyl-carbonyl, carbonyl-carbonyl and carbonyl-CO_2 interactions need to distinguish by preparing polyketone/PEG interfaces. The swelling and CO_2 sorption of this blend with different compositions can be investigated and compared with those of pure polyketone. The main challenge of this investigation is that polyketone is difficult to mix homogeneously with PEG so that the weight ratio of polyketone to PEG is not exactly 50:50 in the polymer blend sample, which affects the obtained results.

4. Finally, the use of ATR-FTIR spectroscopy and spectroscopic imaging with other analytical methods can aid this study. Comparing the obtained results from this work with other established analytical approaches, such as X-ray diffraction (XRD), differential scanning calorimetry (DSC) and so on, can provide more valuable information to supplement and improve this work.

Reference

[1] D. Marlina, H. Sato, H. Hoshina, Y. Ozaki, Intermolecular interactions of poly(3-hydroxybutyrate-co-3-hydroxyvalerate) (P(HB-co-HV)) with PHB-type crystal structure and PHV-type crystal structure studied by low-frequency Raman and terahertz spectroscopy, Polymer (Guildf). 135 (2018) 331–337. doi:10.1016/j.polymer.2017.12.030.

[2] S.F. Chou, K.A. Woodrow, Relationships between mechanical properties and drug release from electrospun fibers of PCL and PLGA blends, J. Mech. Behav. Biomed. Mater. 65 (2017) 724–733. doi:10.1016/j.jmbbm.2016.09.004.

[3] S. Türkkan, A.E. Pazarçeviren, D. Keskin, N.E. Machin, Ö. Duygulu, A. Tezcaner, Nanosized CaP-silk fibroin-PCL-PEG-PCL/PCL based bilayer membranes for guided bone regeneration, Mater. Sci. Eng. C. 80 (2017) 484–493. doi:10.1016/j.msec.2017.06.016.

[4] S. Milovanovic, G. Hollermann, C. Errenst, J. Pajnik, S. Frerich, S. Kroll, K. Rezwan, J. Ivanovic, Supercritical CO_2 impregnation of PLA/PCL films with natural substances for bacterial growth control in food packaging, Food Res. Int. 107 (2018) 486–495. doi:10.1016/j.foodres.2018.02.065.

[5] Q. Guo, Polymer morphology: principles, characterization, and processing, John Wiley & Sons, 2016.

[6] C. Vogel, E. Wessel, H.W. Siesler, FT-IR Imaging Spectroscopy of Phase Separation in Blends of Poly (3-hydroxybutyrate) with Poly (L -lactic acid) and Poly (E -caprolactone), Biomacromolecules. 9 (2008) 523–527.

[7] O.S. Fleming, Application of Advanced Vibrational Spectroscopy to Polymers Processed with Supercritical CO_2, PhD Thesis, Imperial College London, 2006.

[8] T.A. Walker, D.J. Frankowski, R.J. Spontak, Thermodynamics and kinetic processes of polymer blends and block copolymers in the presence of pressurized carbon dioxide, Adv. Mater. 20 (2008) 879–898. doi:10.1002/adma.200700076.

[9] H. Lu, S.G. Kazarian, How Does High-Pressure CO_2 Affect The Morphology of PCL/PLA Blends? Visualization of Phase Separation using In Situ ATR-FTIR

Spectroscopic Imaging, Spectrochim. Acta Part A Mol. Biomol. Spectrosc. 243 (2020) 118760. doi:10.1016/j.saa.2020.118760.

[10] S.G. Kazarian, Polymers and supercritical fluids: Opportunities for vibrational spectroscopy, Macromol. Symp. 184 (2002) 215–228. doi:10.1002/1521-3900(200208)184:1<215::AID-MASY215>3.0.CO;2-X.

[11] O.S. Fleming, S.G. Kazarian, Polymer Processing with Supercritical Fluids, Supercrit. Carbon Dioxide Polym. React. Eng. (2006) 205–238. doi:10.1002/3527606726.ch10.

[12] S.G. Kazarian, K.L.A. Chan, FTIR Imaging of Polymeric Materials under High-Pressure Carbon Dioxide, Macromolecules. 37 (2004) 579–584. doi:10.1021/ma035420y.

[13] A. V. Ewing, S.G. Kazarian, Current trends and opportunities for the applications of in situ vibrational spectroscopy to investigate the supercritical fluid processing of polymers, J. Supercrit. Fluids. 134 (2018) 88–95. doi:10.1016/j.supflu.2017.12.011.

[14] A.A. Gabrienko, A. V. Ewing, A.M. Chibiryaev, A.M. Agafontsev, K.A. Dubkov, S.G. Kazarian, New insights into the mechanism of interaction between CO_2 and polymers from thermodynamic parameters obtained by in situ ATR-FTIR spectroscopy, Phys. Chem. Chem. Phys. 18 (2016) 6465–6475. doi:10.1039/c5cp06431g.

[15] H. Lu, H. Shinzawa, S.G. Kazarian, Intermolecular Interactions in the Polymer Blends Under High-Pressure CO_2 Studied Using Two-Dimensional Correlation Analysis and Two-Dimensional Disrelation Mapping, Appl. Spectrosc. 75 (2021) 250–258. doi:10.1177/0003702820978473.

[16] H. Lu, S.G. Kazarian, H. Sato, Simultaneous Visualization of Phase Separation and Crystallization in PHB / PLLA Blends with In Situ ATR-FTIR Spectroscopic Imaging, Macromolecules. 53 (2020) 9074–9085. doi:10.1021/acs.macromol.0c00713.

[17] H. Lu, H. Sato, S.G. Kazarian, Visualization of Inter- and Intramolecular Interactions in Poly(3-hydroxybutyrate)/Poly(L-lactic acid) (PHB/PLLA) Blends During Isothermal Melt Crystallization Using Attenuated Reflection Fourier Transform infrared (ATR FT-IR) Spectroscopic Imaging, Appl. Spectrosc. 75 (2021) 979–986. doi:10.1177/00037028211010216.

[18] M. Poliakoff, S.M. Howdle, S.G. Kazarian, Vibrational Spectroscopy in Supercritical Fluids: From Analysis and Hydrogen Bonding to Polymers and Synthesis, Angew. Chemie. 34 (1995) 1275–1295. doi:10.1002/chin.199539328.

[19] E. Grotheer, C. Vogel, O. Kolomiets, U. Hoffmann, M. Unger, H.W. Siesler, FT-IR and NIR Spectroscopic Imaging: Principles, Practical Aspects, and Applications in Material and Pharmaceutical Science., in: R. Salzer, H.W. Siesler (Eds.), Infrared Raman Spectrosc. Imaging, Wiley-VCH, 2014.

[20] J. Zhang, H. Tsuji, I. Noda, Y. Ozaki, Structural changes and crystallization dynamics of poly(L-lactide) during the cold-crystallization process investigated by infrared and two-dimensional infrared correlation spectroscopy, Macromolecules. 37 (2004) 6433–6439. doi:10.1021/ma049288t.

[21] J.A. Dougan, K.L. Chan, S.G. Kazarian, FT-IR Imaging in ATR and Transmission Modes: Practical Considerations and Emerging Applications, in: R. Salzer, H.W. Siesler (Eds.), Infrared Raman Spectrosc. Imaging, Wiley-VCH, 2014.

[22] S. Li, T. He, X. Liao, Q. Yang, G. Li, Structural changes and crystallization kinetics of polylactide under CO_2 investigated using high-pressure Fourier transform infrared spectroscopy, Polym. Int. 64 (2015) 1762–1769. doi:10.1002/pi.4977.

[23] S.G. Kazarian, N.H. Brantley, C.A. Eckert, Applications of vibrational spectroscopy to characterize poly(ethylene terephthalate) processed with supercritical CO_2, Vib. Spectrosc. 19 (1999) 277–283. doi:10.1016/S0924-2031(98)00073-3.

[24] M. Schneider, P. Demoulin, R. Sussmann, J. Notholt, Fourier transform infrared spectrometry, in: N. Kämpfer (Ed.), Monit. Atmos. Water Vap., Springer, New York, 2013: pp. 95–111. doi:https://doi.org/10.1007/978-1-4614-3909-7_6.

[25] H. Hifumi, A. V. Ewing, S.G. Kazarian, ATR-FTIR spectroscopic imaging to study the drying and dissolution of pharmaceutical polymer-based films, Int. J. Pharm. 515 (2016) 57–68. doi:10.1016/j.ijpharm.2016.09.085.

[26] R. Salzer, HW Siesler, eds., Infrared and Raman Spectroscopic Imaging, Wiley, 2014.

[27] N.M.B. Flichy, S.G. Kazarian, C.J. Lawrence, B.J. Briscoe, An ATR - IR Study of Poly (Dimethylsiloxane) under High-Pressure Carbon Dioxide : Simultaneous Measurement of Sorption and Swelling, J. Phys. Chem. B. (2002) 754–759.

[28] A. V. Ewing, A.A. Gabrienko, S. V. Semikolenov, K.A. Dubkov, S.G. Kazarian, How do intermolecular interactions affect swelling of polyketones with a differing number of carbonyl groups? an in situ ATR-FTIR spectroscopic study of CO_2 sorption in polymers, J. Phys. Chem. C. 119 (2015) 431–440. doi:10.1021/jp510208e.

[29] A. V. Ewing, S.G. Kazarian, Recent advances in the applications of vibrational spectroscopic imaging and mapping to pharmaceutical formulations, Spectrochim. Acta - Part A Mol. Biomol. Spectrosc. 197 (2018) 10–29. doi:10.1016/j.saa.2017.12.055.

[30] A. Sroka-Bartnicka, L. Borkowski, G. Ginalska, A. Ślósarczyk, S.G. Kazarian, Structural transformation of synthetic hydroxyapatite under simulated in vivo conditions studied with ATR-FTIR spectroscopic imaging, Spectrochim. Acta Part A Mol. Biomol. Spectrosc. 171 (2017) 155–161. doi:10.1016/j.saa.2016.07.051.

[31] H. Tiernan, B. Byrne, S.G. Kazarian, Insight into Heterogeneous Distribution of Protein Aggregates at the Surface Layer Using Attenuated Total Reflection-Fourier Transform Infrared Spectroscopic Imaging, Anal. Chem. 92 (2020) 4760–4764. doi:10.1021/acs.analchem.0c00250.

[32] H. Tiernan, B. Byrne, S.G. Kazarian, ATR-FTIR spectroscopy and spectroscopic imaging for the analysis of biopharmaceuticals, Spectrochim. Acta - Part A Mol. Biomol. Spectrosc. 241 (2020) 118636. doi:10.1016/j.saa.2020.118636.

[33] E. V Solovyeva, H. Lu, G.A. Khripoun, K.N. Mikhelson, S.G. Kazarian, In situ ATR-FTIR spectroscopic imaging of PVC , plasticizer and water in solvent-polymeric ion-selective membrane containing Cd 2 + -selective neutral ionophore, J. Memb. Sci. 619 (2021) 118798. doi:10.1016/j.memsci.2020.118798.

[34] C.L. Song, S.G. Kazarian, Three-dimensional depth profiling of prostate tissue by micro ATR-FTIR spectroscopic imaging with variable angles of incidence, Analyst. 144 (2019) 2954–2964. doi:10.1039/c8an01929k.

[35] A.A. Gabrienko, C.H. Lai, S.G. Kazarian, In situ chemical imaging of asphaltene precipitation from crude oil induced by n -heptane, Energy and Fuels. 28 (2014) 964–971. doi:10.1021/ef402255c.

[36] A. V. Ewing, S.G. Kazarian, Infrared spectroscopy and spectroscopic imaging in forensic science, Analyst. 142 (2017) 257–272. doi:10.1039/c6an02244h.

[37] S.R. Falsafi, H. Rostamabadi, E. Assadpour, S.M. Jafari, Morphology and microstructural analysis of bioactive-loaded micro/nanocarriers via microscopy techniques; CLSM/SEM/TEM/AFM, Adv. Colloid Interface Sci. 280 (2020). doi:10.1016/j.cis.2020.102166.

[38] S.G. Kazarian, C.J. Lawrence, B.J. Briscoe, In-situ spectroscopy of polymers processed with supercritical carbon dioxide, New Trends At. Mol. Spectrosc. 4060 (1999) 210. doi:10.1117/12.375295.

[39] S.G. Kazarian, P.S. Wray, Applications of FTIR Spectroscopic Imaging in Pharmaceutical Science, in: S. Sasic, Y. Ozaki (Eds.), Raman, Infrared, near-Infrared Chem. Imaging, John Wiley & Sons, Inc, 2010: pp. 185–204.

[40] I. Noda, Generalized Two-Dimensional Correlation Spectroscopy, in: Front. Mol. Spectrosc., 2009: pp. 367–381.

[41] P. Lasch, I. Noda, Two-Dimensional Correlation Spectroscopy (2D-COS) for Analysis of Spatially Resolved Vibrational Spectra, Appl. Spectrosc. 73 (2019) 359–379. doi:10.1177/0003702818819880.

[42] Y. Park, S. Jin, E. Park, M. Hwang, I. Noda, B. Chea, Y.M. Jung, Chemical images and 2D-COS analysis of spin-coated PHBHx/PEG blend films, J. Mol. Struct. 1216 (2020) 128344. doi:10.1016/j.molstruc.2020.128344.

[43] H. Shinzawa, K. Awa, T. Okumura, S. Morita, M. Otsuka, Y. Ozaki, H. Sato, Raman imaging analysis of pharmaceutical tablets by two-dimensional (2D) correlation spectroscopy, Vib. Spectrosc. 51 (2009) 125–131. doi:10.1016/j.vibspec.2008.11.011.

[44] Y. Park, S. Jin, I. Noda, Y.M. Jung, Emerging developments in two-dimensional correlation spectroscopy (2D-COS), J. Mol. Struct. 1217 (2020) 128405. doi:10.1016/j.molstruc.2020.128405.

[45] X. Li, Y. Zeng, G. Deng, Y. Xu, Y. Ozaki, I. Noda, J. Wu, A Novel Approach Based on Two-Dimensional Correlation Spectroscopy to Determine the Stoichiometric Ratio of Two Substances Involved in Intermolecular Interactions, Appl. Spectrosc. 73 (2019) 1051–1060. doi:10.1177/0003702819841625.

[46] H. Shinzawa, J. Mizukado, S.G. Kazarian, Fourier Transform Infrared (FT-IR) Spectroscopic Imaging Analysis of Partially Miscible PMMA–PEG Blends Using Two-Dimensional Disrelation Mapping, Appl. Spectrosc. 71 (2017) 1189–1197. doi:10.1177/0003702816670917.

[47] M.A. Czarnecki, Two-Dimensional Correlation Spectroscopy: The Power of Power Spectra, Appl. Spectrosc. 74 (2020) 894–899. doi:10.1177/0003702820931156.

[48] J. Hniopek, M. Schmitt, J. Popp, T. Bocklitz, PC 2D-COS: A Principal Component Base Approach to Two-Dimensional Correlation Spectroscopy, Appl. Spectrosc. 74 (2020) 460–472. doi:10.1177/0003702819891194.

[49] R. Watanabe, A. Sugahara, H. Hagihara, J. Mizukado, H. Shinzawa, Molecular-Scale Deformation of Polypropylene/Silica Composites Probed by Rheo-Optical Fourier-Transform Infrared (FTIR) Imaging Analysis Combined with Disrelation Mapping, Anal. Chem. (2020). doi:10.1021/acs.analchem.0c00623.

[50] I. Noda, Generalized Two-Dimensional Correlation Method Applicable to Infrared, Raman, and Other Types of Spectroscopy, Appl. Spectrosc. 47 (1993) 1329–1336. doi:10.1366/0003702934067694.

[51] J.S. Chiou, J.W. Barlow, D.R. Paul, Polymer Crystallization Induced by Sorption of C02 Gas, J. Appl. Polym. Sci. 30 (1985) 3911–3924.

[52] E. Beckman, R.S. Porter, Crystallization of bisphenol a polycarbonate induced by supercritical carbon dioxide, J. Polym. Sci. Part B Polym. Phys. 25 (1987) 1511–1517. doi:10.1002/polb.1987.090250713.

[53] I. Pasquali, J.M. Andanson, S.G. Kazarian, R. Bettini, Measurement of CO_2 sorption and PEG 1500 swelling by ATR-IR spectroscopy, J. Supercrit. Fluids. 45 (2008) 384–390. doi:10.1016/j.supflu.2008.01.015.

[54] A. V. Ewing, S.G. Kazarian, Interaction of supercritical carbon dioxide with polymers studied by vibrational spectroscopy, in: Supercrit. Fluid Nanotechnol. Adv. Appl. Compos. Hybrid Nanomater., 2015: pp. 481–516. doi:10.1201/b19242.

[55] S.G. Kazarian, N.H. Brantley, B.L. West, M.F. Vincent, C.A. Eckert, In situ spectroscopy of polymers subjected to supercritical CO_2: Plasticization and dye impregnation, Appl. Spectrosc. 51 (1997) 491–494. doi:10.1366/0003702971940765.

[56] P.W. Labuschagne, S.G. Kazarian, R.E. Sadiku, In situ FTIR spectroscopic study of the effect of CO_2 sorption on H-bonding in PEG-PVP mixtures, Spectrochim. Acta - Part A Mol. Biomol. Spectrosc. 78 (2011) 1500–1506. doi:10.1016/j.saa.2011.01.040.

[57] Y.P. Handa, Z. Zhang, B. Wong, Effect of compressed CO_2 on phase transitions and polymorphism in syndiotactic polystyrene, Macromolecules. 30 (1997) 8499–8504. doi:10.1021/ma9712209.

[58] P.G. Parzuchowski, J. Gregorowicz, E.P. Wawrzyńska, D. Wiącek, G. Rokicki, The phase behavior in supercritical carbon dioxide of hyperbranched copolymers with architectural variations, J. Supercrit. Fluids. 107 (2016) 657–668. doi:10.1016/j.supflu.2015.07.028.

[59] S. Li, T. Chen, X. Liao, W. Han, Z. Yan, J. Li, G. Li, Effect of Macromolecular Chain Movement and the Interchain Interaction on Crystalline Nucleation and Spherulite Growth of Polylactic Acid under High-Pressure CO_2, Macromolecules. 53 (2020) 312–322. doi:10.1021/acs.macromol.9b01601.

[60] S.G. Kazarian, M.F. Vincent, F. V. Bright, C.L. Liotta, C.A. Eckert, Specific intermolecular interaction of carbon dioxide with polymers, J. Am. Chem. Soc. 118 (1996) 1729–1736. doi:10.1021/ja950416q.

[61] S.G. Kazarian, Polymer Processing with Supercritical Fluids, Polym. Sci. Ser. C. 42 (2000) 78–101.

[62] M. Takada, S. Hasegawa, M. Ohshima, Crystallization kinetics of poly(L-lactide) in contact with pressurized CO_2, Polym. Eng. Sci. 44 (2004) 186–196. doi:10.1002/pen.20017.

[63] M. Takada, M. Tanigaki, M. Ohshima, Effects of CO_2 on crystallization kinetics of polypropylene, Polym. Eng. Sci. 41 (2001) 1938–1946. doi:10.1002/pen.10890.

[64] K. Mizoguchi, T. Hirose, Y. Naito, Y. Kamiya, CO_2-induced crystallization of poly(ethylene terephthalate), Polymer (Guildf). 28 (1987) 1298–1302.

[65] F. Sampedro, A. McAloon, W. Yee, X. Fan, D.J. Geveke, Cost Analysis and Environmental Impact of Pulsed Electric Fields and High Pressure Processing in Comparison with Thermal Pasteurization, Food Bioprocess Technol. 7 (2014) 1928–1937. doi:10.1007/s11947-014-1298-6.

[66] E. Blümm, A.J. Owen, Miscibility, crystallization and melting of poly(3-hydroxybutyrate)/ poly(l-lactide) blends, Polymer (Guildf). 36 (1995) 4077–4081. doi:10.1016/0032-3861(95)90987-D.

[67] I. Noda, M.M. Satkowski, A.E. Dowrey, C. Marcott, Polymer alloys of nodax copolymers and poly(lactic acid), Macromol. Biosci. 4 (2004) 269–275. doi:10.1002/mabi.200300093.

[68] N. Koyama, Y. Doi, Miscibility of binary blends of poly[(R)-3-hydroxybutyric acid] and poly[(S)-lactic acid], Polymer (Guildf). 38 (1997) 1589–1593. doi:10.1016/S0032-3861(96)00685-4.

[69] W.T. Chuang, U.S. Jeng, P. Da Hong, H.S. Sheu, Y.H. Lai, K.S. Shih, Dynamic interplay between phase separation and crystallization in a poly(ε-caprolactone)/poly(ethylene glycol) oligomer blend, Polymer (Guildf). 48 (2007) 2919–2927. doi:10.1016/j.polymer.2007.03.041.

[70] S.J. Mumby, P. Sher, B.E. Eichinger, Phase diagrams of quasi-binary polymer solutions and blends, Polymer (Guildf). 34 (1993) 2540–2545. doi:10.1016/0032-3861(93)90586-Y.

[71] H. Tanaka, T. Nishi, Local phase separation at the growth front of a polymer spherulite during crystallization and nonlinear spherulitic growth in a polymer mixture with a phase diagram, Phys. Rev. A. 39 (1989) 783–794. doi:10.1103/PhysRevA.39.783.

[72] H. Kang, M.A. Uddin, C. Lee, K.H. Kim, T.L. Nguyen, W. Lee, Y. Li, C. Wang, H.Y. Woo, B.J. Kim, Determining the role of polymer molecular weight for high-

performance all-polymer solar cells: Its effect on polymer aggregation and phase separation, J. Am. Chem. Soc. 137 (2015) 2359–2365. doi:10.1021/ja5123182.

[73] L.M. Robeson, Fundamentals of Polymer Blends, in: Polym. Blends a Compr. Rev., 2007: pp. 10–23.

[74] R. Gelles, C.W. Frank, Effect of Molecular Weight on Polymer Blend Phase Separation Kinetics, Macromolecules. 16 (1983) 1448–1456. doi:10.1021/ma00243a008.

[75] Y. Doi, A. Steinbüchel, eds., Biopolymers, Biology, Chemistry, Biotechnology, Applications, Volume 4, Polyesters III - Applications and Commercial Products, Wiley-Blackwell, 2002.

[76] Q.Y. Wu, B.T. Liu, M. Li, L.S. Wan, Z.K. Xu, Polyacrylonitrile membranes via thermally induced phase separation: Effects of polyethylene glycol with different molecular weights, J. Memb. Sci. 437 (2013) 227–236. doi:10.1016/j.memsci.2013.03.018.

[77] R.M. Briber, F. Khoury, The phase diagram and morphology of blends of poly(vinylidene fluoride) and poly(ethyl acrylate), Polymer (Guildf). 28 (1987) 38–46. doi:10.1016/0032-3861(87)90316-8.

[78] A.T. Lorenzo, L. Arnal, J. Albuerne, A.J. Mu, DSC isothermal polymer crystallization kinetics measurements and the use of the Avrami equation to fit the data: Guidelines to avoid common problems, Polym. Test. 26 (2007) 222–231. doi:10.1016/j.polymertesting.2006.10.005.

[79] O.S. Fleming, K.L.A. Chan, S.G. Kazarian, High-pressure CO_2-enhanced polymer interdiffusion and dissolution studied with in situ ATR-FTIR spectroscopic imaging, Polymer (Guildf). 47 (2006) 4649–4658. doi:10.1016/j.polymer.2006.04.059.

[80] G. Mensitieri, G. Scherillo, C. Panayiotou, P. Musto, Towards a predictive thermodynamic description of sorption processes in polymers: The synergy between theoretical EoS models and vibrational spectroscopy, Mater. Sci. Eng. R Reports. 140 (2020) 100525. doi:10.1016/j.mser.2019.100525.

[81] J. Zhang, Y. Duan, H. Sato, H. Tsuji, I. Noda, S. Yan, Y. Ozaki, Crystal modifications and thermal behavior of poly(L-lactic acid) revealed by infrared spectroscopy, Macromolecules. 38 (2005) 8012–8021. doi:10.1021/ma051232r.

[82] X. Chen, G. Hou, Y. Chen, K. Yang, Y. Dong, H. Zhou, Effect of molecular weight on crystallization, melting behavior and morphology of poly(trimethylene terephalate), Polym. Test. 26 (2007) 144–153. doi:10.1016/j.polymertesting.2006.08.011.

[83] J. Xu, S. Zhang, B. Guo, Insights from polymer crystallization: Chirality, recognition and competition, Chinese Chem. Lett. 28 (2017) 2092–2098. doi:10.1016/j.cclet.2017.10.012.

[84] J. Zhang, H. Sato, T. Furukawa, H. Tsuji, I. Noda, Y. Ozaki, Crystallization behaviors of poly(3-hydroxybutyrate) and poly(L-lactic acid) in their immiscible and miscible blends, J. Phys. Chem. B. 110 (2006) 24463–24471. doi:10.1021/jp065233c.

[85] A. Nogales, B.S. Hsiao, R.H. Somani, S. Srinivas, A.H. Tsou, Shear-induced crystallization of isotactic polypropylene with different molecular weight distributions: in situ small- and wide-angle X-ray scattering studies, Polymer (Guildf). 42 (2001) 5247–5256.

[86] R.H. Somani, B.S. Hsiao, A. Nogales, S. Srinivas, A.H. Tsou, I. Sics, F.J. Balta-calleja, T.A. Ezquerra, Structure Development during Shear Flow-Induced Crystallization of i-PP: In-Situ Small-Angle X-ray Scattering Study, Macromolecules. 33 (2000) 9385–9394. doi:10.1021/ma001124z.

[87] W.C. Lai, W. Bin Liau, T.T. Lin, The effect of end groups of PEG on the crystallization behaviors of binary crystalline polymer blends PEG/PLLA, Polymer (Guildf). 45 (2004) 3073–3080. doi:10.1016/j.polymer.2004.03.003.

[88] J. Zhang, H. Sato, I. Noda, Y. Ozaki, Conformation rearrangement and molecular dynamics of poly(3- hydroxybutyrate) during the melt-crystallization process investigated by infrared and two-dimensional infrared correlation spectroscopy, Macromolecules. 38 (2005) 4274–4281. doi:10.1021/ma0501343.

[89] N. Zhang, X. Yu, J. Duan, J. hui Yang, T. Huang, X. dong Qi, Y. Wang, Comparison study of hydrolytic degradation behaviors between α′- and α-poly(L-lactide), Polym. Degrad. Stab. 148 (2018) 1–9. doi:10.1016/j.polymdegradstab.2017.12.014.

[90] A. Gupper, K.L.A. Chan, S.G. Kazarian, FT-IR imaging of solvent-induced crystallization in polymers, Macromolecules. 37 (2004) 6498–6503. doi:10.1021/ma049313v.

[91] D. Iruretagoyena, K. Bikane, N. Sunny, H. Lu, S.G. Kazarian, D. Chadwick, R. Pini, N. Shah, Enhanced selective adsorption desulfurization on CO_2 and steam treated activated carbons: Equilibria and kinetics, Chem. Eng. J. 379 (2020) 122356. doi:10.1016/j.cej.2019.122356.

[92] H. Yang, M. Shibayama, N. Shimizu, R.S. Stein, T. Hashimoto, Deuteration Effects on the Miscibility and Phase Separation Kinetics of Polymer Blends, Macromolecules. 19 (1986) 1667–1674. doi:10.1021/ma00160a032.

[93] N. Inaba, T. Yamada, S. Suzuki, T. Hashimoto, Morphology Control of Binary Polymer Mixtures by Spinodal Decomposition and Crystallization. 2. Further Studies on Polypropylene and Ethylene-Propylene Random Copolymer, Macromolecules. 21 (1988) 407–414. doi:10.1021/ma00180a021.

[94] J.C. Meredith, E.J. Amis, LCST phase separation in biodegradable polymer blends : poly (D, L-lactide) and poly (e-caprolactone), Macromol.Chem.Phys. 42 (2000) 733–739.

[95] A.R. Kakroodi, Y. Kazemi, D. Rodrigue, C.B. Park, Facile production of biodegradable PCL/PLA in situ nanofibrillar composites with unprecedented compatibility between the blend components, Chem. Eng. J. 351 (2018) 976–984. doi:10.1016/j.cej.2018.06.152.

[96] Y. Ahmadzadeh, A. Babaei, A. Goudarzi, Assessment of localization and degradation of ZnO nano-particles in the PLA/PCL biocompatible blend through a comprehensive rheological characterization, Polym. Degrad. Stab. 158 (2018) 136–147. doi:10.1016/j.polymdegradstab.2018.10.007.

[97] A.K. Matta, R.U. Rao, K.N.S. Suman, V. Rambabu, Preparation and Characterization of Biodegradable PLA / PCL Polymeric Blends, MSPRO. 6 (2014) 1266–1270. doi:10.1016/j.mspro.2014.07.201.

[98] T. Patrício, P. Bártolo, Thermal stability of PCL / PLA blends produced by physical blending process, Procedia Eng. 59 (2013) 292–297. doi:10.1016/j.proeng.2013.05.124.

[99] I. Navarro-Baena, V. Sessini, F. Dominici, L. Torre, J.M. Kenny, L. Peponi, Design of biodegradable blends based on PLA and PCL: From morphological, thermal and mechanical studies to shape memory behavior, Polym. Degrad. Stab. 132 (2016) 97–108. doi:10.1016/J.POLYMDEGRADSTAB.2016.03.037.

[100] H. Walter, E. Dermitzaki, H. Shirangi, B. Wunderle, S. Hartmann, B. Michel, Influence of moisture on the time and temperature dependent properties of polymer systems, 2009 10th Int. Conf. Therm. Mech. Multi-Physics Simul. Exp. Microelectron. Microsystems, EuroSimE 2009. (2009) 1–5. doi:10.1109/ESIME.2009.4938469.

[101] B. Hammouda, B.J. Bauer, Compressibility of Two Polymer Blend Mixtures, Macromolecules. 28 (1995) 4505–4508. doi:10.1021/ma00117a019.

[102] V.S. RamachandraRao, J.J. Watkins, Phase separation in polystyrene-poly(vinyl methyl ether) blends dilated with compressed carbon dioxide, Macromolecules. 33 (2000) 5143–5152. doi:10.1021/ma000066e.

[103] S.P. Nunes, T. Inoue, Evidence for spinodal decomposition and nucleation and growth mechanisms during membrane formation, J. Memb. Sci. 111 (1996) 93–103. doi:10.1016/0376-7388(95)00281-2.

[104] B. Sun, Y. Lin, P. Wu, H.W. Siesler, A FTIR and 2D-IR spectroscopic study on the microdynamics phase separation mechanism of the poly(N-isopropylacrylamide) aqueous solution, Macromolecules. 41 (2008) 1512–1520. doi:10.1021/ma702062h.

[105] S.G. Kazarian, G.G. Martirosyan, Spectroscopy of polymer/drug formulations processed with supercritical fluids: In situ ATR-IR and Raman study of impregnation of ibuprofen into PVP, Int. J. Pharm. 232 (2002) 81–90. doi:10.1016/S0378-5173(01)00905-X.

[106] C. Peña, T. Castillo, A. García, M. Millán, D. Segura, Biotechnological strategies to improve production of microbial poly-(3-hydroxybutyrate): A review of recent research work, Microb. Biotechnol. 7 (2014) 278–293. doi:10.1111/1751-7915.12129.

[107] E. Chiellini, R. Solaro, I. Meisel, eds., Recent Advances in Biodegradable Polymers and Plastics, Wiley-VCH Verlag GmbH, Weinheim, Germany, 2003.

[108] Y. Doi, A. Steinbüchel, eds., Polyesters II: Properties and Chemical Synthesis (Biopolymers, Vol. 3b), Wiley-VCH, Weinheim, Germany, 2001.

[109] R.A. Auras, L.-T. Lim, S.E.M. Selke, H. Tsuji, eds., Poly(lactic acid): Synthesis, Structures, Properties, Processing, and Applications, John Wiley & Sons, Inc, 2010.

[110] R. Auras, B. Harte, S. Selke, An overview of polylactides as packaging materials, Macromol. Biosci. 4 (2004) 835–864. doi:10.1002/mabi.200400043.

[111] M. Kobielarz, M. Gazińska, M. Tomanik, B. Stępak, K. Szustakiewicz, J. Filipiak, A. Antończak, C. Pezowicz, Physicochemical and mechanical properties of CO_2 laser-modified biodegradable polymers for medical applications, Polym. Degrad. Stab. 165 (2019) 182–195. doi:10.1016/j.polymdegradstab.2019.05.010.

[112] H. Tanaka, T. Nishi, New Types of Phase Separation Behavior during the Crystallization Process in Polymer Blends with Phase Diagram, Phys. Rev. Lett. 55 (1985).

[113] X. Zhang, Z. Wang, M. Muthukumar, C.C. Han, Fluctuation-assisted crystallization: In a simultaneous phase separation and crystallization polyolefin blend system, Macromol. Rapid Commun. 26 (2005) 1285–1288. doi:10.1002/marc.200500304.

[114] A. Vichi, G. Eliazyan, S.G. Kazarian, Study of the Degradation and Conservation of Historical Leather Book Covers with Macro Attenuated Total Reflection − Fourier Transform Infrared Spectroscopic Imaging, ACS Omega. 3 (2018) 7150–7157. doi:10.1021/acsomega.8b00773.

[115] R.M.R. Wellen, E.L. Canedo, M.S. Rabello, Melting and crystallization of poly(3-hydroxybutyrate)/carbon black compounds. Effect of heating and cooling cycles on phase transition, J. Mater. Res. 30 (2015) 3211–3226. doi:10.1557/jmr.2015.287.

[116] M. Hiramitsu, Y. Doi, Microbial synthesis and characterization of poly(3-hydroxybutyrate-co-3-hydroxypropionate), Polymer (Guildf). 34 (1993). doi:10.1016/0032-3861(93)90719-Q.

[117] W.T. Chuang, U.S. Jeng, H.S. Sheu, P. Da Hong, Competition between phase separation and crystallization in a PCL/PEG polymer blend captured by synchronized SAXS, WAXS, and DSC, Macromol. Res. 14 (2006) 45–51. doi:10.1007/BF03219067.

[118] H. Yoshida, G.Z. Zhang, T. Kitamura, T. Kawai, Compatibility of polymer blends evaluated by crystallization dynamics simultaneous DSC-FTIR method, J. Therm. Anal. Calorim. 64 (2001) 577–583. doi:10.1023/A:1011559420408.

[119] T. Hashimoto, J. Kumaki, H. Kawai, Time-Resolved Light Scattering Studies on Kinetics of Phase Separation and Phase Dissolution of Polymer Blends.1 1. Kinetics of Phase Separation of a Binary Mixture of Polystyrene and Polyvinyl methyl ether), Macromolecules. 16 (1983) 641–648. doi:10.1021/ma00238a030.

[120] Y. Doi, Microbial polyesters, VCH, New York, 1990.

[121] A. J. Anderson, E. A. Dawes, Occurrence, metabolism, metabolic role, and industrial uses of bacterial polyhydroxyalkanoates, Microbiol. Rev. 54 (1990) 450–472.

[122] M. Vert, Aliphatic polyesters: Great degradable polymers that cannot do everything, Biomacromolecules. 6 (2005) 538–546. doi:10.1021/bm0494702.

[123] Catia Bastioli, ed., Handbook of Biodegradable Polymers, De Gruyter, UK, 2005.

[124] H. Tsuji, Poly(lactic acid) stereocomplexes: A decade of progress, Adv. Drug Deliv. Rev. 107 (2016) 97–135. doi:10.1016/j.addr.2016.04.017.

[125] H. Urayama, T. Kanamori, Y. Kimura, Properties and biodegradability of polymer blends of poly(L-lactide)s with different optical purity of the lactate units, Macromol. Mater. Eng. 287 (2002) 116–121. doi:10.1002/1439-2054(20020201)287:2<116::AID-MAME116>3.0.CO;2-Z.

[126] H. Sato, M. Nakamura, A. Padermshoke, H. Yamaguchi, H. Terauchi, S. Ekgasit, I. Noda, Y. Ozaki, Thermal behavior and molecular interaction of poly(3-hydroxybutyrate-co-3- hydroxyhexanoate) studied by wide-angle X-ray diffraction, Macromolecules. 37 (2004) 3763–3769. doi:10.1021/ma049863t.

[127] H. Sato, R. Murakami, A. Padermshoke, F. Hirose, K. Senda, I. Noda, Y. Ozaki, Infrared spectroscopy studies of CH···O hydrogen bondings and thermal behavior of biodegradable poly(hydroxyalkanoate), Macromolecules. 37 (2004) 7203–7213. doi:10.1021/ma049117o.

[128] H. Sato, K. Mori, R. Murakami, Y. Ando, I. Takahashi, J. Zhang, H. Terauchi, F. Hirose, K. Senda, K. Tashiro, I. Noda, Y. Ozaki, Crystal and lamella structure and C-H ···O=C hydrogen bonding of poly(3-hydroxyalkanoate) studied by X-ray diffraction and infrared spectroscopy, Macromolecules. 39 (2006) 1525–1531. doi:10.1021/ma051777l.

[129] H. Sato, Y. Ando, J. Dybal, T. Iwata, I. Noda, Y. Ozaki, Crystal structures, thermal behaviors, and C-H···O=C hydrogen bondings of poly(3-hydroxyvalerate) and poly(3-hydroxybutyrate) studied by infrared spectroscopy and X-ray diffraction, Macromolecules. 41 (2008) 4305–4312. doi:10.1021/ma702222a.

[130] L. Guo, H. Sato, T. Hashimoto, Y. Ozaki, FTIR study on hydrogen-bonding interactions in biodegradable polymer blends of poly(3-hydroxybutyrate) and poly(4-vinylphenol), Macromolecules. 43 (2010) 3897–3902. doi:10.1021/ma100307m.

[131] L. Guo, H. Sato, T. Hashimoto, Y. Ozaki, Thermally induced exchanges of hydrogen bonding interactions and their effects on phase structures of poly(3-hydroxybutyrate) and poly(4-vinylphenol) blends, Macromolecules. 44 (2011) 2229–2239. doi:10.1021/ma102601p.

[132] N. Suttiwijitpukdee, H. Sato, J. Zhang, T. Hashimoto, Effects of intermolecular hydrogen bondings on isothermal crystallization behavior of polymer blends of cellulose acetate butyrate and poly(3-hydroxybutyrate), Macromolecules. 44 (2011) 3467–3477. doi:10.1021/ma200365e.

[133] M.A. Abdelwahab, A. Flynn, B. Sen Chiou, S. Imam, W. Orts, E. Chiellini, Thermal, mechanical and morphological characterization of plasticized PLA-PHB blends, Polym. Degrad. Stab. 97 (2012) 1822–1828. doi:10.1016/j.polymdegradstab.2012.05.036.

[134] I. Ohkoshi, H. Abe, Y. Doi, Miscibility and solid-state structures for blends of poly[(S)-lactide] with atactic poly[(R,S)-3-hydroxybutyrate], Polymer (Guildf). 41 (2000) 5985–5992. doi:10.1016/S0032-3861(99)00781-8.

[135] K.L.A. Chan, S.G. Kazarian, D. Vassou, V. Gionis, G.D. Chryssikos, In situ high-throughput study of drug polymorphism under controlled temperature and humidity using FT-IR spectroscopic imaging, Vib. Spectrosc. 43 (2007) 221–226. doi:10.1016/j.vibspec.2006.07.015.

[136] H. Shinzawa, K. Awa, Y. Ozaki, H. Sato, Near-infrared imaging analysis of cellulose tablets by a band position shift, Appl. Spectrosc. 63 (2009) 974–977. doi:10.1366/000370209788964584.

[137] H. Shinzawa, K. Awa, Y. Ozaki, Compressino-induced morphological and molecular structura changes of cellulose tablets probed with near infrared imaging, J. Near Infrared Spectrosc. 19 (2011) 15–22. doi:10.1255/jnirs.918.

[138] C.L. Song, S.G. Kazarian, Effect of Controlled Humidity and Tissue Hydration on Colon Cancer Diagnostic via FTIR Spectroscopic Imaging, Anal. Chem. 92 (2020) 9691–9698. doi:10.1021/acs.analchem.0c01002.

[139] K.L.A. Chan, A. Altharawi, P. Fale, C.L. Song, S.G. Kazarian, G. Cinque, V. Untereiner, G.D. Sockalingum, Transmission Fourier Transform Infrared Spectroscopic Imaging, Mapping, and Synchrotron Scanning Microscopy with Zinc Sulfide Hemispheres on Living Mammalian Cells at Sub-Cellular Resolution, Appl. Spectrosc. 74 (2020) 544–552. doi:10.1177/0003702819898275.

[140] Y. Hikima, J. Morikawa, S.G. Kazarian, Analysis of molecular orientation in polymeric spherulite using polarized micro attenuated total reflection Fourier transform infrared (ATR-FTIR) spectroscopic imaging, Anal. Chim. Acta. 1065 (2019) 79–89. doi:10.1016/j.aca.2019.02.017.

[141] T. Furukawa, H. Sato, R. Murakami, J. Zhang, Y.X. Duan, I. Noda, S. Ochiai, Y. Ozaki, Structure, dispersibility and crystallinity of poly (hydroxybutyrate)/ poly(l-lactic acid) blends studied by FT-IR microspectroscopy and differential scanning calorimetry, Macromolecules. 54 (2005) 3593.